NORTHWESTERN UNIVERSITY

Metal Ion Fluxes and Localization in Amphibian Fertilization

A DISSERTATION

SUBMITTED TO THE GRADUATE SCHOOL

IN PARTIAL FULFILMENT OF THE REQUIREMENTS

for the degree

DOCTOR OF PHILOSOPHY

Field of Biological Sciences

By

John Frederick Seeler

EVANSTON, ILLINOIS

June 2021

ABSTRACT

Metal Ion Fluxes and Localization in Amphibian Fertilization

John F. Seeler

Meiosis is a highly regulated process necessary for proper chromosome division. Zinc fluxes regulate mammalian meiosis; between prophase I and metaphase II, total intracellular zinc increases by 50%, while 20% of zinc is released in "zinc sparks" following fertilization. Although zinc fluxes had been shown to be conserved in mammals, it was unknown if they were conserved in different classes of animals. *Xenopus laevis*, the African clawed frog, was therefore used for these experiments. As a model organism, *Xenopus* provides a different toolkit than mammals, namely the large size and easy acquisition of its eggs. Both the zinc spark and a decrease in accessible zinc leading to entry into anaphase II were found to be conserved in *Xenopus*. Additionally, the majority of intracellular manganese is released following fertilization. Most manganese in both eggs and embryos is bound to a low-molecular weight carboxylate. Zinc and manganese are stored in cortical vesicles along with calcium and multiple other transition metals. Both extracellular zinc and manganese act as blocks to polyspermy, though the IC_{50} of zinc is an order of magnitude less than that of manganese. Because amphibians were the first tetrapod class to evolutionarily diverge, meiotic zinc fluxes are therefore an ancient phenomenon. The manganese release is an unexpected finding, demonstrating a further novel role of a transition metal ion. Compared to mammalian zygotes, proportionally less zinc is released from *Xenopus*, which is probably due to significantly different egg geometries as well as the large amount of zinc storage in the *Xenopus* yolk. Multiple transition metals are not stored in the cortical granules of other species' eggs – it is possible that *Xenopus* uses them as a system of detoxification.

In the second part of this thesis, the zinc binding of EMI2, a meiotic spindle checkpoint protein, was studied. The molecular mechanism by which zinc fluxes regulate meiosis is unknown. EMI2 inhibits the APC/C, an E3 ubiquitin ligase that regulates the cell cycle. EMI2 starts to be expressed when egg zinc levels rise and is degraded following the zinc spark. The protein contains two zinc-binding sites and mutating its zinc-binding region leads to meiotic catastrophe, so it is hypothesized that it is regulated by differential zinc binding. Competitive chelation results show a 420,000-fold difference in binding affinity between EMI2's two zinc-binding sites. Using high-energy-resolution fluorescence detection spectroscopy, the first binding site (Cys_4) binds zinc tighter than the second binding site (Cys_3His). The difference in zinc-binding affinities in EMI2 are significantly greater than those found in other RING domain proteins. Although *in vitro* and *in vivo* experiments are necessary to determine functionality, these initial results support the hypothesis that EMI2 acts as a zinc-dependent meiotic regulator.

The localization and concentration of transition metals in biological samples are mapped using microscopic methods; however, the fixation process can lead to bulk elemental changes and/or alterations in their localization. In the third part of this thesis, the effects of a modified version of Timm's sulfide staining method were studied to determine if sulfide fixation maintains transition metal content and localization as well as to determine which step(s) of the fixation to resin-infusion process lead to the greatest amounts of elemental change. Chemically-fixed biological samples used for elemental mapping experiments tend to show a significant loss in transition metal content. Aided by the large size of *Xenopus* eggs, bulk elemental content was analyzed at each step of the fixation and resin-infusion process to determine if and when metal content changed. Surprisingly, sulfide was not necessary for the preservation of either bulk transition metal content or localization in *Xenopus* eggs, probably because the majority of metals

are tightly bound in organelles. Additionally, inductively coupled plasma mass spectrometric analysis showed that microscopy-grade chemicals have enough metal content to contaminate biological samples, demonstrating that sample preparation techniques need to be optimized before starting elemental mapping experiments.

Altogether, these studies have revealed new insights into the roles of transition metals in meiosis. Meiotic zinc fluxes are conserved in *Xenopus*, suggesting that this is an ancient phenomenon. Additionally, a novel manganese release leading to a block to polyspermy was discovered, revealing that other transition metals have important roles in fertilization. Linking intracellular zinc fluxes to possible regulatory pathways, EMI2's two zinc-binding sites demonstrate the greatest difference in zinc-binding affinities of all previously-studied RING domain proteins, suggesting that one site is regulatory and the other is structural. These results contribute to the paradigm shift that transition metals, rather than only alkali and alkaline earth metals, can serve as signaling agents. Finally, studying elemental changes following chemical fixation in *Xenopus* eggs demonstrates that tissue type, particularly influenced by the intracellular metal binding environment, strongly affects metal retention. Rarely considered previously, residual metal content in fixation solutions can be enough to lead to significant sample contamination, demonstrating that researchers should analyze the chemicals they use before performing elemental mapping experiments.

Six video files are part of this thesis. Their corresponding captions can be found in Appendix A, page 191.

ACKNOWLEDGEMENTS

First and foremost, thanks my advisors Drs. Thomas O'Halloran, Teresa Woodruff, and Carole LaBonne. I want to thank Tom O'Halloran for his invaluable guidance and mentorship in my daily research work and overall professional development over the past six years. I am grateful for the constant guidance and support of Teresa in my research and scholarship. Carole provided valuable insights to my work as well as lab resources to help me complete my research. Thank you to my other two committee members, Drs. Kelly Mayo and Sadie Wignall, for their support and helpful conversations.

In the O'Halloran laboratory, Dr. Haimei Chen trained me in proper ICP-MS sample preparation as well techniques to avoid metal contamination. Dr. Seth Garwin shared his broad knowledge on meiosis and inorganic chemistry as well as assisting with imaging experiment design. Aaron Sue and Dr. Ignacio Melgar provided many helpful conservations. Dr. Sandra Siepka and Cristin Connerty provided administrative support and pep talks. In the LaBonne lab, Joe Nguyen, Rachel Schermerhorn and Drs. Elsy Buitrago, Paul Huber, and Betsy Schock all helped me with *Xenopus* questions and frog preparation.

For the EMI2 project, thanks to Dr. Stephen Allen for initial experimental design. Ryan Marcum in the Radhakrishnan lab shared his minimal media growth protocol and advice. Drs. Irina Shepotinovskaya and Sergii Pshenychnyi in the Recombinant Protein Production Core aided in protein purification. Undergraduate researchers Emma Schultz and Isaac Garey assisted with experiments. At the University of Saskatchewan, Dr. Graham George helped design the HERFD experiment, while Dr. Muhammed Qureshi at SLAC National Accelerator Laboratory ran the

samples. Finally, Dr. Andrew Crawford has been a great help in the past few months and has introduced new techniques and knowledge to the project.

At Northwestern, Dr. Brian Hoffman helped to design and analyze EPR experiments while Dr. Ajay Sharma designed, performed, and analyzed them. Drs. Jessica Hornick and Elena Antonova in the Biological Imaging Facility helped to design imaging experiments. Additionally, Jessica found and purchased a microscope lens that could image an entire *Xenopus* egg. Thanks to Yu-Ying Chen for her collaboration on the fixation paper. Dr. Reiner Bleher assisted with experimental design, sample preparation, and helpful conversations. In the Quantitative Bio-element Imaging Center Dr. Keith MacRenaris, Rebecca Sponenburg, and Omar Ali assisted with ICP-MS and ICP-OES.

At Argonne National Laboratory, Dr. Olga Antipova helped with initial experiments. Dr. Barry Lai worked with me over several visits to acquire data at Beamline 2-ID-D. Dr. Nestor Zaluzec designed and performed AEM experiments.

Thanks especially to Drs. Andrew Nowakowski and Steven Philips. Drew helped me with all of my random science questions, while Steve answered my biochemical questions and knew where everything was and how everything worked in lab.

TABLE OF CONTENTS

LIST OF ILLUSTRATIONS AND FIGURES

LIST OF TABLES

APPENDIX A: SUPPLEMENTARY METHODS, CALCULATIONS, FIGURES, AND VIDEO CAPTIONS FOR METAL ION FLUXES CONTROLLING AMPHIBIAN FERTILIZATION

APPENDIX B: SUPPLEMENTARY FIGURES AND TABLES FOR THE EFFECTS OF CHEMICAL FIXATION ON THE METAL CONTENT OF EGGS AND TISSUE

CHAPTER 1: GENERAL INTRODUCTION

Zinc fluxes are necessary for meiotic progression in mammalian eggs and sperm. Artificially perturbing intracellular zinc concentrations at different meiotic stages leads to either meiotic arrest or catastrophe, demonstrating that zinc plays a regulatory role in the gametic cell cycle. This thesis demonstrates that metal release and intracellular metal localization govern meiosis in an organism from a different class of Animalia, *Xenopus laevis*, the African Clawed Frog. Because of the large size and quantity of its eggs, the use of *Xenopus* as a model organism provides different advantages than mammalian systems.

My central hypothesis is that a reduction in zinc is necessary for *Xenopus* embryos' entry in anaphase II and that the release of both zinc and manganese from a series of cortical vesicles acts as a block to multiple sperm entry. Additionally, I provide evidence that the two zinc binding sites in zinc binding region of the meiotic protein EMI2 have significantly different binding affinities, suggesting that changes in intracellular zinc levels can regulate EMI2's function.

In the first section of this chapter, I will review the background of zinc sparks in mammals as well as in other classes and phyla of Animalia. Following that discussion, I will describe how proper zinc levels are necessary at different stages of meiosis for proper cell cycle progress. I will describe the advantages of *Xenopus* as a model organism and what was previously known about its oocytes' and eggs' zinc concentrations. Finally, I will summarize what little is known of manganese in meiosis.

In the second section of this chapter, I will describe the role of the spindle checkpoint proteins EMI1 and EMI2 in mitosis and meiosis. I will describe the structure and function of EMI2, as well as its regulation in *Xenopus*, the organism in which many of the protein's functions have been studied. Finally, I will discuss the necessity of EMI2's zinc binding region for proper meiotic progress and how it might play a role in the regulation of EMI2.

In the third section of this chapter, I will provide an overview of the elemental imaging of biological samples. I will describe two different elemental mapping techniques and their advantages and disadvantages. Additionally, I will describe the elemental and ultrastructural effects of different sample preparation methods and the development of the sulfide fixation technique for biological samples. Finally, at the end of this chapter I will describe the scope of my thesis.

Meiotic Zinc Fluxes and Oocyte Metal Localization

The Biological Role of Zinc

Zinc is a common protein cofactor that is bound by a functional domain known as the zinc finger. Zinc finger proteins account for three percent of all human genes. (1) Recent research, however, has demonstrated that zinc may also have regulatory roles in a variety of organisms. It is well-established that alkali and alkaline metal ions such as Na^{+}, K^{+}, and Ca^{2+} play roles in cellular regulation and signal transduction. Zn^{2+} has a signal transduction role in the brain. Zinc is found in synaptic vesicles within glutamatergic neurons, with the highest density within the hippocampal mossy fiber terminals. Zinc functions as a neuromodulator when the vesicles release to the synaptic cleft. (2) Additionally, pancreatic islet cells have high concentrations of intracellular Zn^{2+}. Much of the Zn^{2+} is stored in secretory granules. When Zn^{2+} is released from the granules, it has autocrine and paracrine effects, and possibly has endocrine functions through the circulatory systems. (3) However, it was not until recently that zinc was found to play a regulatory role in a different physiological process, meiosis.

“Zinc Sparks” and their Analogues in Different Species

A striking feature of zinc regulatory pathways in mammalian oocytes is the coordinated uptake of billions of zinc ions in the brief final stages of meiotic maturation (Figure 1.1). (4) As oocytes undergo meiosis, their zinc content increases by 50% (an increase of 20 billion atoms) between the germinal vesicle (GV) stage and metaphase II, which takes around 12 hours (4, 5), to a final content of 60 billion zinc atoms. (4, 6) About 10% of total intracellular zinc leaves within 2 hours post-fertilization while 20% of the zinc leaves within 6 hours post fertilization (4, 6) in events described as zinc sparks. (7)

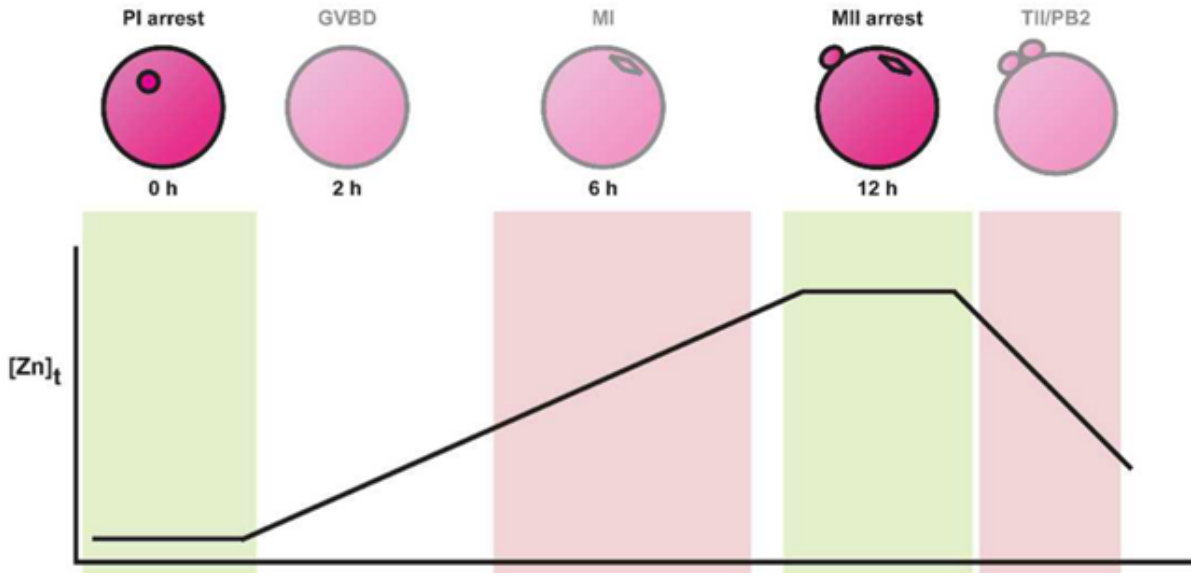

Figure 1.1: Zinc fluxes during murine oocyte meiosis. Modified from (8).

The zinc is released from a pool of approximately 8,000 cortical vesicles, located within 5 μm of the plasma membrane. It is estimated that around 15% of the zinc in the egg is stored in these vesicles with average diameters of 260 nm. (6) The highest concentration of zinc-containing vesicles is the vegetal pole, whence the largest amount of zinc efflux. The animal pole contains a

much lower number of vesicles and therefore shows a lower intensity of zinc release. (6) The zinc-containing cortical vesicles in mouse were later identified as cortical granules (CGs). (9) CGs are a type of vesicle that release their contents following fertilization. In addition to zinc, mouse CGs contain ovastacin, a metalloendopeptidase, which cleaves the glycan ZP2. (9) *Xenopus* CGs contain an orthologue (hatching enzyme). (10)

Zinc sparks are essential for the transition of the egg into an embryo. Several roles have been identified: they regulate transitions from the meiotic to mitotic cell cycle of the egg and resulting zygote, and play roles in the slow block to polyspermy in the cell envelope. (11, 12) In mouse eggs, the zinc released following fertilization acts to prevent polyspermy by hardening the zona pellucida (ZP). Zinc in the ZP is 300% higher post-efflux and changes the structure of the matrix. (12) Finally, the magnitude of the zinc spark is indicative of the quality of the resulting embryo. (13, 14)

First observed in *Mus musculus*, zinc sparks have been found to occur in multiple species. They occur after chemical activation in two species of monkeys (*Macaca mulatta* [rhesus macaque] and *Macaca fascicularis* [crab-eating macaque]) (7) as well as *Homo sapiens*. (15) Both chemical activation and fertilization lead to zinc sparks from cortical vesicles in *Bos taurus*. (16) Recent research has found that zinc release is conserved in lower vertebrates as well. Zinc sparks occur in *Ambystoma mexicanum* (17) (axolotls) and *Danio rerio* (zebrafish) (17, 18), the latter of whose eggs has zinc-containing cortical vesicles. (18) Zinc in the fertilization media blocked embroynic development in two invertebrates: *Strongylocentrotus purpuratus* (sea urchins) and *Hydractinia symbiolongicarpus* (cnidarians), although the authors did not study if these organisms release zinc following fertilization. (17)

An analogous phenotype is oberved in *Caenorhabditis elegans* (19) and *Drosophila melanogaster* (20) where zinc availability is required for embryo viability. Similar to mouse eggs, *Drosophila* see an increase in oocyte zinc content during oogeneis, with the formation of zinc-containing granules. Following activation, intracellular zinc decreases and zinc is released from the granules.

Additionally, zinc fluxes are necessary for proper mammalian male meiotic progression as well. Zn^{2+} redistribution is necessary for capacitation of sperm. Low levels of seminal zinc are linked to reduced fertility. (21)

Besides their role in gametes, there is evidence that fluxes in zinc content and localization accompany different stages of mitosis. Zinc and copper localize next to the metaphase plate in mitotic NIH 3T3 mouse fibroblasts, whereas in interphase cells they are most concentrated in and around the nucleus. Total cellular zinc increases almost 3-fold during mitosis (and because cell volume shrinks approximately 4-fold, the zinc concentration is therefore about an order of magnitude higher). Zinc may act as a messenger or as a protein cofactor. (22) Rat pheochromocytoma (PC12) cells have zinc concentrations that flux with cell cycle progression. Fluctuations may be necessary for protein phosphorylation and dephosphorylation and zinc is required for DNA synthesis. (23) In a non-Metazoan species, the malarial parasite *Plasmodium falciparum*, copper, magnesium, and zinc contents also increase through its lifecycle. (24)

Proper Zinc Levels are Necessary for Meiotic Progress

Zinc plays a role in regulating signaling in *Xenopus* oocytes. The maturation promoting factor (MPF), which leads to meiotic entry (25), consists of the kinase Cdk1 (a.k.a. Cdc2) and Cyclin B. (26) There are two pathways to activate the MPF, one starting with Mos and the other which is still partially unknown but which contains the kinases Plx1 and PLKK. (26)

Artificially lowering the amount of zinc in a hormonally-stimulated Stage VI[1] oocyte through the expression of an exogenous zinc transporter accelerates the rate of germinal vesicle breakdown (GVBD). Conversely, injecting oocytes with $ZnSO_4$ prevents GVBD from occurring following stimulation. Increasing concentrations of ZnSO4 prevent ERK from being phosphorylated and additionally prevent ERK kinase activity. The researchers found that zinc levels affect Ras signaling, which is upstream of ERK. (27) Similarly, treating Stage VI oocytes with 1,10-phenathroline, a chelator, activates MAPK (downstream of Mos) through chelating zinc, regardless of whether GVBD occurs. (28) Treating oocytes with the zinc-chelator N,N,N′,N′-Tetrakis(2-pyridylmethyl)ethylenediamine (TPEN) and then stimulating them with progesterone leads to a decrease in phosphorylation of Plx1 and PLKK. The oocytes do not undergo GVBD; there is no maturation spot and only low levels of phospho-Cdc2, a phosphatase downstream of Plx1 which activates Cdk1. Additionally, MAPK is only partially phosphorylated. The exact mechanism by which zinc chelation activates this signaling pathway remains to be discovered. (26)

Mammalian oocyte maturation is similarly dependent on correct zinc levels. TPEN treatment of PI-arrested mouse oocytes leads to meiotic resumption (GVBD and formation of metaphase I spindles). However, meiosis takes longer than in controls, and progress stops either at metaphase I or telophase I (TI); no oocytes proceed to metaphase II arrest. (8) Similarly, disrupting the zinc transporters ZIP6 and ZIP10 with either morpholinos or antibodies leads to

[1] The most common scheme for classifying *Xenopus* oocytes is that of Dumont. (24) There are six stages based on size, morphology, and internal development. Stage I corresponds to oocytes with diameters between 50-300 mm, while stage VI oocytes are between 1200-1300 mm. Oocytes are arrested at stage VI (interphase G_2/prophase I) until they are hormonally stimulated, leading to GVBD.

meiotic resumption. (11) Zinc is necessary for PI and metaphase II arrest. TPEN causes meiotic resumption through activating the MOS-MAPK pathway before GVBD, while the pathway is normally activated after GVBD. (8) TPEN affects the asymmetric division of mouse oocytes as well. Polar bodies should be significantly smaller than eggs, but zinc chelation leads to a higher rate of symmetric division. TPEN-treated oocytes arrest with a TI spindle attached to decompressed chromatin. Zinc supplementation is able to rescue meiotic progress up to 9 hours after TPEN addition (i.e. before polar body departure). However, the rescued oocytes have larger spindles and polar bodies than control oocytes. TPEN treated oocytes that are arrested in TI are capable of fertilization and form the same number of pronuclei as control, but cleavage is delayed and they never reach the blastocyst stage. (4)

Culturing eggs in TPEN as they go through the metaphase I/II transition prevents proper metaphase II arrest. Some eggs arrest at TI, while the others have chromosomal or spindle abnormalities. (5) A decrease in cytoplasmically-accessible zinc leads to parthenogenic activation. TPEN treatment of mouse eggs leads to non-calcium-dependent parthenogenic activation and decreases the amount of available zinc in the cytoplasm. (29) TPEN leads to a decrease in MPF and MAPK activities, which mirrors what happens after the zinc spark (i.e. pronuclear formation). (5) Fertilization and chemical activation (by $SrCl_2$ or ionomycin), lead to degradation of the protein EMI2 (see below) and CG release; neither occur after TPEN activation. (29) Similarly, treatment with TPEN leads to human egg activation. (15) TPEN treatment of *C. elegans* embryos causes both meiotic catastrophe as well as mitotic problems. Polar body extrusion and chomosone segregation are affected, leading to aneuploidy. (19)

Unnaturally high zinc levels can also disrupt meiosis. Zinc pyrithione (ZnPT, a zinc ionophore) inhibits meiotic progression of activated eggs; oocytes retain a metaphase-like spindle

(so-called “metaphase III”) rather than proceeding to interphase. (7) Addition of TPEN after ZnPT treatment leads to normal activation (formation of polar bodies and pronuclear-like structures), whereas treatment with $SrCl_2$ does not lead to activation. Therefore, a decrease in intracellular zinc is necessary for meiotic resumption. (5)

The use of *Xenopus laevis* as a Model Organism

Xenopus laevis is used as a model organism for cell cycle and developmental studies. It is difficult to acquire significant quantities of mammalian eggs to use for biochemical experiments, especially when they need to come from the same mother. *Xenopus* produces hundreds of eggs at a time. (30, 31) With diameters of 1.2-1.3 mm, they are much larger than mammalian eggs, having a volume over 5000X that of mouse. (32) They can therefore be manipulated without the use of a microscope. The animal pole of the egg is dark, while the vegetal pole is light. It is simple to determine if an egg has been fertilized, as the zygote will rotate in liquid so that the animal pole is on top, and the small white activation spot in the animal pole will shrink. One of the main disadvantages of *Xenopus* eggs is that the animal pole is pigmented and they contain auto-fluorescent yolk, making it impossible to image the interiors of live eggs with a confocal microscope. However, one can image near the surface of albino eggs. (33)

Xenopus oocytes are useful as well for the production of cycling egg extracts. There are numerous protocols for routine production of extracts, and there are many well-developed reconstitution assays for studying the cell cycle *in vitro*. (34-37) Because the spindle apparatus forms *in vitro*, it is easy to add or remove proteins or cytoplasmic components to study their roles in cell division. *Xenopus* is difficult to manipulate genetically since it is allotetraploid (38) and has a relatively long development, although CRISPR/Cas9 has made the procedure significantly easier. (39) Antisense oligonucleotides and mRNA microinjections, however, can be used to manipulate

protein expression in *Xenopus* eggs since zygotic mRNA transcription does not begin until the 13th cell cycle. (34) Therefore, *Xenopus* will be an excellent model system for future experiments to better understand the protein response to zinc fluxes in the meiotic cell cycle. This will probably involve studying the proteins EMI1 and EMI2 (see below).

Xenopus Oocyte Zinc Uptake

Zinc is transported into *Xenopus* oocytes over a period of months during oogenesis (40, 41); unlike mouse eggs, there is no massive influx during meiosis. During oogenesis, zinc is taken into eggs bound to the protein vitellogenin. (41) Vitellogenin is a plasma protein that contains 2 atoms of zinc per dimer. (42) Vitellogenin is taken into oocytes between Stages II and VI, with the "vitellogenic phase" of oogenesis lasting from Stage III – Stage VI. (41) Stage III – VI oocytes have a membrane receptor that permits vitellogenin intake by receptor-mediated endocytosis. Inside the oocyte, vitellogenin is cleaved into lipovitellin subunits 1 and 2 (which remain bound to zinc) as well as phosvitin. These proteins make up the yolk platelets. (42) It is unknown if vitellogenin taken into cells during Stage II is through receptor mediated endocytosis as well. (43) In Stage II oocytes, most zinc is in the cytosol and small vesicles. (41) In Stage III and IV oocytes, most zinc is contained in the endocytosed vesicles and multivesicular bodies, with some entering yolk platelets. By Stage V and VI, around 90% of zinc is in the yolk platelets. Zinc remains in the yolk until after tadpole hatching, when it enters the cytosol. (41)

Zinc levels do not increase as *Xenopus* oocytes progress from GV oocytes to metaphase II-arrested eggs. (40, 43) Before starting my research, it was unknown that there was a zinc efflux following fertilization in *Xenopus* eggs. Atomic absorption spectroscopy experiments measured no detectable difference in metal content between unfertilized eggs and embryos up to 48 hours

post fertilization. (40) Following fertilization, zinc, copper, and iron content does not change during the first fifty stages of embryonic development. (40)

Manganese in Meiosis and Fertilization

There has been little previous research on the manganese content of eggs. An analysis of the manganese concentration of eggs of the Norway lobster (*Nephrops norvegicus*) found that there is no significant change over developmental stages in unfertilized eggs, no significant change between oocytes and early zygotes (albeit the author did not study the act of fertilization itself), while there is a significant increase in manganese concentration during embryonic development. (44) In the Japanese rice fish (*Oryzias latipes*), the manganese content of the embryo one hour post-fertilization is over four times that of the unfertilized egg, and increases through early embryonic development. (45) The authors suspected that there is a system of active transport into the embryo in order to supply enzymes with cofactors.

Finally, one group studied the effects of Mn^{2+} during the fertilization of mouse eggs. Mn^{2+} is the cation of the sperm galactosyltransferase (GT) enzyme which interacts with the zona pellucida. Increasing Mn^{2+} levels lead to approximately logarithmic GT activity. Half-maximal activation is at 0.65 mM Mn^{2+}. However, increasing Mn^{2+} concentrations led to decreasing sperm-zona binding, with an IC_{50} at 1.25 mM Mn^{2+}. (46) These results suggest that elevated extracellular manganese levels could act as a block to polyspermy.

Research Questions

Because changes in zinc levels affect so many different aspects of meiosis, we hypothesized that they would be conserved in different classes of animal. We therefore asked the following questions: Are meiotic metal fluxes conserved in amphibia, a non-mammalian class?

Additionally, how are metals localized within *Xenopus* eggs and how does fertilization affect their localization?

The results from zinc sparks and zinc perturbation experiments led to the following question: What are the molecular mechanisms by which zinc fluxes might regulate the activity of oocyte maturation, the establishment of metaphase II arrest, and then at the time of the egg-to-embryo transition?

EMI1 and EMI2

Background and Significance

Mitosis and meiosis occur in every sexually reproducing species and require precisely timed activity of regulatory proteins at each stage. During cell division, microtubule spindles form to align and separate chromosomes appropriately. Spindle alignment is highly regulated, and many key biophysical features of the regulatory mechanism are not yet understood.

The anaphase promoting complex/cyclosome (APC/C) is a ubiquitin ligase that governs cell cycle progression. It is evolutionarily conserved, with 14 different protein subunits in vertebrates (Figure 1.2). The APC/C attaches polyubiquitin chains to substrate proteins, which are subsequently degraded by the 26S proteasome. (47) The APC/C governs meiotic progress through the destruction of enzymes and other catalytic proteins, as well as the activation of other proteins through the degradation of their inhibitors. The evolutionarily conserved spindle checkpoint proteins early mitotic inhibitor 1 (EMI1, a.k.a. F-box protein 5 [FBXO5]) and EMI2 (a.k.a. Emi1-related protein 1 [Erp1] and F-box protein 43 [FBXO43]) are involved in inhibiting the APC/C in mitosis and meiosis. (48-50) EMI1 and EMI2 inhibit the APC/C at different stages of cell division.

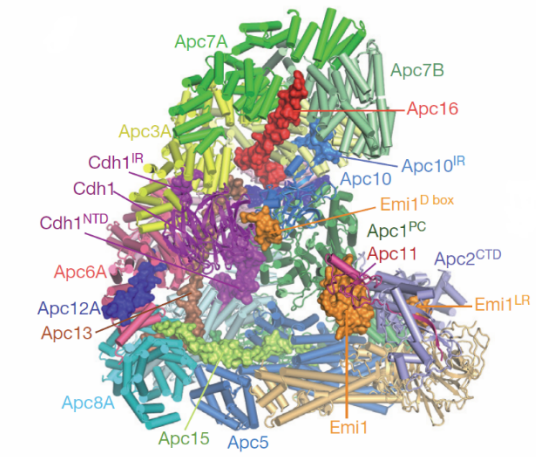

Figure 1.2: The APC/C bound to EMI1. From (51).

EMI2 Structure and Function

EMI1 was first discovered in cycling *Xenopus* extracts. (52, 53) EMI2 was later determined to be a separate protein; the antibodies used for studying EMI1 cross-reacted with EMI2 and the two proteins' functions were conflated. (54) Metaphase II arrest is mediated by cytostatic factor (CSF), which was first described in frog eggs in 1971 (55), although the proteins causing it were not identified at the time. (55, 56) EMI2 was found to be part of the CSF. (56) Both EMI1 and EMI2 are conserved in vertebrates (Figure 1.3). Mammalian and amphibian EMI2 are not functionally interchangeable and are regulated differently; *Xenopus* EMI2 is unable to enter the mouse germinal vesicle (the different temperature at which the species fertilize their eggs could affect interchangeability as well). (29)

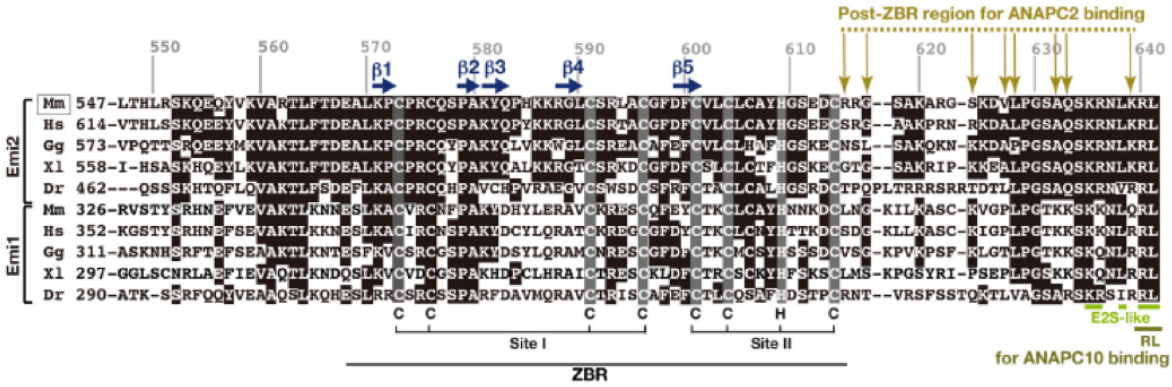

Figure 1.3: C-termini of EMI1 and EMI2 orthologs showing conservation in vertebrates. Mm, *Mus musculus*; Hs, *Homo sapiens*; Gg, *Gallus gallus* (chicken); Xl, *Xenopus laevis*; Dr, *Danio rerio* (zebrafish). From (57).

EMI2's zinc-binding region (ZBR) is a RING-finger domain located near the C-terminus. RING domains consist of two tetrahedral metal binding sites each containing two pairs of amino acid ligands (C_4 and C_3H). (58, 59) A functional ZBR is necessary for APC/C inhibition during metaphase II arrest. (29, 52, 60) Additional evidence comes from injecting EMI2 into GV oocytes, which arrests them at metaphase I. The addition of TPEN to the medium prevents the precocious arrest, meaning that EMI2 requires zinc to function. (5)

EMI1 and EMI2 have important roles in *Xenopus* meiosis and early mitosis (Figure 1.4). In a stage VI oocyte (interphase G_2/prophase I), EMI1 is expressed at a low level (61) and inhibits the APC/C during interphase. (62) EMI1 is required for G_2 exit and activation of MPF and MAPK in response to hormonal stimulation. (54) EMI1 is degraded by the $SCF^{\beta\text{-}TrCP}$ E3 ubiquitin ligase to allow progression beyond prometaphase I (56, 61); if EMI2 is prematurely expressed, metaphase I arrest occurs. (61) The APC/C is required for the metaphase I/AI transition. (60) EMI2 starts to be expressed during AI. It partially inhibits cyclin B degradation, allowing the meiosis I/meiosis II transition to occur. (62, 63)

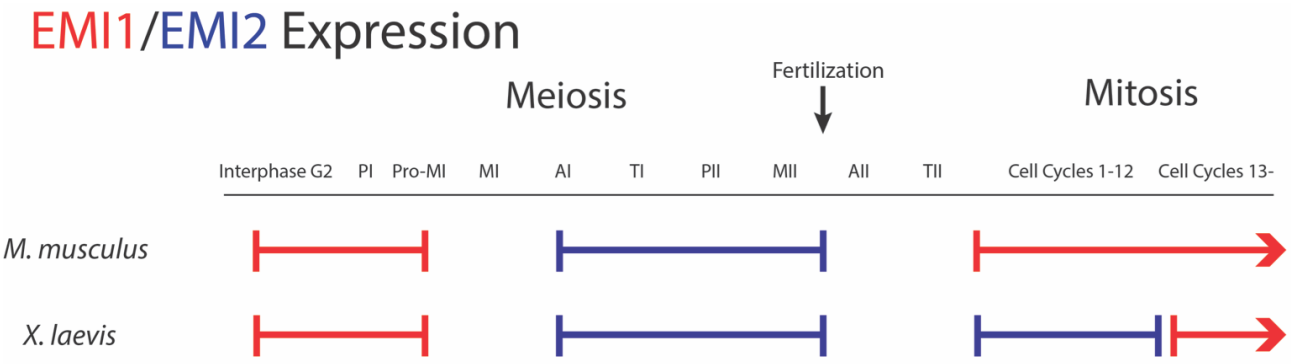

Figure 1.4: EMI1/EMI2 expression in meiosis and early mitosis. Red = EMI1, Blue = EMI2.

At metaphase II, MOS triggers a MEK/MAPK signaling cascade. (29) p90 ribosomal S6 kinase ($p90^{RSK}$), a MAPK substrate, phosphorylates EMI2, activating it. (64) EMI2 inhibits the APC/C, causing metaphase II arrest by preventing the APC/C from destroying cyclin B. (65) At fertilization there is a single calcium wave (66, 67) which activates both calcium-/calmodulin-dependent kinase II (CaMKII) and the phosphatase calcineurin (CaN, a.k.a. PP2B). (68) CaMKII phosphorylates EMI2, stimulating its interaction with the Polo Box domain of Plx1. Phosphorylation by Plx1 creates a phosphodegron for $SCF^{\beta\text{-}TrCP}$-mediated ubiquitylation of EMI2. (64) CaN activates the APC/C^{Cdc20} by both negative and positive regulation (Cdc20 is the coactivator of the APC/C). Negatively, CaN leads to the degradation of EMI2 by dephosphorylating it at pSer335 in the recruiting motif for PP2A-B'56. Positively, CaN dephosphorylates Cdc20 at an inhibitory site (pThr68), permitting it to activate the APC/C. (68) Fertilization leads to complete degradation of EMI2. (65) This the main pathway to APC/C activation. (68) The APC/C with its E2 UbcX/UbcH10 catalyzes a non-proteolytic ubiquitylation of EMI2 as well, preventing EMI2's inhibitory activities. This can accelerate APC/C activation,

leading to the quick onset of anaphase. (64) EMI2 degradation and therefore APC/C activation lead to cyclin B degradation. (69)

During the first mitotic interphase, EMI2 and cyclin B1 start to be resynthesized 20-30 minutes after calcium release. (69) EMI2 reaccumulates in early embryos to the same level as before fertilization. (65) During early embryonic divisions EMI2 is negatively regulated by Cdk1 and positively regulated by PP2A-B'56. The first mitotic division is the slowest, taking around 90 minutes. The following 11 cycles take around 30 minutes each. Cycle 13 is the mid-blastula transition, around 7 hr post-fertilization. EMI2 starts to be degraded and EMI1 is resynthesized. EMI1 rather than EMI2 is found in all subsequent cell divisions. (64)

Mammals differ in early embryonic mitosis. Mice have a prolonged first embryonic cell division as well, but subsequent murine cell divisions take 12 hours and are asynchronous. (64) EMI2 is degraded after metaphase II and it never reappears. EMI1 is synthesized and regulates the APC/C. This is probably because zygotic gene activation (the Mid-Blastula Transition, i.e. the start of new zygotic mRNA transcription) occurs after 12 cell cycles in *Xenopus* but only after 1 cycle in mice. (34, 64)

EMI2 is found in spermatids and sperm in addition to eggs and without it mice are sterile. (70) EMI2 is necessary for meiosis I in murine spermatogenesis. Without EMI2, spermatocytes arrest at diplotene of prophase I, though some further parthenogenetic division can occur. Knocking in additional Cdk1 allows the sperm to enter into MI with significant problems, possibly because Cdk1 assists with chromosome condensation. The researchers did not study meiosis II, so it is currently unknown if EMI2 is necessary for that in male meiosis.

The EMI2 Zinc-Binding Region

EMI2 requires a functional ZBR to be able to inhibit the APC/C. Schmidt and colleagues found that immunodepletion of EMI2 in *Xenopus* CSF extracts using an antibody against the N-terminus leads to premature CSF release. Premature CSF release can be rescued by the addition of a WT C-terminal fragment. However, a C-terminal fragment containing a C583A mutation (the first cysteine in the first zinc-binding site – see Figure 1.3) is unable to rescue metaphase II arrest. Similarly, excess full-length MBP-tagged $EMI2^{WT}$ or WT C-terminal fragment is able to prevent CSF release, while excess full-length MBP-tagged $EMI2^{C583A}$ cannot. (71)

Suzuki *et al.* injected metaphase II-arrested mouse eggs with $EMI2^{C573A}$ (the first cysteine of the first zinc-binding site). TPEN was added 4 hours later to determine what proportion of the eggs would undergo parthenogenic activation. Fewer $EMI2^{WT}$-injected eggs extruded their second polar bodies in comparison to $EMI2^{C573A}$ eggs. Polar body extrusion was studied in oocytes that had EMI2 depleted through siRNA and were injected with cRNA encoding other ZBR mutants (C591A [third cysteine in the first site], C601A [first cysteine in the second site], C606A [third cysteine in second site], C573A+C606A, and H609A [in the second site]). C573, C591, and C601 were found to be important for EMI2's ability to maintain metaphase II arrest. (29) Bernhardt and colleagues injected mosue oocytes with a morpholino targeting EMI2 and then were *in vitro* matured. After the first polar body formed, the oocytes were injected with cRNA either encoding $EMI2^{WT}$ or $EMI2^{C573A}$. Most morpholino-injected oocytes without cRNA rescue did not have metaphase II spindles, but rather chromatin masses with improper microtubule formations. Most $EMI2^{WT}$-injected oocytes formed proper metaphase spindles. The amount of $EMI2^{C573A}$-injected oocytes with proper spindle formation was between that of the $EMI2^{WT}$-injected and the control oocytes, demonstrating that EMI2 needs to properly bind zinc in order to function. (5)

Research Questions

Because proper zinc levels are necessary for meiosis and because EMI2 requires a functional zinc binding region in order to function, we hypothesize that EMI2 regulates meiotic progress through at least one of its two zinc binding sites. This leads to the following questions: What are the zinc-binding affinities of EMI2's two zinc binding sites? Structurally, does the C_4 or the C_3H site have the higher affinity?

Elemental Preservation in Chemically-Fixed Biological Samples

Imaging biological samples can involve compromises during sample fixation. The next section describes two types of elemental mapping and methods to preserve biological samples for X-ray imaging.

X-Ray Elemental Mapping Methods

The past decades have seen increasing levels of sensitivity in elemental analytical techniques. There are multiple methods to map elemental distribution in biological samples (72), but in this introduction I will focus on two that I used in my research: X-ray fluorescence microscopy (XFM) and scanning transmission electron microscopy energy dispersive X-ray spectroscopy (STEM-EDS). Both techniques utilize an X-ray source. After atoms are ionized by X-rays, a photon is released when they return to the ground state. The energy of the photon is based on the difference of the two electron orbitals and therefore different elements will fluoresce at different wavelengths. (73) Samples are imaged in a grid, similar to a digital camera. The X-ray beam passes over the grid stopping at each pixel for a given amount of time. This allows for a 2D map of elemental concentration to be created.

There are both synchrotron- and lab-based XFM systems. Laboratory micro-XRF systems are slower and have lower spatial and elemental resolution than synchrotron-based XFM. (72) Optimally, XFM can detect elements between phosphorus and uranium with the highest sensitivity for metalloids and transition metals. The best XFM detection limit is less than 0.1 PPM, though most systems have sensitivities 10-10,000X less than that. (72) (See Table 1.1 for the elemental detection limits of Beamline 2-ID-D at Argonne National Laboratory) XFM has greater elemental sensitivity than other mapping techniques. Another advantage of XFM is that it has deeper sample penetration compared to methods that use X-rays with energies below 3 keV. Additionally, XFM is able to acquire 3D data through the use of XFM-CT. The highest spatial resolutions of XFM are the Bionanoprobe at the Advanced Photon Source at Argonne National Laboratory (74) and Beamline ID16A at the European Synchotron Radiation Facility (75), both with spatial resolutions of ~30 nm. At this resolution organelles can be studied in detail (75), though radiation damage, which leads to bond breaking and therefore sample loss, becomes a problem. (74)

Element	**Mn**	**Fe**	**Co**	**Ni**	**Cu**	**Zn**
Sensitivity (atoms/μm^3)	4.5×10^5	6.3×10^5	3.0×10^5	2.4×10^5	5.0×10^5	2.7×10^5

Table 1.1: Minimal sensitivity of XFM. Data from Beamline 2-ID-D, Argonne National Laboratory, 500 ms/pixel scan. Data analyzed by Dr. Andrew Crawford.

STEM-EDS or Analytical Electron Microscopy (AEM) combine a scanning transmission electron microscope with an electron detector. (76, 77) Because of the overlap of different elements' X-ray peaks, EDS can detect elements with $Z > 10$. (72, 73) Spatial resolution is as low as 5 nm (78), with a minimal elemental limit of detection of 10 ppm (73), though most systems have elemental LODs hundreds of times higher. (72) One disadvantage of STEM-EDS is that

software packages are designed for materials science rather than biology, making it necessary for a user to doublecheck peak assignments. (73) Additionally, quantification of STEM-EDS samples is difficult (72, 79), meaning that much data is either presented qualitatively or as elemental ratios. In sum, synchrotron XFM provides superior elemental resolution to STEM-EDS, but STEM-EDS provides higher spatial resolution, making the two methods complementary.

Sample Preparation Methods for Elemental Analysis

Samples need to be prepared for elemental analysis via STEM-EDS or XFM, but every preservation method has its own set of advantages and disadvantages. Frozen-hydrated samples are ideal for preservation of intracellular structure, elemental content, and elemental localization, including the distribution of ions in cell water. (74) Samples are rapidly frozen in liquid propane or ethane at a speed of 10,000 K/s to a temperature of 123 K. (72) A layer of vitrified ice forms (72) which helps to prevent radiation damage when being subjected to X-rays. (74) There are some disadvantages to freeze-hydrated samples. If the biological samples have high water content, the water will dilute their intracellular elemental content, making it harder to measure. Frozen XFM samples have lower limits of detection than dry samples because of lower probe depths, increased X-ray background, and lower fluorescence escape depth. (72) Larger tissues (such as a 1.3 mm *Xenopus* egg) are not able to be frozen quickly enough to create usable frozen-hydrated samples. Finally, not every microscope is equipped for sample handling and imaging at liquid nitrogen temperatures, limiting instrument availability.

Dehydration is another type of sample preparation. In freeze drying, frozen samples are placed in a high vacuum, which then sublimates the ice. (72) Advantages of dehydrated compared to frozen-hydrated samples are that an instrument with a cryo-setup is no longer necessary and that samples are more protected against radiation damage. (74) Disadvantages of dehydration

compared to freezing are that dehydration can affect intracellular structure and that some ion loss can occur during dehydration. (74, 80) It should be noted however that elemental content and intracellular structure are still better preserved than in chemically-fixed samples. (72, 80)

Chemical fixation is the third type of sample preparation method. Samples are usually fixed with aldehydes and then infused with resin before imaging. Chemical fixation leads to the greatest changes in intracellular structure and elemental content; native ion distribution is destroyed because the aldehydes permeabilize the membranes, leading to the loss of ions and small molecules that are not tightly bound. (80-85) Phosphorus content often drops as well, probably through creating cracks in the sample and therefore increasing the surface area with which solvents can interact. (86) Depending on the tissue type, one may see transition metal loss as well. (81, 87) Although worse than freezing or dehydrating, because of the size and/or properties of a biological sample, chemical fixation may be the only applicable preparation method.

Timm's Staining Method

Because chemical fixation alters intracellular structure and can lead to transition metal loss, modified procedures are necessary to preserve metal content. Dr. F. Timm worked in forensic medicine and when studying poisoning cases decided to understand normal tissue metal distribution. (88) In the 1950s he developed a method in which tissue samples are treated with sodium sulfide. The S^{2-} interacts with M^{2+} ions creating metal sulfides, the majority of which are insoluble, preventing them from being washed out of the tissue during fixation. The samples are then treated with silver, which replaces the metal and grows in size, allowing for easy visualization of the original metal localization via light microscope or transmission electron microscopy (TEM). (88-90)

Although Timm's method allows for the visualization of metal-enriched compartments, it does not allow quantification of the metal or determination of the original size of the metal distribution. The silver replaces the original metal(s). (Reiner Bleher and Emily Que, unpublished data) Additionally, because the silver deposition reaction occurs as long as there are silver ions and reducing molecules in the vicinity of the sulfide particles, the size of the silver granules is not indicative of the size of the original metal. (86)

In order to preserve transition metal contents and localization in a chemically fixed sample, we have developed a modified form of Timm's method. We removed the silver staining step in order to image native metal contents. Visualization is not a problem, because we image the samples with elemental mapping techniques (XFM and STEM-EDS) rather than light microscopy or TEM. Previous experiments using chemically-fixed mouse eggs showed that sulfide treatment was necessary to preserve zinc content in their CGs. (6) However, bulk elemental analysis of mouse eggs via inductively coupled plasma mass spectrometry (ICP-MS) is impractical because of their small volumes combined with difficulty of acquisition, so it was not known if the sulfide fixation completely preserved transition metal contents. *Xenopus* eggs are an ideal system for studying the effects of fixation on bulk elemental content because they are significantly larger than mammalian eggs and, unlike dissected tissue, are fairly regular in size.

Research Questions

Our hypothesis for this project is that the sulfide fixation of *Xenopus* eggs will preserve most of their transition metal content. This leads to the following questions: How does chemical fixation (with and without sulfide) affect bulk elemental content as well as intracellular metal localization in *Xenopus* eggs? Additionally, when analyzing a different tissue type (fixed mouse ovaries), how does bulk elemental preservation compare?

Scope of Thesis

In this thesis I researched metal fluxes and localization in *Xenopus laevis*. Secondly, I determined whether our modified Timm's fixation method preserves transition metal content in biological samples. Thirdly, I studied a possible regulatory role for meiotic zinc fluxes, namely whether they govern the inhibitory effects of the spindle checkpoint protein EMI2.

In chapter 2 I tested the hypothesis that the zinc spark and intracellular zinc localization are conserved in a different class of animal, amphibia. I found that the zinc spark is conserved and measured a release of manganese as well. A drop in zinc is necessary for meiotic progress in *Xenopus*; chemical chelation is able to activate eggs. Analysis of the eggs and embryos via electron paramagnetic resonance confirms the loss the majority of the cell's manganese following fertilization and demonstrated that the majority of intracellular manganese, both pre- and post-fertilization, is bound to a carboxylate ligand. Zinc and manganese are stored in cortical vesicles alongside a variety of other metals. TEM images of the cortices of egg and embryo show that the majority of the electron-dense cortical vesicles disappear following fertilization. Finally, both extracellular zinc and manganese block fertilization.

In chapter 3 I tested the hypothesis that EMI2's APC/C inhibitory function is governed by differential zinc binding in its two zinc binding sites. I describe improvements I made to the inherited protein purification process in order to increase yield and prevent protein oxidation and/or degradation. I then discuss how I altered the design of the competitive chelation experiments in order to provide usable data. The results of the zinc-binding affinity experiments show that the strong-binding site has a ~420,000X stronger affinity than the weak binding site, suggesting that the weak binding site is regulatory. High-energy-resolution fluorescence detection

(HERFD) X-ray data comparing one and two zinc-bound forms of the protein suggest that the C_4 binding site is the strong binding site, while the C_3H binding site is the weak site.

In chapter 4 I studied the effects of chemical fixation on bulk metal content as well as metal localization in biological samples. *Xenopus* eggs were fixed using in a solution with and without sodium sulfide to determine the extent of sulfide preservation. Surprisingly, transition metal contents are preserved even without the addition of sulfide. Every step in the fixation to resin-infusion process was analyzed by ICP-MS to determine elemental change; the majority of change occurs during fixation. STEM-EDS analysis showed that metals remain in the cortical vesicles even without sulfide fixation. ICP-MS analysis of the solutions used for fixation and resin infusion demonstrate that some microscopy-grade chemicals contain enough metal content to contaminate biological samples. Finally, the *Xenopus* egg results were compared with those of a multicellular tissue, mouse ovaries, with the ovaries showing greater amounts of elemental loss.

Chapter 5 is a summary of my work and a discussion of the significance of my findings. Additionally, I discuss possible future research directions.

Chapter 2: Metal Ion Fluxes Controlling Amphibian Fertilization

John F. Seeler, Ajay Sharma, Nestor J. Zaluzec, Reiner Bleher, Barry Lai, Emma G. Schultz, Brian M. Hoffman, Carole LaBonne, Teresa K. Woodruff, Thomas V. O'Halloran

The data presented here have been accepted for publication in *Nature Chemistry*.

The following people acquired and analyzed data used in this chapter:

Ajay Sharma: Figures 2.5 and 2.6

Nestor J. Zaluzec: Figures 2.12 A-C, 2.13-15, 2.16B.

Abstract

Mammalian oocytes undergo major changes in zinc content and localization in order to be fertilized, the most striking being the rapid exocytosis of over ten billion zinc ions, known as zinc sparks. Here we report that fertilization of amphibian *Xenopus laevis* eggs also initiates a zinc spark that progresses across the cell surface in coordination with dynamic calcium waves. This zinc exocytosis is accompanied by a newly recognized loss of intracellular manganese: synchrotron-based X-ray fluorescence and analytical electron microscopy reveal that zinc and manganese are sequestered in a system of cortical granules that are abundant at the animal pole. Through Electron-Nuclear Double-Resonance (ENDOR) studies, a method of obtaining an NMR spectrum of the ligands to a paramagnetic metal ion, we rule out Mn^{2+} complexation with phosphate or nitrogenous ligands in intact eggs but the data are consistent with a carboxylate coordination environment. Our observations suggest that zinc and manganese fluxes are a conserved feature of fertilization in vertebrates and that they function as part of a physiological block to polyspermy.

Introduction

Physiochemical approaches are opening the door to understanding how inorganic chemistry regulates key biological processes. A striking example of this is the discovery of zinc regulatory pathways controlling fertilization of mammalian oocytes which begins with the coordinated uptake of billions of zinc ions in the brief final stages of meiotic maturation. (4) Upon fertilization, murine eggs then rapidly release between 10-20% of their zinc from a pool of 8,000 cortical vesicles in events described as zinc sparks. (6, 7) First observed using zinc responsive fluorescent probes in *M. musculus* (7), these events occur in macaques (7), *B. taurus* (16), and *H. sapiens* (15) and are essential for transition of the egg into an embryo. Studies of mouse eggs reveal several roles of these zinc sparks: they regulate transitions from the meiotic to mitotic cell cycle of the egg and resulting zygote, and play roles in the slow block to polyspermy in the cell envelope. (11, 12) The magnitude of the zinc spark, readly established in real time using fluorescent probes, correlates with the quality of the resulting embryo. (13, 14) Analogous zinc-dependent phenotypes are oberved in *Caenorhabditis elegans* (19) and *Drosophila melanogaster* (20), where zinc availability is required for embryo viability. While eggs from each of these provide specific advantages, each is limited by size and low material yields. This is not the case for the African Clawed Frog, *Xenopus lavis*.

While zinc is known to be transported into *Xenopus* oocytes over a period of months during oogenesis (40, 41), little is known about whether a zinc cycle occurs in this or other amphibians: neither influx nor exocytosis of zinc has been reported during meiosis. We decided to test whether meiotic zinc transients occur in *Xenopus* because of the large size and the abundance of eggs produced by the frog. The diameter of *Xenopus* eggs is fifteen times that of mouse eggs, allowing for a more in-depth study of the dynamics of the zinc efflux. While the abundance of auto-

fluorescent yolk platelets in frog eggs presents significant challenges in confocal microscopy studies, the large size and the fact that a typical frog extrudes hundreds of eggs at a time, each with an average dry weight of 0.45 mg/egg (91), allows for the application of methods such as Inductively Coupled Plasma Mass Spectrometry (ICP-MS) and Electron-Paramagnetic Resonance (EPR) that otherwise would require an impractically large number of mammalian eggs. These bulk-sample methods provide key benchmarks and allow for our application of an array of more sensitive quantitative methods for understanding the chemistry of metal ion fluctuations in the regulation of biological processes at both the single cell and subcellular level.

Here, we present several complimentary physical methods that show that fertilization triggers release of zinc from vesicular storage compartments at the surface of the frog egg. These cortical vesicles, located predominantly at the animal pole, are the source. Our results suggest that the storage of labile zinc complexes and their triggered release as zinc sparks may be an evolutionarily conserved and functional feature of fertilization from amphibians to mammals. Intriguingly, *Xenopus* differs from mammals by also concentrating manganese in cortical vesicles and releasing a significant amount of the egg's Mn^{2+} content at the time of fertilization. We find that extracellular Zn^{2+} or Mn^{2+} decreases the rate of *Xenopus* fertilization, suggesting that the triggered release of these metal ions contributes to blocking the entry of a second sperm which would be fatal to a developing embryo. The paramagnetism of Mn^{2+} allows us to glean insights into the local coordination environment of manganese within the cortical granules in ways that are not possible for its d^{10} congener Zn^{2+}. These chemical and functional insights into the inorganic chemistry of an amphibian egg expand the evolutionary context of zinc, and possibly now manganese, fluctuations as signaling events in biology.

Results

The zinc spark is conserved in amphibia

Live cell fluorescent microscopy experiments using the fluorescent zinc-responsive probe FluoZin-3 were employed to test whether zinc is released from *Xenopus* eggs upon fertilization or activation by chemical treatment. Following the addition of sperm, a single zinc release event is observed. Moreover, beginning at a single point on the oocyte surface, zinc release proceeds bidirectionally around the circumference of the egg, taking around 3 minutes to reach the opposite point (Figure 2.1A, Video A.1). The zinc spark in mammalian oocytes has been shown to be a calcium-dependent exocytosis event, and the Ca^{2+} ionophore ionomycin is known to parthenogenetically activate amphibian eggs. (92) Using these conditions as a guide, the addition of 20 μM ionomycin to frog eggs leads to a single rapid and intense release of zinc (Figure 2.1B, Video A.2). The zinc efflux induced by addition of ionomycin starts at a broad section of the circumference and travels around the circumference of the egg within approximately 30 – 90 seconds.

Figure 2.1: Zinc release from frog oocytes

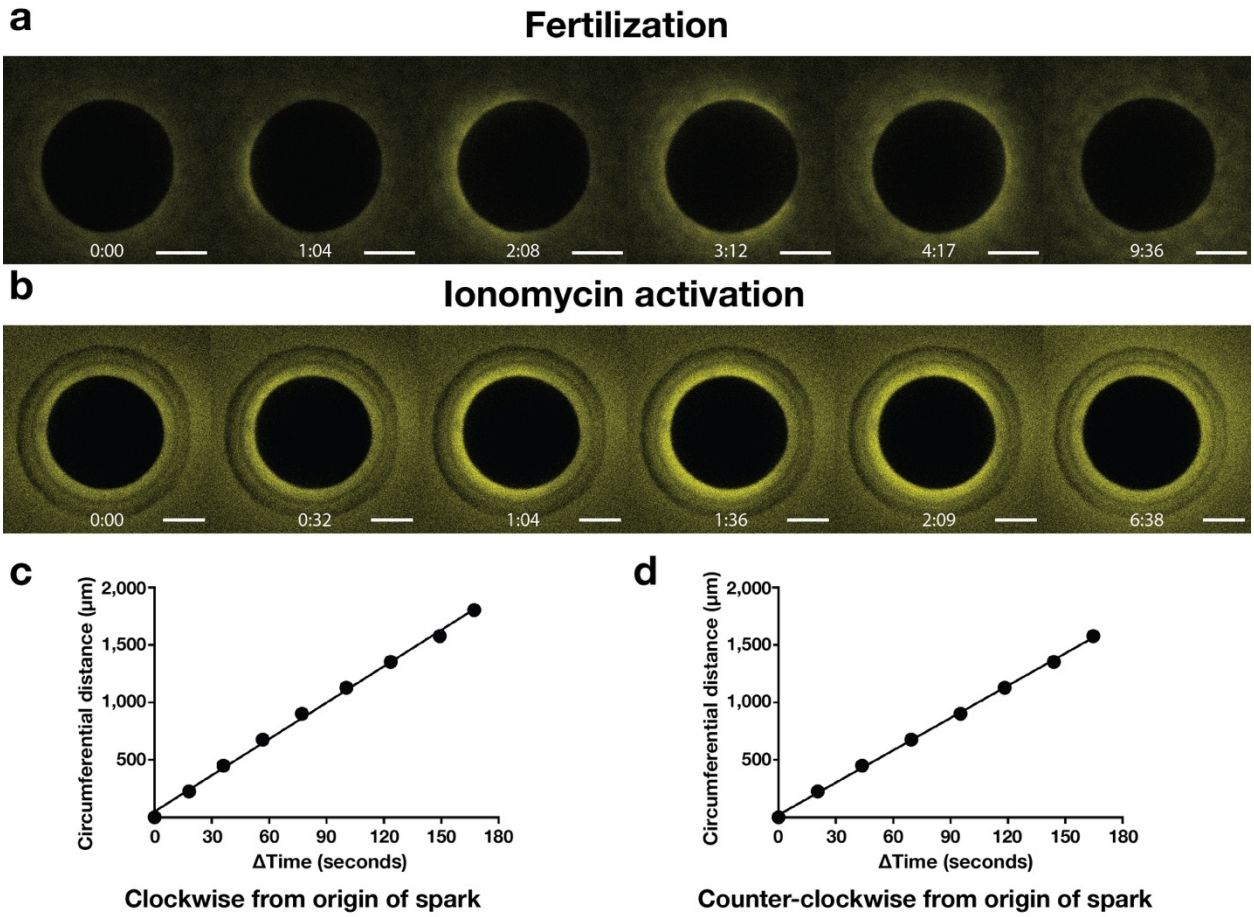

Figure 2.1: Zinc is released following both fertilization and chemical activation of a *Xenopus* egg. **a.** Zinc efflux following fertilization of a *Xenopus* egg. Images are representative of 14 eggs from 4 separate frogs over 4 independent experiments. **b.** Zinc efflux following parthenogenic activation of a *Xenopus* egg by ionomycin. Images are representative of 12 eggs from 3 separate frogs over 3 independent experiments. In both **a.** and **b.** scale bar = 500 µm, time is as m:ss, and brightness and contrast have been adjusted for clarity (see Supplemental Methods for values). **c.** Representative plot of the circumferential distance from the origin of the zinc spark at which half-maximal fluorescence is measured over the time since the start of the spark, traveling clockwise from origin. **d.** Representative plot of the circumferential distance from the origin of the zinc spark at which half-maximal fluorescence is measured over the time since the start of the spark, traveling counterclockwise from origin. **c.** and **d.** are representative of measurements from 3 separate eggs (see text for mean rate).

Upon fertilization, the zinc efflux travels approximately linearly around most of the circumference of the egg at 9.7 ± 0.3 μm/sec (n = 3, mean ± SD). Figure 2.1C and D show the rate of efflux around the circumference (see Figure 2.2 for procedure). Fertilization is known to initiate a well-established biochemical cascade leading to calcium release from intracellular stores. (93) This is apparent in the calcium wave, which travels at an average of 8.9 μm/s (66), similar to that of our observed zinc efflux. The calcium wave starts at the site of sperm entry, and travels around the egg in approximately 3.5 minutes (66), about as long as the zinc spark, suggesting that the calcium wave triggers zinc release. Zinc release in eggs activated by ionomycin is more rapid, likely because ionomycin is bringing calcium indiscriminately to all parts of the egg simultaneously, leading to a faster release of cortical granule (CG) content. Zinc is known to be a cofactor for the ZPA protease, which is released from *Xenopus* eggs and hardens the ZPA glycoprotein following fertilization, contributing to the block to polyspermy. (94) Given that the zinc-binding affinity of FluoZin-3 (K_D 9.1 nM) (95) is lower than that of most known zinc proteins (6, 96), the observed extracellular fluorescence signal is likely arising from free zinc.

Figure 2.2: Zinc spark rate

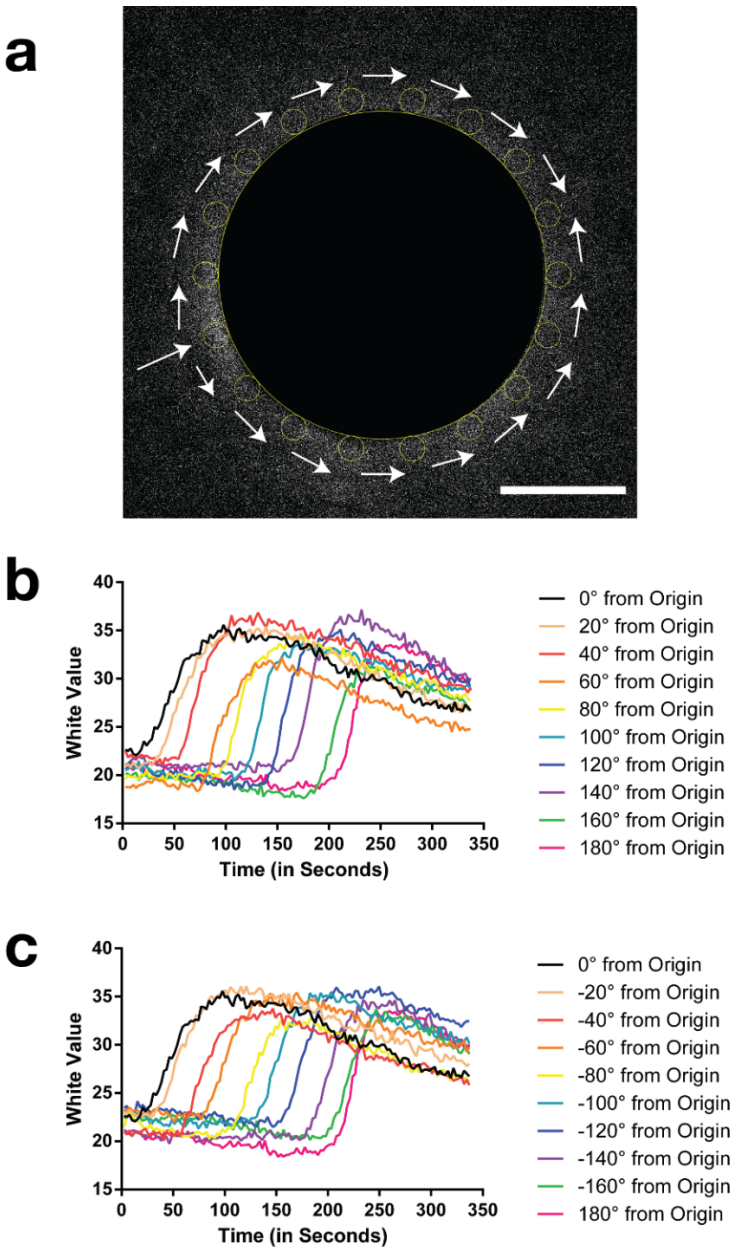

Figure 2.2: Procedure and data used for determining the rate of the zinc release. **a.** Representative image of the procedure used to measure the half-maximal fluorescence around the circumference of the egg. Scale bar = 500 μm. **b.** Graph charting fluorescence changes in sections of the egg circumference following fertilization. The graph represents Fluozin-3 fluorescence traveling clockwise from the origin of the zinc spark. **c.** Graph charting fluorescence changes in sections of the egg circumference following fertilization. The graph represents Fluozin-3 fluorescence traveling counter-clockwise from the origin of the zinc spark. **a.**, **b.**, and **c.** are representative images/graphs of n = 3 biologically independent eggs examined in a single experiment.

The change in intracellular distribution of this cofactor resulting from zinc efflux can be mimicked by treatment with intracellular metal chelating agents. In mouse eggs, treatment with these agents leads to parthenogenic egg activation supporting the conclusion that zinc efflux is necessary for activation. (7) To test whether this is true in frog as well as in mammals, *Xenopus* eggs were treated with cell-permeable chelators and scored for activation. Treatment with N,N,N',N'-tetrakis-(2-pyridylmethyl)-ethylenediamine [TPEN] does not activate frog eggs, probably due to its low solubility; however, treatment with 1,10-phenathroline (OP) activates 97 ± 5% of the eggs (Mean ± SD, n = 3. See Figure 2.3, Videos A.3 – 5). To test whether OP causes activation through lowering intracellular copper availability, eggs were treated with ammonium tetrathiomolybdate (TTM), which has a high selectivity and specificity for copper. (97) TTM did not activate the eggs (Video A.6) indicating that activation is driven by a decrease in zinc, instead of a decrease in copper availability. The absence of validated intracellular chelators that are specific for other transition metals limits our ability to address their roles in the activation of mammalian or amphibian eggs.

Figure 2.3: 1,10-Phenanthroline activates *Xenopus* eggs

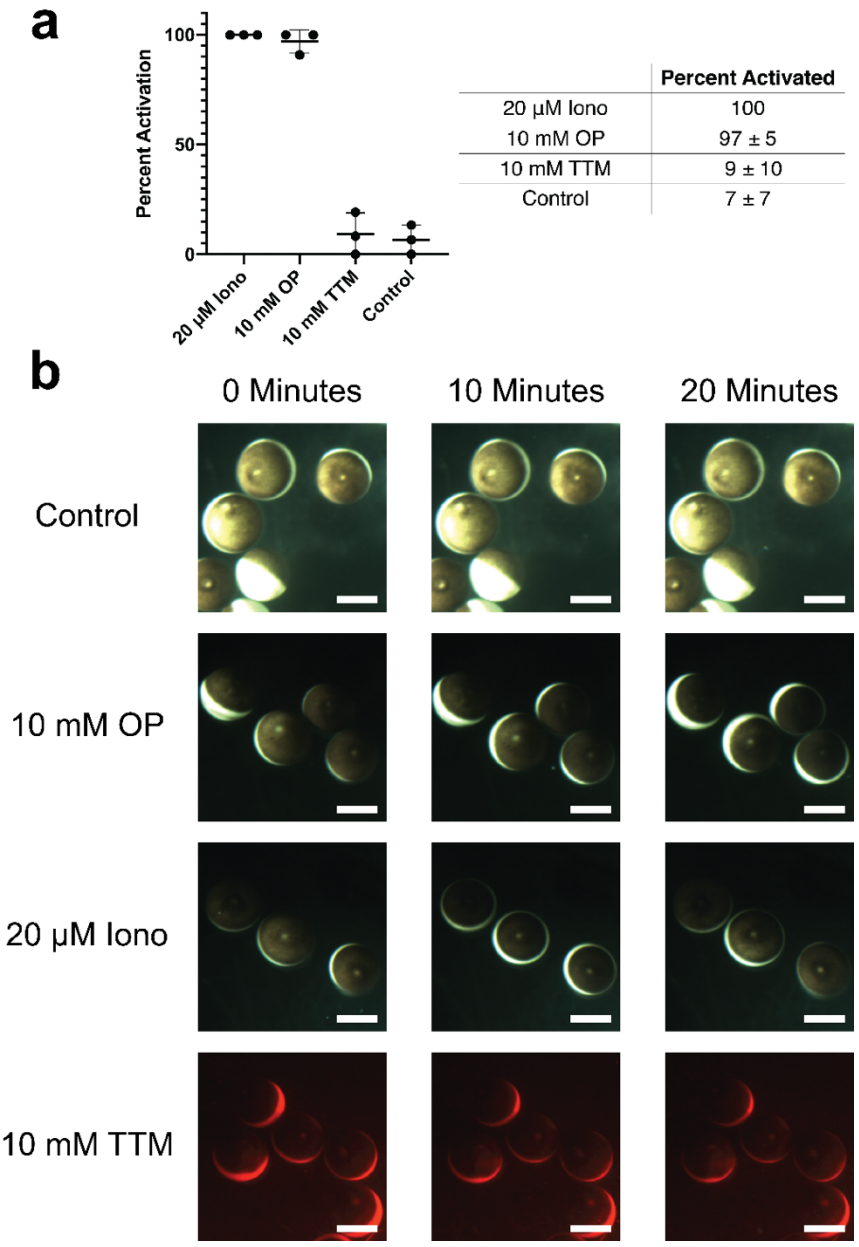

	Percent Activated
20 µM Iono	100
10 mM OP	97 ± 5
10 mM TTM	9 ± 10
Control	7 ± 7

Figure 2.3: The metal chelator 1,10-Phenanthroline parthenogenetically activates *Xenopus* eggs whereas ammonium tetrathiomolybdate does not, indicating that activation is driven by a decrease in accessible zinc. **a.** Graph of the percentage of eggs to activate 20 minutes after chemical treatment (measured by darkening and contraction of the animal pole and contraction of the activation spot). Iono: Ionomycin, OP: 1,10-Phenanthroline, TTM: Ammonium tetrathiomolybdate. Data are presented as mean ± SD, n = 3 frogs examined over 3 independent experiments (15 – 35 eggs used per datapoint). **b.** Representative images of dejellied eggs 0, 10, and 20 minutes after the addition of chemical. Scale bar = 1 mm. n = eggs from 3 separate frogs examined over 3 independent experiments.

Fertilization-induced changes in metal content

While the zinc content of mouse eggs drops circa 20% upon fertilization, a previous study using atomic absorption spectroscopy revealed no difference in the zinc content of single *Xenopus* eggs and embryos. (40) To determine whether zinc content changes immediately following fertilization, we analyzed eggs and embryos using Inductively Coupled Plasma Mass Spectrometry (ICP-MS). We compared eggs to embryos collected one-hour post-fertilization and found no statistically significant change in zinc content (Figure 2.4A).

Fluorescence optical microscopy nonetheless clearly indicates that zinc is released upon fertilization; we hypothesize that this release corresponds to only a small percentage of the total zinc contained in these large eggs. In contrast to mammalian eggs, at the time of fertilization approximately 90% of intracellular zinc in *Xenopus* eggs is found in the yolk. (41, 98) As discussed in detail below, it is not surprising that only a very small portion of intracellular zinc ions is released.

We also determined concentrations of other transition metals before and after fertilization. There was no change in the average iron or copper concentration following fertilization. However, intracellular manganese decreased by 53 ± 15% (n = 4, ± SEM) (Figure 2.4A). We did not detect changes in other elements (Figure 2.4B and Table 2.1 for values in atoms/cell). As this was an unexpected finding, we decided to probe it further.

Figure 2.4: Elemental analysis of eggs and embryos

a

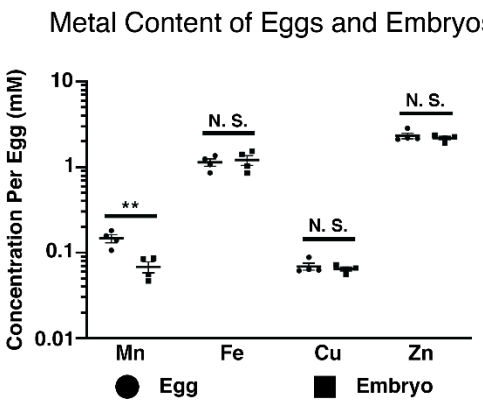

b

Elemental Content of Eggs and Embryos

	Egg (mM)	Embryo (mM)	p
Na	61 ± 2.1	61 ± 2.1	0.95
Mg	21 ± 1.1	21 ± 1.3	0.95
P	260 ± 5.4	250 ± 6.0	0.77
S	120 ± 3.2	120 ± 3.3	0.75
K	83 ± 1.1	83 ± 1.6	0.98
Ca	1.3 ± 0.036	1.2 ± 0.084	0.49
Mn	0.15 ± 0.016	0.068 ± 0.010	0.0081
Fe	1.1 ± 0.11	1.2 ± 0.16	0.72
Cu	0.069 ± 0.0064	0.065 ± 0.0035	0.56
Zn	2.3 ± 0.17	2.2 ± 0.10	0.52

Mean ± SEM. n = 4 frogs

Figure 2.4: ICP-MS measures a significant decrease in intracellular manganese post-fertilization. **a.** Metal concentrations of *Xenopus* eggs and embryos (1 hour post-fertilization) determined by ICP-MS. Intracellular Co and Ni are both below 13 μM. Data are presented as mean ± SEM per egg/embryo, **: **p** = 0.0081. Each point corresponds to ICP-MS analysis of a batch of 20 eggs normalized to a per egg basis. Similar results were obtained in 6 separate experiments (not shown). **b.** Elemental contents (mM) of *Xenopus* eggs and embryos (1-hour post-fertilization). Experimental conditions as in **a**. In both **a.** and **b.** n = samples from 4 separate frogs analyzed in a single ICP experiment. **p** is the significance of the change in elemental content following fertilization. Two-tailed, heteroscedastic T-tests were run between eggs and embryos in order to determine if there was a significant difference in metal content. No adjustments were made for multiple comparisons.

Table 2.1: Elemental content of *Xenopus* eggs and embryos from ICP

	Egg (Atoms)	Embryo (Atoms)
Na	$3.7 \pm 0.12 \times 10^{16}$	$3.7 \pm 0.13 \times 10^{16}$
Mg	$1.3 \pm 0.065 \times 10^{16}$	$1.3 \pm 0.077 \times 10^{16}$
P	$1.5 \pm 0.033 \times 10^{17}$	$1.5 \pm 0.036 \times 10^{17}$
S	$7.1 \pm 0.19 \times 10^{16}$	$7.0 \pm 0.20 \times 10^{16}$
K	$5.0 \pm 0.065 \times 10^{16}$	$5.0 \pm 0.094 \times 10^{16}$
Ca	$7.8 \pm 0.22 \times 10^{14}$	$7.4 \pm 0.51 \times 10^{14}$
Mn	$8.8 \pm 0.94 \times 10^{13}$	$4.1 \pm 0.60 \times 10^{13}$
Fe	$6.8 \pm 0.66 \times 10^{14}$	$7.3 \pm 0.95 \times 10^{14}$
Cu	$4.2 \pm 0.39 \times 10^{13}$	$3.9 \pm 0.21 \times 10^{13}$
Zn	$1.4 \pm 0.11 \times 10^{15}$	$1.3 \pm 0.061 \times 10^{15}$

Table 2.1: Elemental contents of *Xenopus* eggs and embryos (1 hour post-fertilization) in atoms/cell. Data obtained from ICP-MS and ICP-OES. 20 egg/embryos per tube, values reported as mean ± SEM per egg/embryo. n = samples from 4 separate frogs analyzed in a single ICP experiment.

The coordination environment of manganese

Intracellular manganese is predominantly present in the +2 oxidation state. (99, 100) The majority of that is found in kinetically labile complexes with low molecular-weight metabolites, (101-104) but it is also bound as a cofactor in a number of enzymes. (105) Mn^{2+} is paramagnetic (S=5/2), and we employ a combination of Electron-Paramagnetic Resonance (EPR), Electron-Nuclear Double-Resonance (ENDOR) and Electron Spin-Echo Envelope Modulation (ESEEM) spectroscopies, complementary means of obtaining an NMR spectrum of the ligands to a paramagnetic metal ion (see Supplemental Methods), to determine the relative populations of the different Mn-ligand complexes present in intact eggs before and after fertilization. (101-103)

The absorption-display continuous-wave (CW) EPR spectrum of frozen intact eggs and embryos provides a well resolved six-line pattern created by the hyperfine interaction of the electron spin with ^{55}Mn nuclear spin ($I = 5/2$). This pattern is centered at g-2 (~12 kG), and rides

on relatively narrow "wings" (Figure 2.5A and see Supplemental Methods); the latter are suppressed in derivative-mode CW EPR spectra (inset). This pattern is typical of Mn^{2+} coordinated in high-symmetry (roughly octahedral) geometry, as seen for small Mn-metabolite complexes like Mn-phosphate (Mn-Pi). Broad "wings" associated with asymmetric Mn^{2+} chelate and enzyme environments (i.e. MnSOD) (103, 104) are absent in the spectra of *Xenopus* eggs and embryos. The shape of the Mn^{2+} EPR spectrum of the embryos is unchanged from that of the eggs (Figure A.3) but the amplitude of the embryo signal is about one-third that of the eggs (~30 $\pm$ 10% remaining; see Figure 2.5, legend, and Supplemental Methods). Given that the spectra have the same shape, their relative amplitudes are an appropriate measure of Mn^{2+} present. The decrease in EPR amplitude upon fertilization agrees with the loss of Mn measured by ICP-MS (Figure 2.4), within the mutual uncertainties of the measurements, together showing that the egg loses Mn^{2+} upon fertilization.

Figure 2.5: Paramagnetic resonance measurements of eggs and embryos

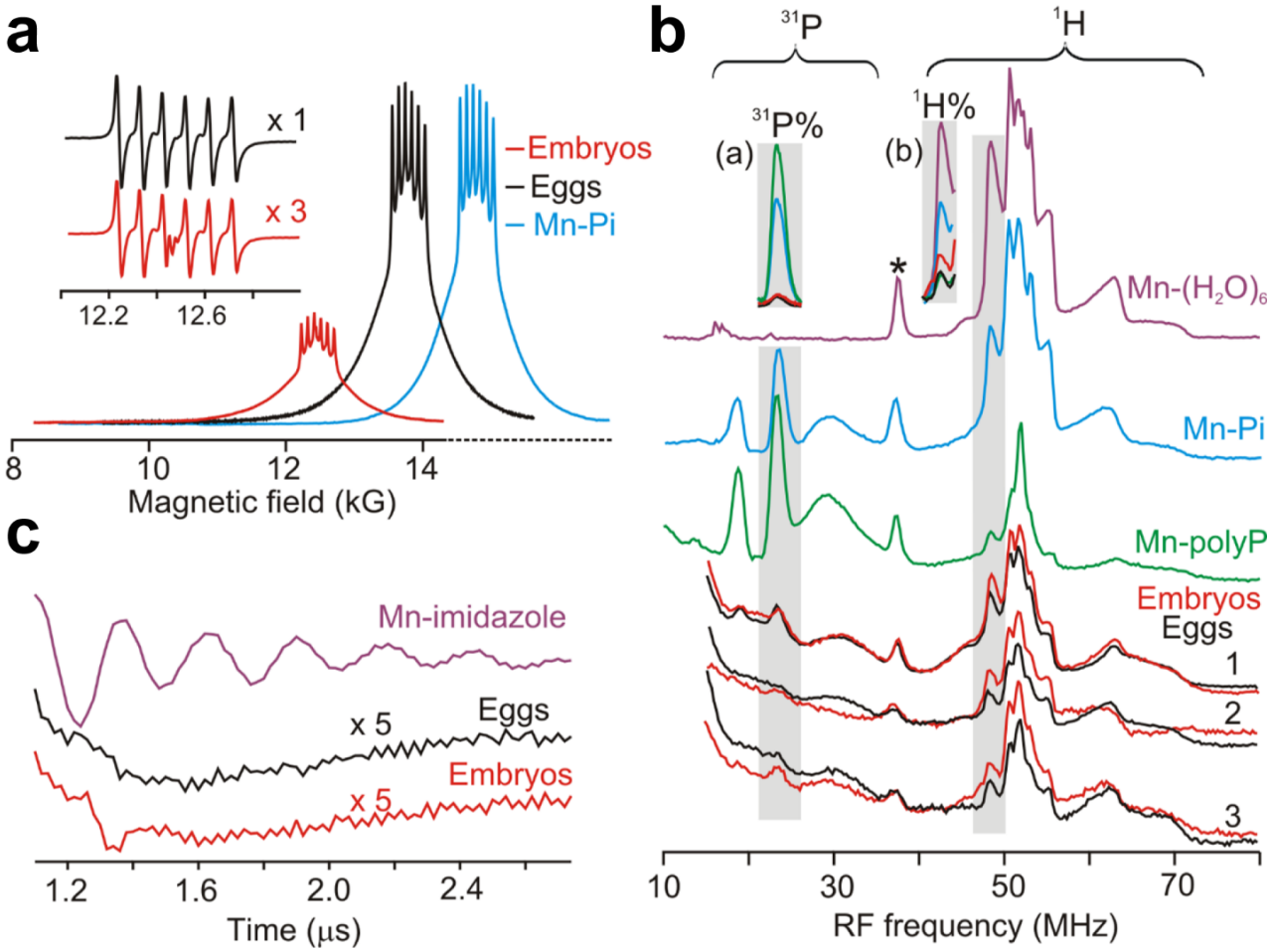

Figure 2.5: EPR confirms a post-fertilization decrease in manganese, while EPR, ENDOR, and ESEEM demonstrate that the majority of intracellular manganese is bound to a low molecular weight carboxylate. 35-GHz, 2K EPR/ENDOR/ESEEM Spectra: **a.** Representative absorption-display CW-EPR spectra of Mn^{2+} in: frog eggs (black); embryos (red; 1/3 amplitude of eggs, ~30 ± 10% remaining, see text); Mn-orthophosphates Mn-Pi (blue; scaled to eggs); EPR spectra of frog eggs/Mn-Pi offset by 500G/1000G. *Inset:* Digital derivatives of spectra accentuating g-2 (~12 kG) six-line ^{55}Mn hyperfine pattern. **b.** $^{31}P/^{1}H$ Davies pulsed-ENDOR spectra of: intact frog eggs and embryos; solution Mn^{2+} complexes (aquo [H_2O], orthophosphate [Pi], polyphosphate [polyP]). Braces represent frequency ranges of ^{31}P and ^{1}H ENDOR signals. ENDOR spectra are normalized to Mn^{2+} concentration; thus $^{31}P\%$, $^{1}H\%$ peaks (gray highlight) represent absolute ENDOR responses. *Insets:* (a) $^{31}P\%$ ENDOR responses of exemplars and eggs/embryos from frog 3; (b) corresponding $^{1}H\%$ ENDOR responses. (* is a ^{55}Mn ENDOR signal) **c.** ^{14}N 3-pulse ESEEM timewaves of: eggs (black); embryos (red), each multiplied by 5 for ease of comparison; solution Mn-imidazole complex (purple). *Experimental conditions:* see Supplemental Methods (**b, c**, Fields ~ 12.5k G**).** In **a.**, **b.**, and **c.** n = 3 biologically independent replicates of intact frog eggs and embryos examined over 3 independent experiments.

ENDOR and ESEEM were used to determine the intracellular speciation of the Mn^{2+}. Figure 2.5B shows 35 GHz pulsed ENDOR spectra of eggs and embryos (triplicates) and selected exemplar Mn^{2+} complexes (hexa-aquo Mn^{2+} and the Pi, and polyphosphate [polyP]). The $[Mn(H_2O)_6]^{2+}$ sample shows a strong ^{1}H ENDOR response with multiple peaks centered at the ^{1}H Larmor frequency (shown under the ^{1}H 'brace') assigned to directly-coordinated water molecules. (106) When a metabolite moiety such as a phosphate binds to Mn^{2+} it replaces coordinated water(s), decreasing the ^{1}H ENDOR amplitude. When a phosphate binds, this also introduces a ^{31}P ENDOR doublet, split by the electron-nuclear interaction and centered at the ^{31}P Larmor frequency (shown under the 'brace' ^{31}P). In Mn-polyP complexes, multiple phosphates bind, most of the waters are displaced, as shown by the large reduction of ^{1}H ENDOR signal, and there is an even greater increase in ^{31}P ENDOR signal (Figure 2.5B). When the amplitudes of the ^{31}P, ^{1}H ENDOR peaks shown in Figure 2.5B as gray stripes are normalized to the corresponding Mn^{2+} concentrations they are denoted as absolute ENDOR responses and labelled as $^{31}P\%$, $^{1}H\%$. These responses can be used in a heuristic model of Mn^{2+} ligand binding described previously (102) to estimate fractions of aquo, Pi, polyP, and ENDOR-silent (e.g. carboxylate) complexes (see SI).

In comparison to the exemplars, both eggs and embryos show weak ^{31}P signals (inset a), indicating little Pi/polyP ligation, and a weak $^{1}H\%$ ENDOR response (inset b), yet indicating a high population of ligands that displace H_2O. To test for Mn^{2+} ligation by nitrogenous ligands we used 35 GHz ESEEM spectroscopy, which is a very sensitive probe towards such ligation (101-104); Figure 2.5C shows that the ESEEM time-wave for a frozen solution of Mn^{2+}-imidazole exhibits strong modulation whose frequency corresponds to ^{14}N resonance frequencies. Neither eggs nor embryos show any ^{14}N modulation of the time-waves in the 35 GHz ESEEM traces, indicating the absence of any detectable Mn-N complexes. Together, these observations indicate

that the majority of the intracellular Mn^{2+} coordination sites (i.e. between 75-90%) in both eggs and embryos are occupied by ENDOR (NMR)-silent ligands, and when an organism is grown with natural abundance ^{12}C nutrients, carboxylates are the major class of such ligands. We conclude that the majority Mn^{2+} population in the eggs and embryos can be assigned as low molecular-weight Mn^{2+} complexes with carboxylate ligands (Mn-C 75-90%).

Disruption of eggs exposes compartmentalized Mn^{2+} complexes to cytoplasmic concentrations of phosphate and phosphoryl ligands which are typically in the millimolar concentration range. (107) As a result, scrambling induces a 20% increase in the Mn-P population (Figure 2.6 and Supplemental Methods). Taken together, the ENDOR measurements are consistent with a model in which a majority of the EPR-detectable Mn^{2+} is sequestered as manganese-carboxylate in non-cytosolic compartments in the egg, and that these complexes are released from the egg upon fertilization without change in speciation of the remaining Mn^{2+}. To test for the presence of Mn- and Zn-enriched compartments in these eggs we turned to two subcellular methods for mapping the locations of elements in cells.

Figure 2.6: Coordination environment of manganese

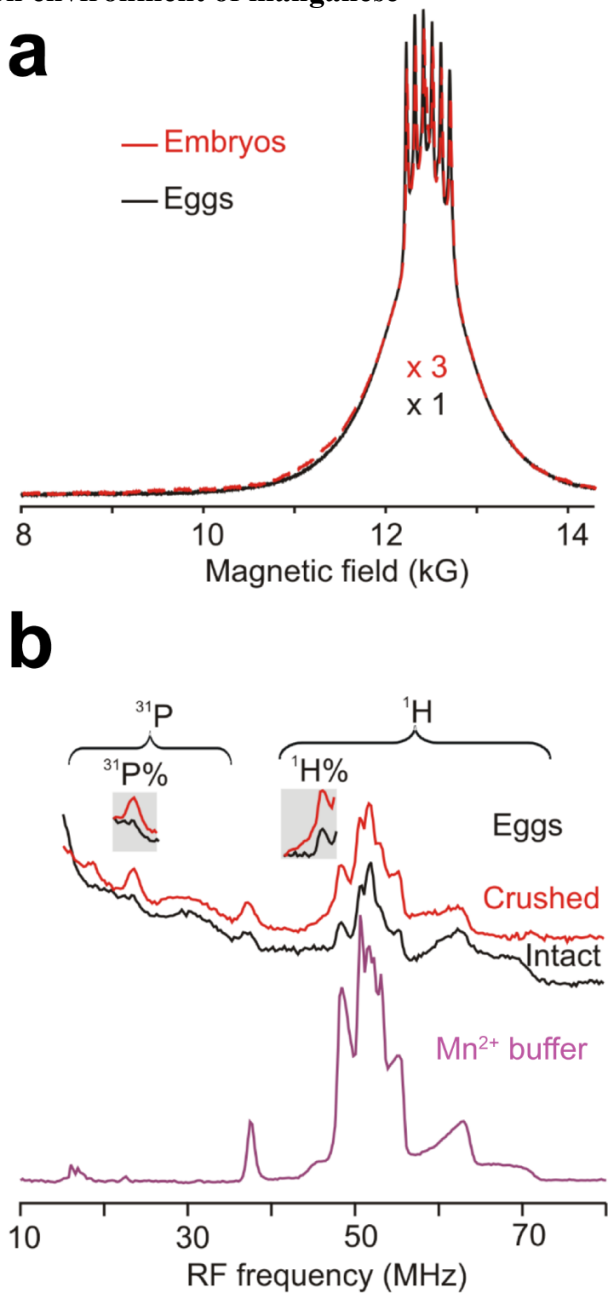

Figure 2.6: Manganese has similar coordination environments in both eggs and embryos; freezing *Xenopus* eggs does not alter manganese coordination. **a.** Overlay of the EPR spectra of eggs (black) and embryos (red); the shape of the embryo signal is unchanged from that of the egg. This is a representative experiment of n = 3 biologically independent samples examined over 3 independent experiments. **b.** Intentionally destroying *Xenopus* eggs significantly changes their ENDOR spectra, demonstrating that freezing the eggs does not affect the vesicular compartmentalization of manganese. ^{31}P, ^{1}H Davies pulsed ENDOR spectra of intact (black), crushed (red) frog eggs and frozen solution of Mn-spiked buffer (purple). Experimental conditions as in Figure 2.5B. n = 1 biologically independent sample.

XFM reveals cortical metal compartmentalization

X-ray Fluorescence Microscopy (XFM) (108) methods indicated that cortical vesicles in mouse eggs contain on average one million zinc ions each (6) and we employed this approach to test for the presence of analogous zinc- and manganese-enriched sites in small sections at the cortices of *Xenopus* eggs and embryos. To preserve transition metal contents in our samples we used a modified form of Timm's silver staining. (6, 88, 90) ICP-MS reveals that this fixation method preserves native metal contents in *Xenopus* eggs, except for iron, which showed a significant gain in concentration, due to contamination in the fixative (Seeler et al., in preparation). We analyzed ultramicrotome slices of the animal pole (AP) and vegetal pole (VP) of eggs and embryos, ranging from 0.4 to 2 μm thick. The cortical ultrastructure of the AP and VP are significantly different. (109) We find that metal content and localization differ in the poles as well (Figures 2.7-2.9). We conclude that in *Xenopus* eggs, zinc is loaded to high concentrations in the smaller group of cortical vesicles that are analogous to those found in murine, bovine and primate eggs. (7, 15, 16)

Figure 2.7: Synchrotron-based X-ray fluorescence mapping of animal pole egg and embryo cortices

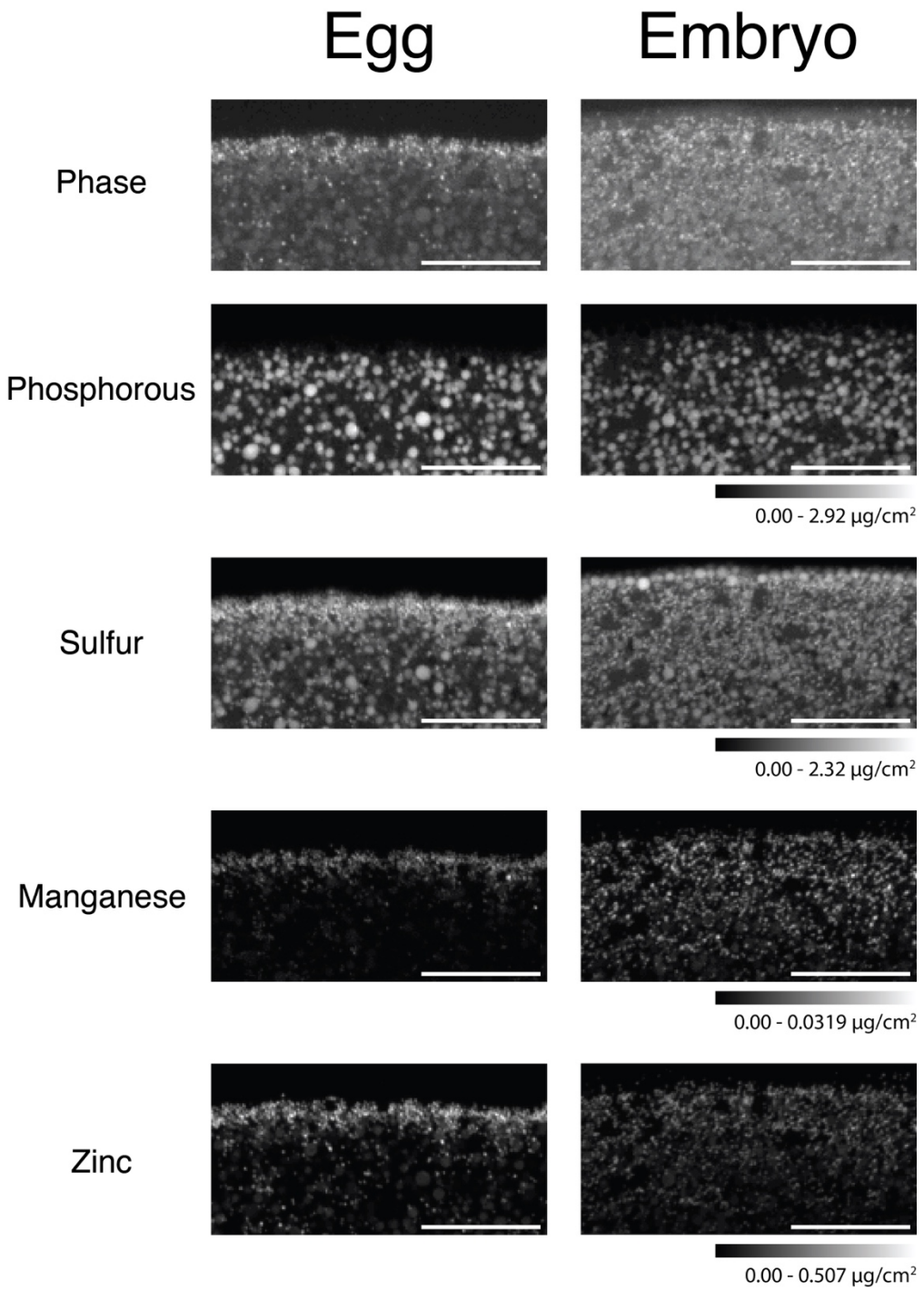

Figure 2.7: X-ray fluorescence microscopy images of the animal pole of fixed *Xenopus* egg/embryo slices show zinc and manganese are localized in small cortical compartments. Scale bar = 20 µm. Images acquired at Beamline 2-ID-D at Argonne National Laboratory. Pixel size: 300 x 300 nm, slice thickness: 2 µm, scan time: 500 ms/pixel. These are representative images of slices of eggs/embryos from 7 different frogs imaged over 3 experiments.

Figure 2.8: Synchrotron-based X-ray fluorescence mapping of animal pole egg and embryo cortices

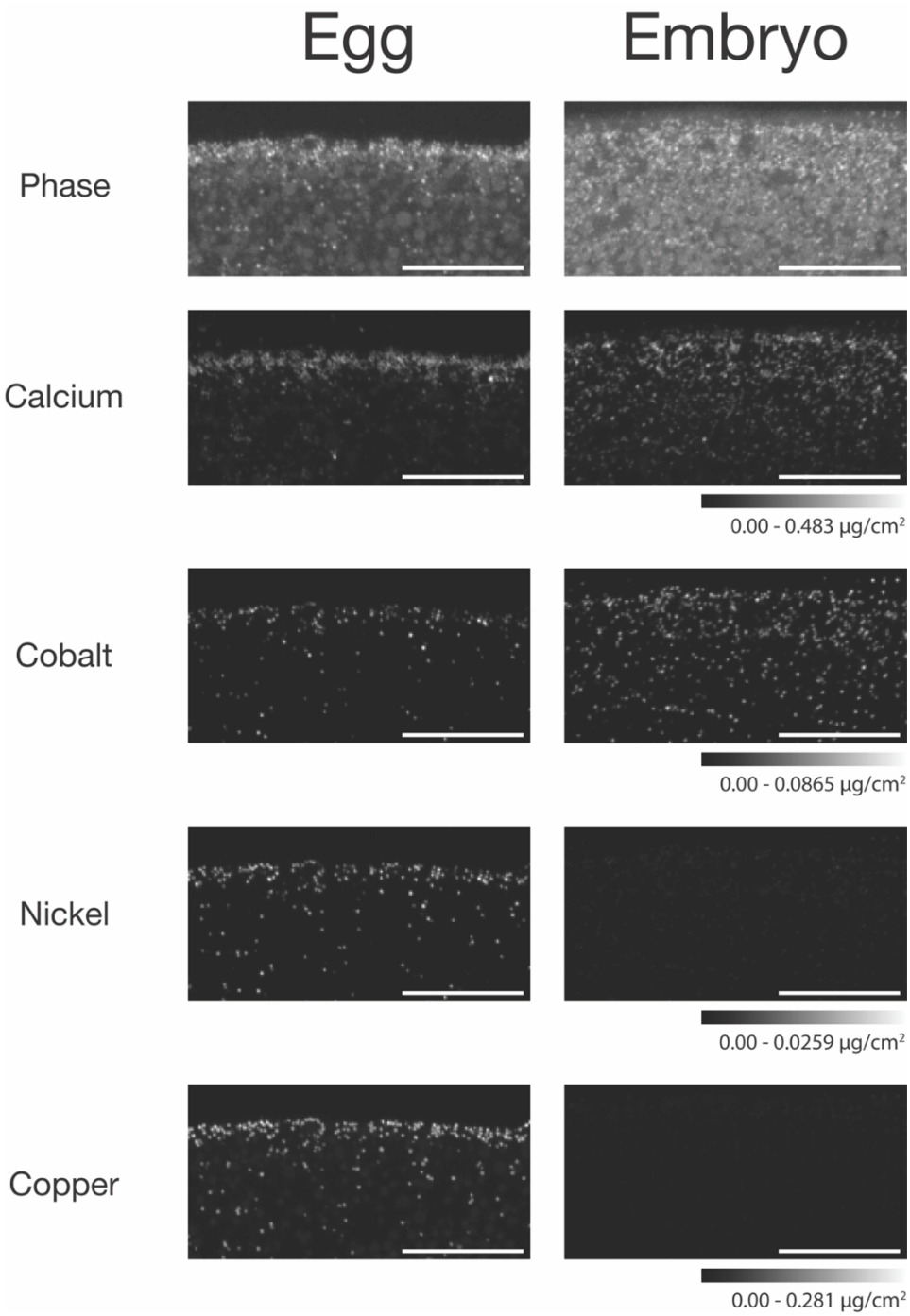

Figure 2.8: X-ray fluorescence microscopy images of the animal pole of fixed *Xenopus* egg/embryo slices showing metal localization in small compartments. Scale bar = 20 µm. Images acquired at Beamline 2-ID-D at Argonne National Laboratory. Pixel size: 300 x 300 nm, slice thickness: 2 µm, scan time: 500 ms/pixel. These are representative images of slices of eggs/embryos from 7 different frogs imaged over 3 experiments.

Figure 2.9: Synchrotron-based X-ray fluorescence mapping of vegetal pole egg and embryo cortices

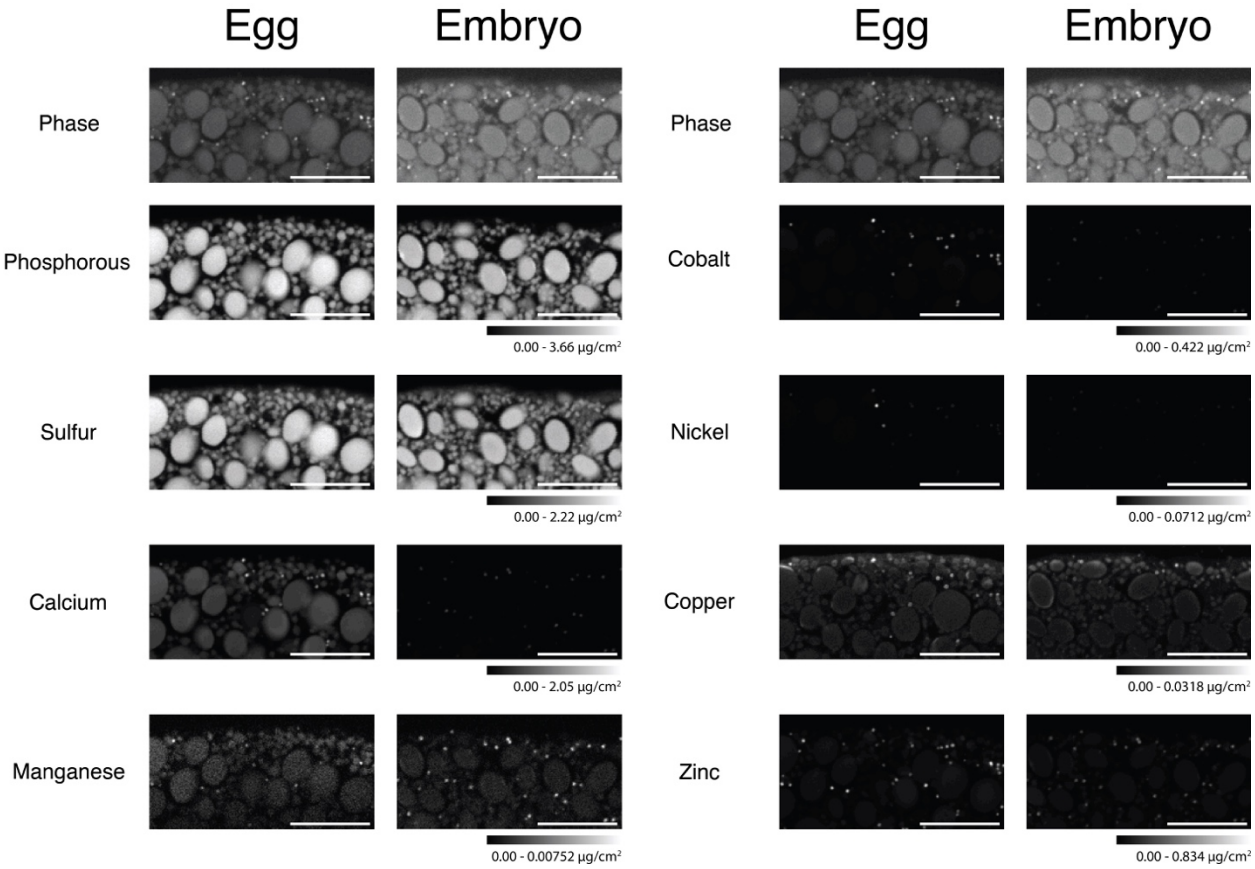

Figure 2.9: X-ray fluorescence microscopy images of the vegetal pole of fixed *Xenopus* egg/embryo slices. The yolk platelets show high phosphorous and sulfur content. Metals are localized to small compartments, however there are far fewer than in the animal pole. Scale bar = 20 µm. Images acquired at Beamline 2-ID-D at Argonne National Laboratory. Pixel size: 300 x 300 nm, slice thickness: 2 µm, scan time: 500 ms/pixel. These are representative images of slices of eggs/embryos from 7 different frogs imaged over 3 experiments.

We find two classes of metal-containing compartments: the smaller ones are far more abundant in the AP than the VP. Fitting the XFM data reveals that metals are localized in compartments at millimolar-scale concentrations. Figure 2.10A presents the XFM values as $\mu g/cm^2$ next to an estimate of the minimal molar concentration in each site. The conversion to mM was obtained through estimates of the number of atoms in each voxel, as the sample thickness is known (see SI for more detail). There is some variation in the metal content of these compartments,

though some of this is because slices of eggs were analyzed, so compartments may represent sections or combinations of what we assume to be vesicles (Figure 2.10B and C). There is significant metal concentration in these compartments: Mn concentration is approximately 30X higher in the compartments compared to the entire volume of the egg (see Figure 2.4B), Cu is 150X, and Zn is 10X.

Figure 2.10: Animal pole egg metal compartment contents

a

	Average µg/cm²	Voxel Concentration (mM)
Mn	$4.0 \pm 1.1 \times 10^{-3}$	2 ± 0.5
Co	$5.9 \pm 6.7 \times 10^{-3}$	3 ± 3
Ni	$6.7 \pm 1.7 \times 10^{-4}$	0.3 ± 0.07
Cu	$2.4 \pm 1.5 \times 10^{-2}$	10 ± 6
Zn	$5.0 \pm 0.66 \times 10^{-2}$	20 ± 3

Mean ± SD. N = 3 frogs

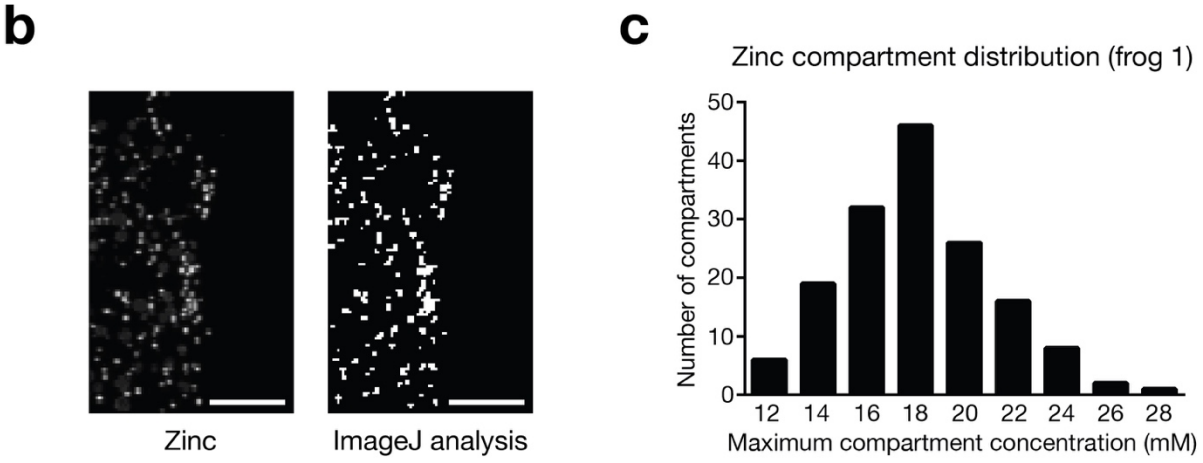

Figure 2.10: Metals are stored at millimolar concentrations in the cortical compartments. **a.** Concentrations of metal compartments in the egg animal pole. Voxel size 300 x 300 x 400 nm. Data acquired at Beamline 2-ID-D, Argonne National Laboratory. Values reported as mean ± SD, n = 3 slices of eggs analyzed from separate frogs examined over 2 independent experiments. **b.** Representative image of zinc distribution and thresholding of areas of high zinc concentration. Scale bar = 10 µm. Images acquired at Beamline 2-ID-D at Argonne National Laboratory. Pixel size: 300 x 300 nm, slice thickness: 400 nm, scan time: 500 ms/pixel. **c.** Representative plot of the zinc concentration distribution of small metal compartments found in a slice. n = 156 compartments.

The second class of metal-containing compartments is larger and contains a lower concentration of metal. These are likely yolk platelets. Yolk consists of two proteins: lipovitellin, which binds zinc, and phosvitin, which contains 25% phosphoserine. (42) These compartments are also larger in the VP cortex than the AP (110), further supporting this assignment. Besides zinc and to an extent copper, transition metals are at very low concentrations in the yolk platelets (Table 2.2).

Table 2.2: Yolk platelet elemental content

	Mean µg/cm^2	**Voxel Concentration (mM)**
P*	0.20 ± 0.025	2 ± 0.2 x 10^2
Ca	1.2 ± 0.24 x 10^{-2}	7 ± 1
Mn	9.8 ± 3.5 x 10^{-4}	0.4 ± 0.2
Co	3.6 ± 3.5 x 10^{-4}	0.2 ± 0.1
Ni	2.0 ± 0.17 x 10^{-4}	8 ± 0.7 x 10^{-2}
Cu	4.7 ± 2.8 x 10^{-3}	2 ± 1
Zn	1.6 ± 0.20 x 10^{-2}	6 ± 1

*: Note this is a minimum value, as there is phosphorous loss during fixation (Figure 3.2)

Table 2.2: Elemental concentrations of larger elemental compartments in the egg animal pole. Voxel size 0.3 x 0.3 x 2 µm. Data acquired at Beamline 2-ID-D, Argonne National Laboratory. Values reported as mean ± SD, n = 3 biologically independent samples examined over 2 independent experiments.

Unlike mammalian eggs, we find other metals in addition to zinc localized to the *Xenopus* egg cortex. To determine the extent of metal co-localization, Pearson coefficients were calculated. The egg AP sections had the highest number of significant correlations with low variability (Figure 2.11). Two main elemental groupings with high Pearson coefficients (0.64 – 0.92) are observed. The first is cobalt, copper, and nickel, and the second is calcium, manganese and zinc. A possible

source of metals with little or no known biological role in vertebrates (e.g. cobalt and nickel) is the water in which the animals are housed. Water from frog tanks was analyzed by ICP-MS and transition metals were found to be at approximately nanomolar concentrations (Table 2.3).

Figure 2.11: Metal overlay in cortical compartments

a

Ca	Mn	Co	Ni	Cu	Zn	
1	0.92 ± 0.017	0.46 ± 0.32	0.36 ± 0.21	0.35 ± 0.22	0.82 ± 0.072	Ca
	1	0.49 ± 0.30	0.37 ± 0.26	0.36 ± 0.22	0.80 ± 0.12	Mn
		1	0.77 ± 0.072	0.64 ± 0.16	0.53 ± 0.30	Co
			1	0.65 ± 0.070	0.51 ± 0.11	Ni
				1	0.46 ± 0.25	Cu
					1	Zn

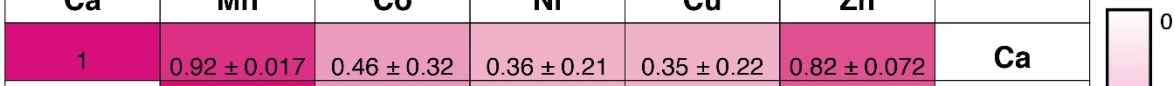

b

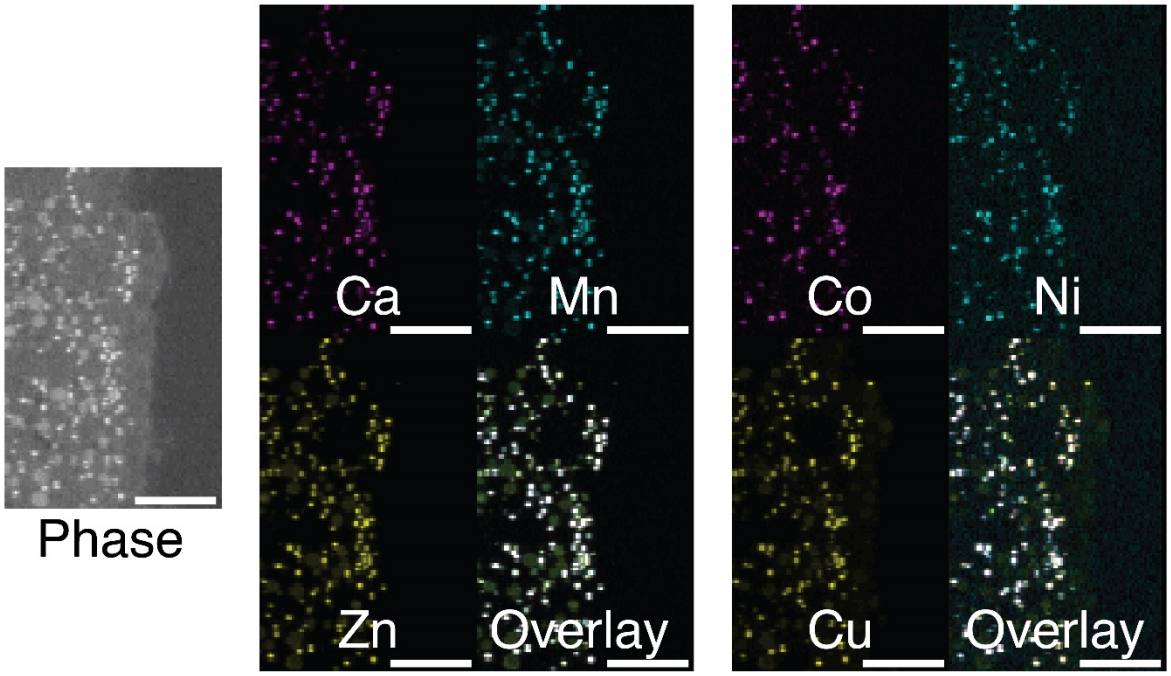

Figure 2.11: Metals cluster in the small cortical compartments. Cobalt, copper, and nickel group together as well as calcium, manganese and zinc. **a.** Pearson coefficients of elemental overlap in the egg animal pole. Data are presented as mean ± SD. n = 4 (for Mn, Co, Cu, and Zn) and n = 3 (for Ca and Ni because of contamination in a sample) biologically independent samples examined over 2 independent experiments. **b.** Representative X-ray fluorescence microscopy images of fixed *Xenopus* egg/embryo slices showing elemental overlap. Scale bar = 10 µm. Images acquired at Beamline 2-ID-D at Argonne National Laboratory. Pixel size: 300 x 300 nm, slice thickness: 400 nm, scan time: 500 ms/pixel.

Table 2.3: Elemental content of frog tank water

Element	Concentration (M)	n
Na	0.20 ± 0.024	3
Mg	$2.9 \pm 0.025 \times 10^{-2}$	3
P	$2.4 \pm 0.061 \times 10^{-3}$	3
K	$6.4 \pm 0.046 \times 10^{-3}$	3
Ca	$7.6 \pm 0.027 \times 10^{-3}$	3
V	$1.8 \pm 0.076 \times 10^{-9}$	6
Cr	$4.6 \pm 3.4 \times 10^{-10}$	6
Mn	$1.3 \pm 0.21 \times 10^{-9}$	6
Fe	$3.8 \pm 0.39 \times 10^{-8}$	6
Co	$3.5 \pm 0.12 \times 10^{-10}$	6
Ni	$<1.1 \times 10^{-9}$	6
Cu	$8.5 \pm 0.16 \times 10^{-9}$	6
Zn	$8.2 \pm 0.092 \times 10^{-8}$	6
As	$1.1 \pm 0.11 \times 10^{-9}$	6
Se	$7.8 \pm 0.45 \times 10^{-10}$	6
Mo	$2.4 \pm 0.15 \times 10^{-9}$	6

Table 2.3: Elemental content of frog tank water measured by ICP-MS. Values are in M and presented as mean ± SD. n is the number of tubes of water analyzed by ICP (in order to take into account variation in sample preparation/detection).

While XFM provides very high elemental sensitivity, the spatial resolution at 2-ID-D (300 x 300 nm pixels) does not allow for high resolution imaging of the metal-enriched sites. Thus, additional high-resolution elemental mapping methods were employed to characterize these sites.

AEM demonstrates metal vesicular localization

To assess whether these sites represented metal-enriched vesicle structures, nanometer resolution images were obtained using state-of-the-art Analytical Electron Microscopy (AEM) which combines Scanning Transmission Electron Microscopy (STEM) with X-ray Energy Dispersive Spectroscopy (XEDS). (111) Images were obtained using 150 nm-thick sections of eggs and embryos. Similar to the XFM data, AEM revealed two classes of vesicle, with the smaller ones containing multiple metals, and the larger ones containing primarily phosphorous and sulfur, with very low concentrations of the other elements examined (Figure 2.12A and B). Ca, Mn, Co, Ni, Cu, and Zn are found in the smaller class of electron-dense vesicle (Figure 2.12C). The average diameter of the small vesicle in the egg AP is 490 ± 56 nm (mean ± SD, n = 50) (Figure 2.12D). These images concur with our XFM findings. There are fewer small vesicles in the animal pole embryo than in the egg (Figure 2.13). Both the vegetal pole egg (Figure 2.14) and vegetal pole embryo (Figure 2.15) show large yolk platelets and few of the small vesicles.

Figure 2.12: Analytical electron microscopic analysis of egg animal pole cortical vesicles

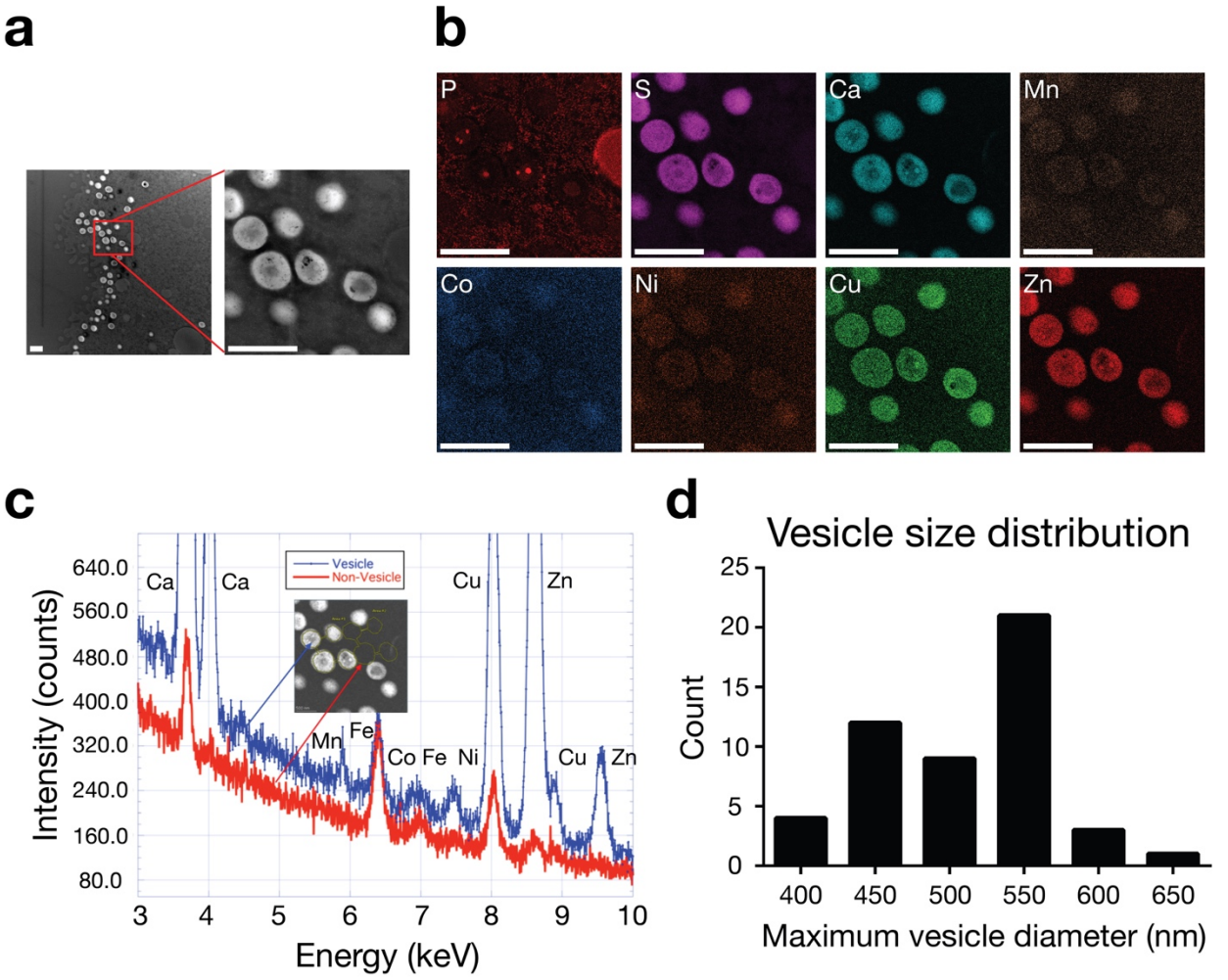

Figure 2.12: AEM demonstrates that multiple metals are stored in sub-micrometer vesicles in the animal pole. **a.** High Angle Annular Dark Field Scanning Transmission Electron Microscopy (HAADF-STEM) images of the cortex of the animal pole of a fixed *Xenopus* egg. **b.** Hyperspectral elemental intensity distribution maps: background corrected, with a 0.7-pixel gaussian blur, no normalization, no quantification. Same conditions as in **a**. Scale bar = 1 µm in both **a.** and **b**. These are representative images of 3 separate scans. **c.** Cumulative XEDS spectra confirming the presence of Ca, Mn, Co, Ni, Cu, and Zn in vesicles. These comparison spectra are obtained by summing individual spectra from an identical number of pixels in regions of interest which correspond to vesicle and neighboring non-vesicle areas. **d.** Histogram of vesicle diameter distribution from image in **a**. n = 50 vesicles measured.

Figure 2.13: Analytical electron microscopic analysis of embryo animal pole cortical vesicles

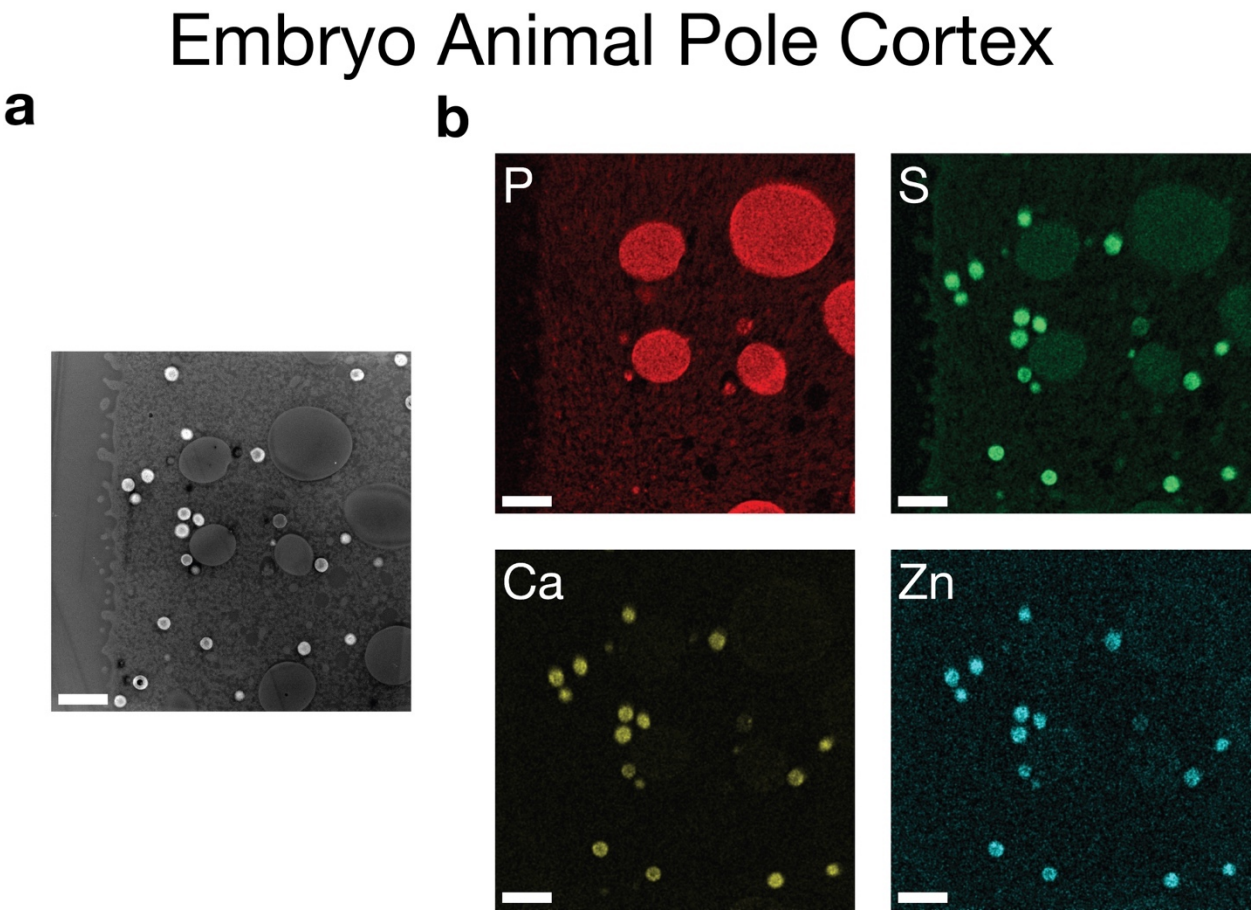

Figure 2.13: The cortex of the animal pole embryo has small zinc-containing vesicles as well as yolk platelets. **a.** HAADF-STEM images of the cortex of the animal pole of a fixed *Xenopus* embryo. **b.** Hyperspectral elemental intensity distribution maps, background corrected, gaussian blur at 3 pixels, no normalization, no quantification. Same conditions as in **a**. Scale bar = 2 µm in both **a.** and **b**. These are representative images of 2 separate scans.

Figure 2.14: Analytical electron microscopic analysis of embryo animal pole cortical vesicles

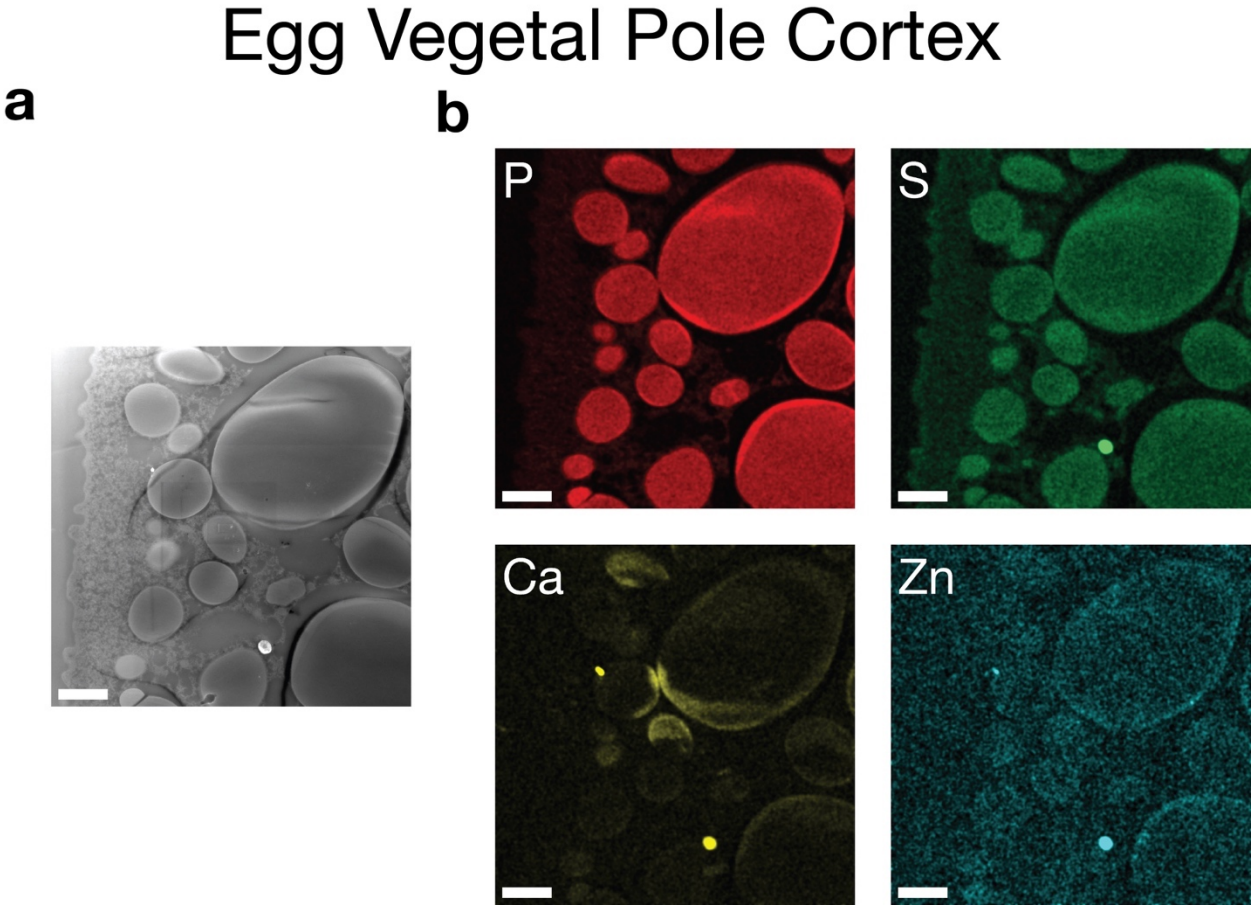

Figure 2.14: The egg vegetal pole mostly contains yolk platelets. **a.** HAADF-STEM images of the cortex of the vegetal pole of a fixed *Xenopus* egg. **b.** Hyperspectral elemental intensity distribution maps, background corrected, gaussian blur at 3 pixels, no normalization, no quantification. Same conditions as in **a**. Scale bar = 2 μm in both **a.** and **b**. These are results from a single AEM experiment.

Figure 2.15: Analytical electron microscopic analysis of embryo animal pole cortical vesicles

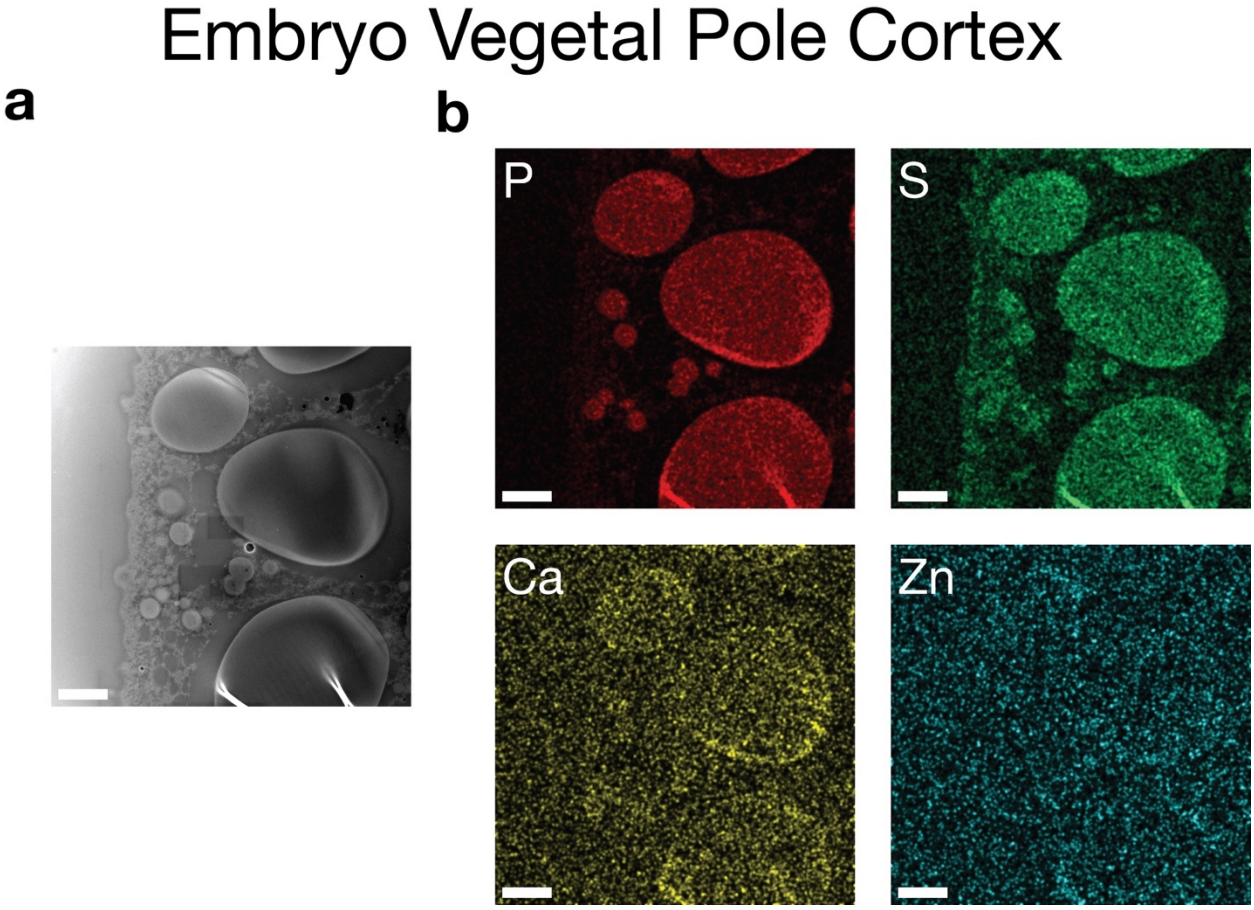

Figure 2.15: The embryo vegetal pole mostly contains yolk platelets. **a.** HAADF-STEM images of the cortex of the vegetal pole of a fixed *Xenopus* embryo. **b.** Hyperspectral elemental intensity distribution maps, background corrected, gaussian blur at 3 pixels, no normalization, no quantification. Same conditions as in **a**. Scale bar = 2 µm in both **a.** and **b**. These are results from a single AEM experiment.

Using TEM images of sections of the circumferences of an egg and embryo AP, we counted the numbers of small, electron-dense vesicles in the cortex. Within 10 µm of the plasma membrane, there was an average of 21 vesicles/100 μm^2 in the egg, compared to an average of 3.4 vesicles/100 μm^2 in the embryo, corresponding to an 84% drop (Figure 2.16). We can therefore conclude that we see an almost complete release of cortical vesicle content. Additionally, this analysis suggests

that other vesicular metals beside zinc and manganese are released from the zygote following fertilization. Finally, we sought to determine the biological relevance of this metal release.

Figure 2.16: TEM images of cortical vesicle loss

a

	Distance From Egg Membrane			
	0 – 2 µm	2 – 5 µm	5 – 10 µm	0 – 10 µm
Vesicles Counted	965	354	427	1746
Vesicles per 100 µm²	58	14	10	21
	Distance From Embryo Membrane			
Vesicles Counted	34	69	127	230
Vesicles per 100 µm²	2.5	3.4	3.8	3.4
	Vesicle Density Percent Difference Following Fertilization			
Percent Change	-96	-76	-64	-84

b

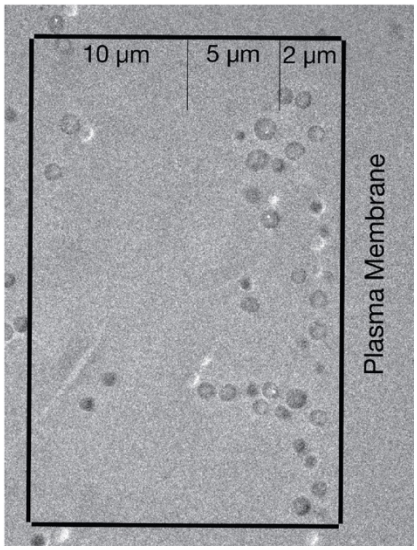

Figure 2.16: TEM data of eggs and embryos demonstrate that the majority of electron-dense vesicles disappear following fertilization. **a.** Table showing the differences in small, electron-dense vesicle content between the cortices of animal pole eggs and embryos. 8,263 µm^2 and 6,767 µm^2 of the egg and embryo cortices, respectively, were analyzed. **b.** Representative image showing the methodology of counting. TEM image of a ~150 nm thick slice of the animal pole egg. 47 images of the egg cortex and 47 images of the embryo cortex were analyzed.

Treatment with Zn or Mn decreases the fertilization rate

To determine if the zinc and/or manganese released from *Xenopus* eggs following fertilization prevents polyspermy, we fertilized eggs in buffer containing different concentrations of the two metals. Increasing concentrations of both zinc and manganese (Figure 2.17, Table 2.4; see Figures A.1 and A.2 for raw data) lead to decreasing rates of fertilization. This was determined by the percent of eggs that become properly-cleaving embryos (after normalization to a control fertilization), divided by the total count of eggs, embryos, and failed cleavage (Figure 2.17A). Zinc

inhibits fertilization at an order of magnitude lower concentration than that of manganese: a 50% block to fertilization occurs at 53 µM (95% CI = 47 - 61 µM) in $ZnSO_4$ treatments (Figure 2.17B), while it occurs at 890 µM (95% CI = 770 µM – 1.0 mM) in the case of $MnCl_2$ (Figure 2.17C).

Figure 2.17: Extracellular zinc or manganese inhibits fertilization in a dose-dependent manner

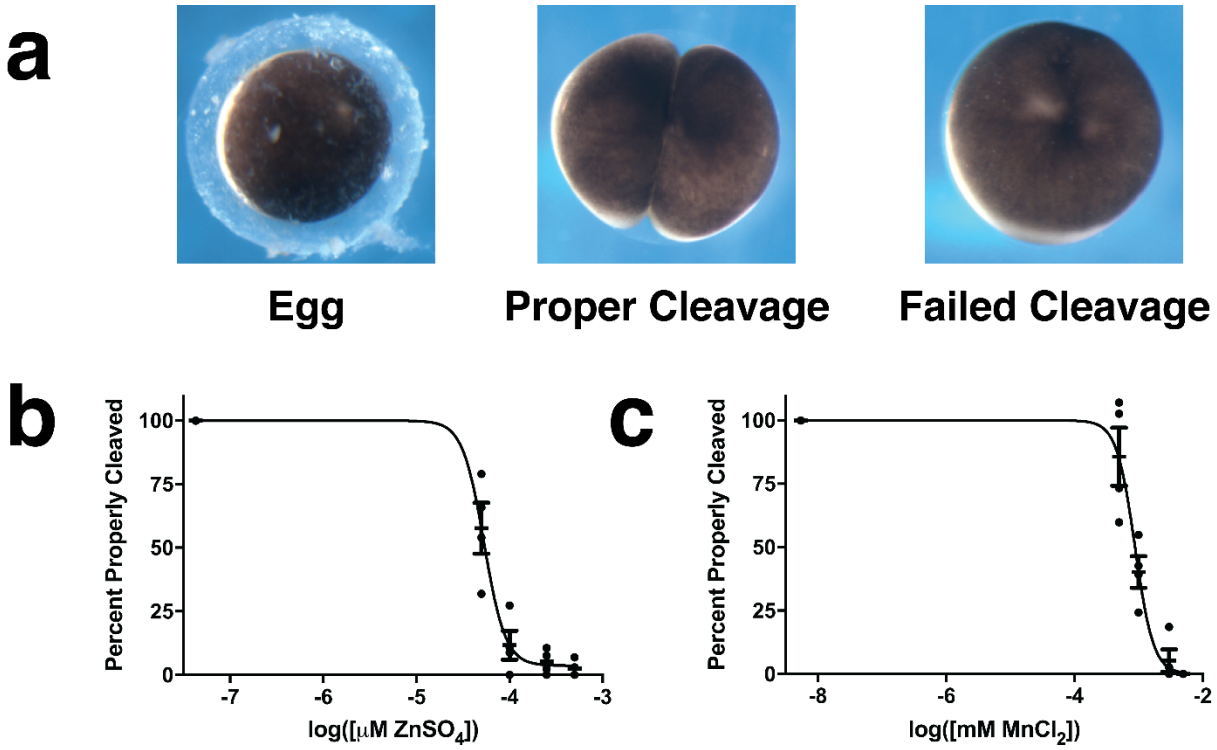

Figure 2.17: Both extracellular zinc and manganese block fertilization. **a.** Images of an unfertilized *Xenopus* egg (in jelly coat), a properly dividing embryo (first cleavage), and an instance of failed cleavage (meiotic catastrophe). **b.** An IC_{50} graph of the effects of extracellular $ZnSO_4$ on the rate of fertilization. IC_{50} = 53 µM (95% CI = 47 - 61 µM, R^2 = 0.94). Data are presented as mean percentage of eggs properly fertilized ± SEM, n = 4 frogs (39 – 102 eggs per datapoint). See Figure A.1 for raw data. **c.** An IC_{50} graph of the effects of extracellular $MnCl_2$ on the rate of fertilization. IC_{50} = 890 µM (95% CI = 770 µM – 1.0 mM, R^2 = 0.93). Data are presented as mean percentage of eggs properly fertilized ± SEM, n = 4 frogs (36 – 100 eggs per datapoint). See Figure A.2 for raw data.

Table 2.4: Fertilization rates in different concentrations of extracellular Zn^{2+} and Mn^{2+}

a

$ZnSO_4$ Concentration	% Properly Cleaved
50 µM	58 ± 10
100 µM	12 ± 5.7
250 µM	5.1 ± 2.4
500 µM	2.5 ± 1.6

n = 4

b

$MnCl_2$ Concentration	% Properly Cleaved
0.5 mM	86 ± 11
1 mM	40 ± 6.3
3 mM	5.3 ± 4.5
5 mM	0

n = 4

Table 2.4: a. The percent of *Xenopus* embryos that properly cleaved in buffer containing $ZnSO_4$. The percentages were normalized to control fertilizations. n = 4 frogs (39 – 102 eggs per datapoint). **b.** The percent of *Xenopus* embryos that properly cleaved in buffer containing $MnCl_2$. The percentages were normalized to control fertilizations. n = 4 frogs (36 – 100 eggs per datapoint). For both **a.** and **b.** data are presented as mean ± SEM.

Discussion

The goal of this study was to determine whether zinc is aggregated in a system of vesicles near the surface of *Xenopus* eggs and then released in a highly coordinated manner, similar to what has been shown for mammalian model organisms and human eggs. Indeed, we show that *Xenopus* eggs, like mammalian ones, undergo zinc-chelator induced activation, contain a similar system of zinc-loaded vesicles, albeit larger than those seen in mammalian eggs (6), as well as demonstrate a significant efflux of zinc following activation and fertilization. Thus, these reorganizations of zinc are essential to successful development in mouse and *Xenopus*. We demonstrate that one

function of the zinc released acts as part of a block to fertilization in *Xenopus*: the entry of a second sperm is typically catastrophic in early embryonic development. Further experiments are necessary to determine if, as in mouse eggs, zinc alters the structure of the outer envelope in *Xenopus* eggs. It is possible that release into the jelly coat could have an effect as well.

Surprisingly, we find that manganese is released alongside zinc in *Xenopus* eggs. Manganese, as well as a series of non-essential transition metal ions, is stored in vesicular compartments. Several lines of reasoning support the conclusion that the cohort of small metal-containing vesicles describe here are CGs. First, the timing of the zinc spark in *Xenopus* eggs correlates directly to the well-established process of CG breakdown. CG breakdown begins around 3 minutes post-fertilization (approximately the time needed for the sperm to penetrate the egg) and virtually all CGs have ruptured within 10 minutes. (109, 112) Second, the spatial distribution of CGs resembles that of the metal-containing compartments. CGs in the AP are mostly next to the plasma membrane, while those in the VP can be located farther into the cortex. (109) Third, the reported sizes of CGs – 1.5 – 2.5 μm (109, 113) – are similar to those of the metal-containing compartments. Although the vesicles described here appear smaller than the literature values, this is likely an effect of fixation and/or treatment with sodium sulfide. The zinc-containing CGs of mouse eggs are approximately 260 nm in diameter and have an intra-vesicular zinc content of 0.2 M. (6) *Xenopus* CGs are therefore larger but have lower zinc concentrations.

The role of cobalt and nickel loading in *Xenopus* CGs is currently unknown. Because of their toxicity, these metals may be sequestered in the egg CGs to minimize teratogenicity. It is also possible that the metals are not intentionally localized to CGs, but rather are mistaken for Zn^{2+} and Mn^{2+} by promiscuous divalent metal transporters. Sequestration and release of these metals may be specific to amphibians; we will further explore this in mouse.

These results in *Xenopus* provide evidence of the Mn^{2+} coordination environment in an egg. While the EPR and ENDOR signals drop as expected upon fertilization, the speciation of Mn remaining after Mn release at fertilization remains largely unchanged. Most importantly, both eggs and embryos have only a minimal population of Mn-Pi and polyP complexes (~10%), with most Mn carboxylate-bound (75-90%), and with negligible amounts bound in high molecular weight proteins/enzymes such as MnSOD. The coordinating carboxylates are presumed to be associated with low molecular weight metabolites. This type of insight into the manganese coordination environment in small subcellular compartments provides a starting point for understanding the chemistry of other metal ions in these highly specialized compartments.

Manganese content of eggs was not directly determined in our studies of mouse, worm, and cow as yields of eggs in these systems are too low to analyze with ICP-MS. Previously published single cell data on mouse eggs was acquired on XFM beamlines that did not provide sufficient incident flux for detection of manganese signals; however the single cell studies described here open the door to the evaluation of these questions. While the role of the manganese efflux is not known, one possible role may be as a block to polyspermy. In a mouse model, Mn^{2+} inhibited sperm-zona pellucida interactions, with 50% inhibition at 1.25 mM $MnCl_2$. (46) This is similar to what we found in our *Xenopus* model, in which half of fertilization was inhibited at 890 μM $MnCl_2$. Estimating the concentration of Mn released in the area around the *Xenopus* zygotes gives a value in the hundreds of micromolar range (see SI for calculations). Thus our results are consistent with a model in which the Mn and Zn release functions in part to block the entry of a second sperm, though additional tests of this mechanism are required.

In conclusion, we have found that a zinc exocytosis event upon fertilization is evolutionarily conserved between mammals and amphibians. Additionally, we have found that manganese is also released from *Xenopus* eggs and that both metals can inhibit fertilization.

Materials and Methods

Additional details including descriptions of methods and calculations are included in Supplemental Information.

Confocal Imaging. *Xenopus* eggs were obtained via established methods. Eggs were acquired from female *Xenopus laevis* (Nasco) between the ages of 3 to 10 years old. Confocal images were taken at 2.5X using a Leica SP5 microscope (Biological Imaging Facility, Northwestern University). Eggs were imaged in 0.1X Ca^{2+}, Mg^{2+}, and EDTA-free Marc's Modified Ringer's (MMR: 10 mM NaCl, 200 μM KCl, 500 μM HEPES pH 7.4) buffer containing 50 μM FluoZin-3 tetrapotassium salt (ThermoFisher Scientific)**.** In order to parthenogenically activate the eggs, ionomycin calcium salt from *Streptomyces conglobatus* (Sigma Aldrich) in DMSO was added to the buffer at a final concentration of 20 μM. To image fertilization, around half of a testis was ground in 200 μl 1X Ca^{2+}, Mg^{2+}, and EDTA-free MMR (100 mM NaCl, 2 mM KCl, 5 mM HEPES pH 7.4) and kept on ice. Before imaging, the sperm solution was mixed 1:1 with 0.1X Ca^{2+}, Mg^{2+}, and EDTA-free MMR and added at a 1:10 dilution to the buffer in the imaging dish.

ICP-MS. The jelly coat of eggs and embryos was removed through soaking in a 3% w/v solution of cysteine-HCl, pH 8 for 10 minutes. They were rinsed and then 20 egg/embryos were placed in a metal-free conical tube. 3-5 tubes of eggs/embryos were analyzed for each of the 4 separate frogs. The eggs/embryos were dried in a heat block and dissolved in 450 μl 67-70% trace-metal free

nitric acid (Supelco) overnight at 70 C. The solution was diluted to 15 ml using MilliQ H_2O. Metal concentrations were measured using a Thermo iCAP Q ICP-MS and a Thermo iCAP 7600 ICP-OES (Quantitative Bio-element Imaging Center, Northwestern University). The elemental composition of frog tank water was measured using a Thermo iCAP Q ICP-MS and a Thermo Element2 High Resolution Magnetic Sector Field ICP-MS (Quantitative Bio-element Imaging Center, Northwestern University)

EPR/ENDOR/ESEEM Spectroscopy. Frog eggs and embryos were loaded into a quartz EPR sample tube, flash-frozen in liquid nitrogen, and stored at 77 K until analysis. 35 GHz continuous-wave (CW) EPR spectra were recorded using a lab-built 35 GHz EPR spectrometer. (114) Absorption-display EPR spectra were collected from eggs/embryos and Mn-metabolites by using CW "rapid passage" methods at 2 K as previously described. (101, 104) Pulsed ENDOR/ESEEM spectra were recorded using a lab-built 35 GHz pulsed EPR spectrometer. (115) All spectra were recorded at 2 K using an immersion helium cryostat. Experiments were performed on three sets of samples and the average ^{31}P%, ^{1}H% were used to calculate the fractional Mn^{2+} speciation. The fractional populations of Mn-L, L = H_2O, Pi, polyP, and ENDOR-silent complexes reported as percentages were obtained using a heuristic binding model as previously described. (102)

Sample Fixation and XFM. Eggs/embryos were fixed in a solution containing NaSH (2.5% glutaraldehyde, 2% paraformaldehyde, 20 mM NaSH, in 0.1 M PIPES buffer, pH 7.4) for 2 hours at RT. They were then dehydrated in EtOH. After dehydration, eggs/embryos were infiltrated with a Durcupan resin and polymerized at 65° C for 24 hours. Sections of 400 nm and 2 μm thickness were obtained with a Ultracut-S ultramicrotome (Leica) using a diamond knife (Diatome/EMS). Egg and embryo sections were mounted on 200 nm-thick silicon nitride windows (Norcada) and

were glued to aluminum sample holders using clear nail polish. The sections were imaged at Beamline 2-ID-D at the Advanced Photon Source at Argonne National Laboratory.

Analytical Electron Microscopy. Eggs and embryos used in AEM studies were fixed as above. ~ 150 nm thick ultramicrotome-cut sections were mounted on an aluminum grid coated with a Formvar and a carbon film and mounted in a custom-manufactured beryllium-tipped cryo-transfer tomography holder from Fischione Instruments. Experimental measurements were performed using ThermoFisher Talos F20 and the prototype ANL PicoProbe AEM's, both equipped with the most recent generations of high solid angle (~ 1sR) X-ray energy dispersive spectroscopy systems. All observations were made at 200 kV in both TEM and STEM modes at room temperature. Temporally resolved hyper spectral imaging (HSI) was used to scan variable area regions of interest at spatial resolutions ranging from 2-100 nm. Probe currents employed were typically ~ 100 pA, HSI regions of interest utilized pixel dwell times of ~ 25 μsec/pixel for hundreds of frames to develop statistics and mitigate drift, resulting in final data acquisition times of ~ 500 msec/pixel. Programs used for data acquisition and analysis were ThermoFisher Scientific TIA/ESVision and ThermoFisher Scientific Velox.

Fertilization Experiments. Eggs were placed in 0.1X EDTA-free MMR containing different concentrations of $ZnSO_4$ or $MnCl_2$ for 15 minutes. They were fertilized using a sperm solution containing the same metal concentration. 15 minutes after fertilization, the dishes were flooded with the corresponding metal solutions. After cleavage became apparent, eggs were scored between uncleaved, properly cleaved, and failed cleavage. The percent of eggs properly cleaved in the experimental groups was normalized to that of a control group fertilized in buffer that was not spiked with zinc or manganese.

Chapter 3: EMI2 Binds Zinc Over Five Orders of Magnitude

John F. Seeler, Andrew Crawford, Muhammed Qureshi, Stephen J. Allen, Graham George, Teresa K. Woodruff, Thomas V. O'Halloran

The following people acquired and analyzed data used in this chapter:

Figure 4.4: Graham George assisted with HERFD sample design and analysis. Muhammed Qureshi acquired the HERFD data. Andrew Crawford assisted with sample preparation and analyzed the data.

Abstract

Successful mitosis and meiosis require tight regulation. The anaphase promoting complex /cyclosome (APC/C) governs cell cycle progression and is regulated by the spindle checkpoint protein EMI2 during meiosis. In mammalian oocytes, zinc levels increase between prophase I and metaphase II and then decrease following fertilization. The spindle checkpoint protein EMI2 establishes and maintains metaphase II arrest. EMI2 has two zinc binding sites, one C_4 and one C_3H. According to the results of competitive chelation experiments, the stronger site binds zinc 420,000X more tightly than the weaker. High-energy-resolution fluorescence detection X-ray absorption spectroscopy analysis of EMI2 show that the C_4 site has the tighter binding affinity. Because zinc fluxes correlate with APC/C inhibition, we believe that at least one zinc-binding site in EMI2 is regulatory and that zinc therefore acts as a signaling agent in meiosis. Although transition metals have traditionally been viewed as only protein cofactors, this work contributes to the growing understanding that they can possess signaling functions as well.

Introduction

Mitosis and meiosis occur in every sexually-reproducing species and require the precisely timed activity of regulatory proteins at each stage. (116) The anaphase promoting complex/cyclosome (APC/C) is a ubiquitin ligase that governs cell cycle progression. The APC/C attaches polyubiquitin chains to substrate proteins, which are subsequently degraded by the 26S proteasome. (47) The evolutionarily-conserved vertebrate spindle checkpoint proteins EMI1 (early mitotic inhibitor 1, a.k.a. F-box protein 5 [FBXO5]) and EMI2 (a.k.a. Emi1-related protein 1 [Erp1] and F-box protein 43 [FBXO43]) are involved in inhibiting the APC/C in mitosis and meiosis, respectively. (48-50) EMI2 begins to be expressed after metaphase I and is at its maximum expression at metaphase II when it fully inhibits the APC. (63) The APC remains inhibited until fertilization, when EMI2 is degraded and the zygote proceeds into anaphase II (AII). (29) EMI2 is required for proper meiotic progression in both oocytes and sperm. (70)

Zinc fluxes regulate meiotic progression during oocyte maturation in mammals. As murine oocytes undergo meiotic maturation, their zinc content increases by 50% within 12 hours between the germinal vesicle (GV) stage and metaphase II arrest. (4, 5) Upon fertilization or chemical activation there is an efflux of zinc, dubbed “zinc sparks”. About 20% of the zinc leaves within 6 hours post fertilization. (6) Zinc sparks occur in multiple mammalian species (6, 7, 15) as well as different classes of vertebrates. (17, 18) (Seeler *et al.*, accepted) Proper embryonic development is then dependent on adequate levels of zinc. (13)

Perturbing these natural changes in zinc concentration leads to meiotic catastrophe. Decreasing the amount of available zinc, either through treatment with the zinc chelator N,N,N’,N’-Tetrakis(2-pyridylmethyl)ethylenediamine (TPEN) (5, 8, 29) or through disrupting the

zinc transporters ZIP6 and ZIP10 with morpholinos or antibodies (11), leads to meiotic catastrophe. Likewise, unnaturally high zinc levels can also disrupt meiosis. Zinc pyrithione, a zinc ionophore, inhibits the meiotic progression of activated eggs; oocytes retain a metaphase-like spindle (so-called "metaphase III") rather than proceeding to interphase. (7)

EMI2's zinc-binding region (ZBR) is an in-between-ring (IBR) domain located near the C-terminus. It possesses two tetrahedral metal binding sites, each containing two pairs of amino acid ligands (C_4 and C_3H). EMI2 requires a functional ZBR to be able to inhibit the APC/C. Mutating the ZBR leads to meiotic catastrophe: mutating the first cysteine in both *Xenopus laevis* and murine EMI2 (C583A/C573A) causes significant problems. (5, 29, 71) Additionally, mutating C591A (the third cysteine in the first site) or C601A (the first cysteine in the second site) affect murine EMI2's ability to maintain metaphase II arrest. (29) Premature expression of EMI2 affects meiotic progression; injecting EMI2 into GV oocytes arrests them at metaphase I. The addition of TPEN to the medium prevents the precocious arrest, further demonstrating that EMI2 requires zinc to function. (5)

Because there is a significant flux in intracellular zinc levels in mammalian meiosis and because EMI2 requires an intact ZBR in order to function, we hypothesize that zinc acts a signaling agent to establish as well as end meiotic arrest. The purpose of these experiments was twofold: First, what are the affinities of EMI2's zinc-binding sites? Second, structurally which site (C_4 or C_3H) possesses the higher zinc-binding affinity? As demonstrated below, one of EMI2's zinc-binding sites possesses a zinc-binding affinity 420,000X stronger than that of the other. Therefore, we predict that as intracellular zinc content increases between GV and metaphase II, the regulatory site is filled. EMI2's structure changes, allowing it to inhibit the APC. Following fertilization, zinc

leaves the regulatory site, EMI2's structure returns to its half-filled form, it no longer binds the APC, and the zygote enters into AII.

Methodological Improvements

When I inherited this project, improvements were necessary for both the purification of $EMI2^{ZRL}$ and the competitive chelation experiments. The following is a description of the changes I made and their rationale.

$EMI2^{ZRL}$ Purification Process Improvements

When I took over the project and attempted to conduct titration experiments with frozen aliquots of protein, the titrations failed because the protein was oxidized or otherwise degraded. In addition, the yield of the month-long expression and purification protocol was low. I therefore proceeded to improve the process and made the following changes (see the Methods section for the complete, final protocol – note that not every step was modified):

Increased Concentration of Reducing Agent: The original protocol used 1 mM 1,4-dithiothreitol (DTT), a reducing agent. However, this is 1/5 of the recommended amount to use, which is probably why the EMI2 was oxidized after a month-long purification process. I switched to 5 mM DTT and then finally to 1 mM Tris(2-carboxyethyl)phosphine hydrochloride (TCEP). TCEP is superior to DTT because of its longer lifespan. (117)

Increased Growth Volume: The original protocol called for 4 L of media to be grown. However, because of the low yield of the protocol and extra space in the shakers, I increased the volume to 10 L.

Larger Anion Exchange Column: The original protocol used a GE Healthcare 5 ml HiTrap Q column. I switched to a 20 ml HiPrep Q column, which contains the same resin. The 5 ml column was being overloaded, especially when I increased the amount of protein by 2.5X.

MBP Cleavage: Because the EMI2^{ZRL} protein is expressed with an MBP tag which is 5X the size of the construct, the tag needs to be cleaved by the Factor Xa protease. The original protocol called for using Factor Xa at a 1:100 ml: ml ratio. This does not make sense, because although the Factor Xa comes from the manufacturer at a specific concentration, the protein is not eluted from the anion exchange column at the same concentration in every experiment. Therefore, the tag needs to be cleaved at a standard mg: mg ratio. I tried different ratios of protease to MBP-EMI2^{ZRL}, but only got good cleavage at 1:25 or 1:50, which uses a prohibitively expensive amount of protease. I therefore optimized the buffer conditions. After testing multiple buffers, 20 ml HEPES, 100 mM NaCl, pH 7.4, with 10 mM β-mercaptoethanol provided the most efficient cleavage. I proceeded with a 1:200 Factor Xa: MBP-EMI2^{ZRL} ratio.

Cation Exchange Column: After cleavage, the cleaved EMI2^{ZRL} needs to be separated from the MBP tag and Factor Xa by a cation exchange column. The original protocol used a GE Healthcare 5 ml HiTrap SP FF column and called for the column to be loaded and run manually – i.e. through slowly pressing a syringe full of protein and elution buffer over a handheld column. This did not lead to good protein separation – although some of the cleaved MBP and/or Factor Xa were removed, the elute consisted of a mixture of cleaved EMI2^{ZRL}, cleaved MBP, Factor Xa, and an off-target cleavage product. I changed the protocol so that the column was run over a salt gradient using the FPLC, which separated the enzyme and the different cleavage products. Additionally, I switched to a GE Healthcare 5 ml HiTrap SP HP column, which provides better resolution than the FF (Fast Flow) column.

Gel Filtration Column: Because the cation exchange column in the original protocol did not separate the cleaved $EMI2^{ZRL}$ from the other proteins, it called for a gel filtration column to separate them. Since I obtained a pure $EMI2^{ZRL}$ peak once I used a buffer gradient for the cation exchange column, I eliminated the need for the gel filtration, saving time and a significant amount of protein.

Final Buffer Exchange: In the original protocol, $EMI2^{ZRL}$ was demetallated using a dialyzer cassette and three rounds of EDTA-containing buffer, followed by exchange into one round of the final titration buffer. After this, the protein was run over a GE Healthcare PD 10 desalting column. This led to significant protein loss through dilution as well as some zinc contamination of the demetallated protein, as the column cannot be pre-cleaned with nitric acid to remove any endogenous metal. I altered this step in order to eliminate the PD 10, instead keeping the protein in the dialysis cassette and exchanging into a total of three rounds of titration buffer.

Titration Experiment Improvements

Upon inheriting this project, the competitive chelation experiments provided zinc-binding K_{D}s of $EMI2^{ZRL}$ over two orders of magnitude. Additionally, the titration experiment for determining the affinity of the weak-binding site was set up inversely, possibly leading to inaccurate results. Therefore, the following changes were made to the titration experiments:

Automation of Titration Process: Originally, the titrations were performed using a Hamilton syringe fitted with a repeater. After titrating zinc, the solution in the cuvette was mixed with a pipet, allowed to sit to equilibrate, and then the fluorescence was measured. There were several problems with this procedure. First, titration by hand is not very accurate, leading to irregular fluorescence curves and therefore poor data fitting. Second, the total liquid volume in the cuvette is 1 ml. Inserting a syringe and then mixing with a pipettor after each step leads to sample

loss, which noticeably affects the final volume and therefore the calculations. Third, constant mixing is better for reaching chemical equilibrium than pipetting several times. Fourth, the titrations were performed at room temperature, while they should have been performed at a set, steady temperature. To solve these problems, I purchased a stirring/water bath accessory for the fluorimeter as well as a syringe pump. The accessory turns a tiny stir bar at the bottom of the quartz cuvette and is connected to a water bath by hoses in order to maintain a constant temperature. The syringe pump accurately titrates small volumes of liquid and can be automated, leading to more accurate and precise titrations.

Changes to Fitting Process: The initial experiments contained about six titration points which, when analyzed, did not lead to reproducible K_D values. After discussions with Professor Christoph Fahrni (Georgia Institute of Technology), the procedure was changed so that there were 20 titration points in order to obtain a good fit. Additionally, I only analyzed titration data between 10 – 90% zinc occupancy, which contains the greatest part of the slope of the binding isotherm. (118)

Redesign of Weak-Binding Site Titration: The standard protocol for a competitive chelation experiment is to have the protein and chelator in a cuvette, and then titrate in metal and measure the increase in fluorescence. (119) Originally, the titration for the weak binding site was set up inversely: EMI2 (one zinc loaded – OZL) was titrated into a cuvette containing zinc and FluoZin-3 (FZ3), a zinc binding dye. As zinc entered the EMI2 weak binding site, the fluorescence of the FZ3 is quenched. The problem with this setup is that if EMI2's zinc-binding affinity is much greater than that of FZ3, there is little competition and the fluorescence should be quenched virtually linearly, preventing a good fit of the titration data. I therefore set this experiment up according to the standard protocol in which zinc is titrated into the cuvette at a 1:1 EMI2 (OZL):

FZ3 ratio. The fluorescence was quenched until almost all of the EMI2 (OZL) was bound to zinc, meaning that the EMI2 has a significantly higher zinc-binding affinity than FZ3. I then tried a 1:10 EMI2 (OZL): FZ3 ratio which provided good competition, proving that the original inverse protocol was not giving a good fit.

Results

EMI2's binding sites have significantly different zinc-binding affinities. Full length EMI2 is insoluble at the concentrations necessary for biochemical experiments. Because of this, we designed a truncated construct, dubbed EMI2^{ZRL}, of murine EMI2 containing amino acids 566-641. This contains part of the linker, the IBR domain, and continues to the C-terminus (Figure 3.1). Truncated peptides containing a zinc finger can be used to accurately determine binding affinity of the whole protein because their structure is mainly influenced by zinc binding. (120)

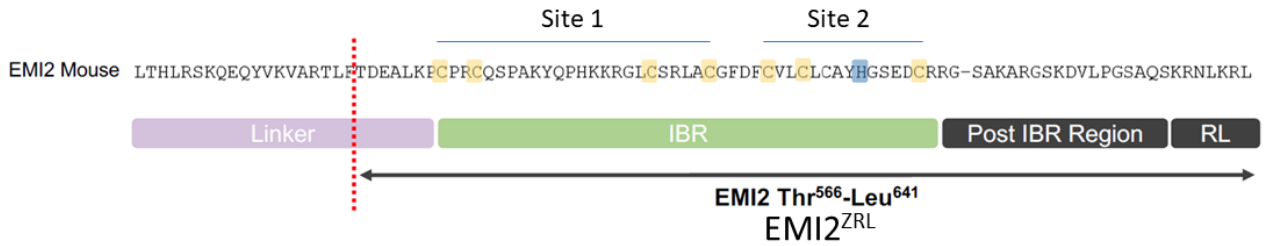

Figure 3.1: Sequence of the EMI2^{ZRL} construct.

In order to determine the zinc-binding affinities of the two zinc-binding sites, we performed fluorescent competitive chelation experiments. Titrations were performed with a syringe pump, which titrated with 99% accuracy (Table 3.1). Additionally, this was confirmed through measuring the amount of zinc in the cuvette post-titration through inductively coupled plasma mass

spectrometry (ICP-MS). The theoretical amount of zinc in the cuvette was the same as measured by ICP-MS (Table 3.2).

	Volume of Water in Cuvette (µl)	% Difference from Theoretical Volume
Experiment 1	51.67	98.4
Experiment 2	51.94	98.9
Experiment 3	51.97	99.0
Experiment 4	52.14	99.3
Experiment 5	52.13	99.3
Mean ± SD	52	99 ± 0.43 %

Table 3.1: Accuracy determination of the syringe pump. 2.5 µl was titrated 21 times for a final theoretical volume of 52.5 µl. The cuvette was weighed before and after titration to obtain the mass of water in the cuvette. The syringe pump titrates with 99% accuracy.

	Post-Titration [Zinc] (in mM)
Theoretical Amount of Zinc in Cuvette	1.0 ± 0.0078
Experiment 1 ICP-MS Value	1.0 ± 0.0064
Experiment 2 ICP-MS Value	1.0 ± 0.015
Experiment 3 ICP-MS Value	1.0 ± 0.013

Table 3.2: The final amount of zinc measured in the cuvette by ICP-MS for three representative TPEN titrations compared to theoretical amount of zinc. The experimental zinc concentrations agree with the theoretical.

To determine the affinity of the tighter-binding site, we followed an established procedure which provides a very close approximation. (121) Demetallated EMI2^{ZRL} competed for zinc against TPEN ($K_D = 2.6 \times 10^{-16}$ M), which was at a 50-fold molar excess. Zinc was titrated into a fluorescence cuvette. Because TPEN possesses no intrinsic fluorescence, the fluorescence of the protein's tyrosine residues was measured. As EMI2^{ZRL} binds zinc, its average structure changes, leading to an increase in fluorescence emission. The zinc-binding affinity of the strong site was determined to be 1.3 ± 0.10 x 10^{-15} M (mean ± SD, n = 3) (Figure 3.2).

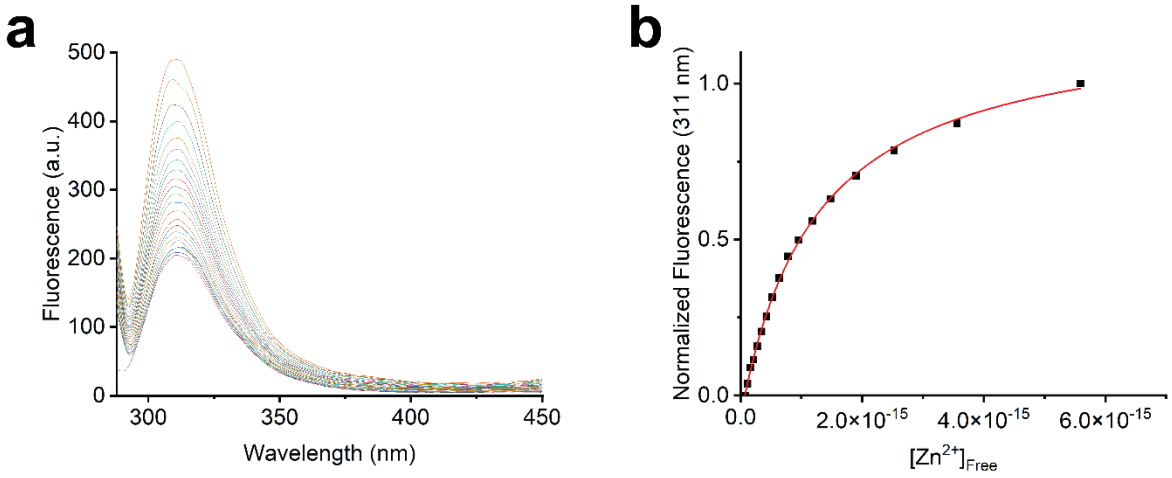

Figure 3.2: Representative strong-binding site titration (R^2 = 0.99906). Data were fit to Equation 1 (see Materials and Methods). The affinity of the strong-binding site is 1.3 ± 0.10 x 10^{-15} M (mean ± SD, n = 3). [EMI2^{ZRL}] = 20 µM, [TPEN] = 1 mM. $ZnSO_4$ titrations: [$ZnSO_4$] = 20 mM, 2.5 µL per titration. Excitation wavelength: 278 nm. Emission wavelength: 311 nm. **a.** Change in fluorescence from 0 – 105% zinc occupancy of the strong binding site (0 – 52.5% zinc occupancy of EMI2^{ZRL}). **b.** Fitted data from 10 – 90% zinc occupancy.

Competition with TPEN demonstrated that one binding site has a much higher affinity than the other. In order to determine the affinity of the weak binding site, we filled the strong binding site with one molar equivalent of zinc before performing competitive chelation experiments. Through testing zinc chelators with varying affinities, we found that a ratio of 1 mole EMI2^{ZRL} (one zinc-loaded) to 10 moles of FZ3 achieved good competition. FluoZin-3 (K_D = 9.1 × 10^{-9} M) (95) is a zinc-binding dye, so its fluorescence changes were measured following each titration. The zinc-binding affinity of the weak site was determined to be 5.4 ± 0.47 x 10^{-10} M (mean ± SD, n = 3) (Figure 3.3). There is therefore a ~420,000-fold difference between the affinities of the two binding sites.

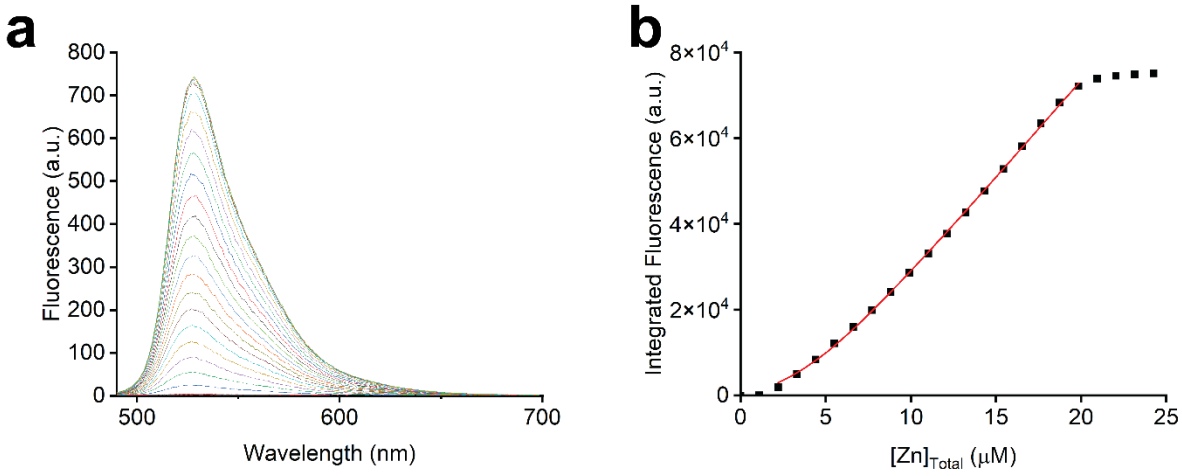

Figure 3.3: Representative weak-binding site titration (K_D = 5.9 x 10^{-10} M, 95% CI: 4.1 – 8.0 x 10^{-10} M. Data were analyzed with Dynafit (see Materials and Methods). The affinity of the weak-binding site is 5.4 ± 0.47 x 10^{-10} M (mean ± SD, n = 3). [$EMI2^{ZRL}$ (one zinc-loaded)] = 2 μM, [FluoZin-3] = 20 μM. $ZnSO_4$ titrations: [$ZnSO_4$] = 440 μM, 2.5 μL per titration. Excitation wavelength: 425 nm. Fluorescence integrated over 490 - 650 nm. **a.** Change in fluorescence from 0 – 115% zinc occupancy of the weak binding site (50 – 107.5% zinc occupancy of $EMI2^{ZRL}$). **b.** Data fitted from 10 – 90% zinc occupancy.

The C_4 binding site has higher zinc-binding affinity than the C_3H. Competitive chelation experiments provide information on the binding affinities of metal-binding sites, but if a protein contains multiple binding sites the experiments cannot tell which affinity corresponds to which site. Many studies of zinc coordination environments use the X-ray absorption fine structure (EXAFS) and X-ray absorption near-edge structure (XANES) regions of the X-ray absorption spectroscopy (XAS) spectrum. Unfortunately, spectral changes as a function of atomic number change almost indiscernibly and similar to X-ray diffraction, XAS methods, at least in the classical sense, cannot distinguish similar scatterers. For Zn, this tends to be the case, and both nitrogen and sulfur ligands can appear ambiguous in XAS spectra.

However, recent advancements in XAS have made possible the differentiation of these two ligands through the use of high-energy-resolution fluorescence detection (HERFD) spectroscopy,

which we have applied to the study of EMI2 to identify whether the C_4 or the C_3H site constitutes the strong binding site. HERFD narrows the energy bandwidth of the X-ray fluorescence, providing higher resolution information and therefore permitting accurate identification of the metal coordination environment. (122, 123)

Two samples of $EMI2^{ZRL}$ were compared. One was loaded with 0.95 molar equivalents of zinc while the other was loaded with 2.05. Because of the great difference in binding affinities of the two sites, virtually all of the zinc in the former sample should be located in the strong-binding site. The samples were analyzed at the Stanford Synchrotron Radiation Lightsource (SSRL) at the SLAC national accelerator laboratory. The experimental spectra were compared to HERFD spectra of zinc in C_4, C_3H, and C_2H_2 coordination environments (24), strongly suggesting that EMI2's strong-binding and weak-binding sites are C_4 and C_3H, respectively (Figure 3.4).

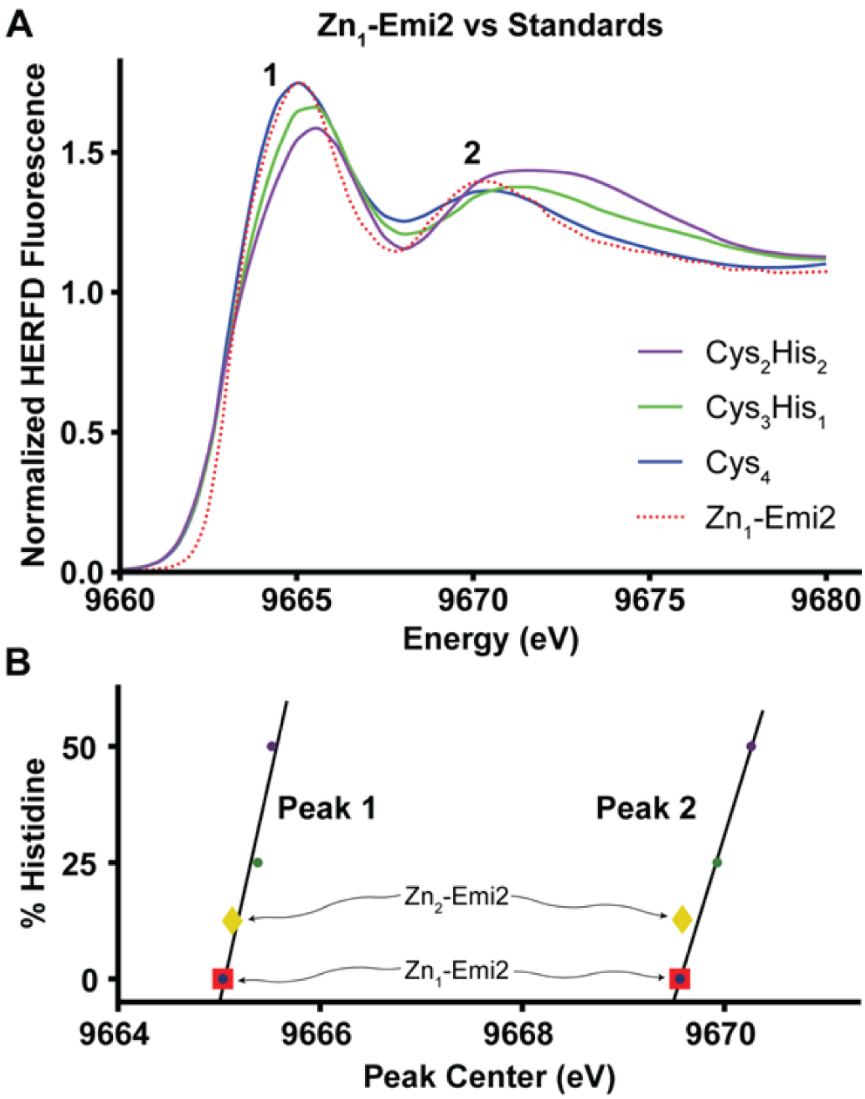

Figure 3.4: Determination of Zn and EMI2 stoichiometry via HERFD. **a.** Zn HERFD spectra collected at SSRL beam line 15-2 using a single Zn crystal analyzer for Zn_1-Emi2 and Zn_2-EMI2. The spectrum for Zn_1EMI2 is overlaid by the spectra for Zn-Cys_4, Zn-Cys_3His_1, and Zn-Cys_2His_2 peptides from Thomas et al. (124) **b.** The overlaid points of Zn_1- and Zn_2-bound EMI2 suggest the Zn^{2+} in the tight binding (structural) site is bound by 4 cysteines and the Zn in the weak binding (regulatory) site is bound by 3 cysteines and 1 histidine. Linear regression of the Thomas peptide standards resulted in r^2 of 0.9425 and 0.9993 for peaks 1 and 2, respectively.

Discussion

According to our competitive chelation results, there is an approximately 420,000-fold difference in the zinc-binding affinities of EMI2's two binding sites. This is a very large difference

for RING proteins. Although RING proteins' metal-binding affinities have not been studied in depth, the literature differences in affinity are within two orders of magnitude. (58, 125, 126) We therefore believe that EMI2's zinc binding has a regulatory role, with the strong-binding site having a structural role and the weak-binding site having a regulatory role, filling as intracellular zinc levels rise and losing its bound zinc following fertilization. Because free zinc levels in a mammalian cell are usually on the pico-molar scale (11, 23), it is plausible that cytoplasmic zinc levels increase between G_2/PI and decrease following the zinc efflux, as a 50% increase in intracellular zinc would significantly affect the oocyte's zinc buffering capacity. *In vitro* experiments reconstructing the minimal functional unit of the APC/C as well as *in vivo* experiments will provide support for the hypothesis that EMI2's function is regulated by zinc occupancy.

According to the HERFD data, the C_4 site possesses a stronger binding affinity than the C_3H site. Because the affinity of a zinc-binding site is affected by pH and the surrounding amino acid environment (120, 127, 128), a C_4 site is not expected to necessarily have a stronger affinity than a C_3H. (128) The identification of the strong-binding site will allow further experiments to focus on how zinc binding to the C_3H site changes EMI2 structure and therefore affects EMI2 and therefore APC/C regulation.

EMI2 is conserved in vertebrates and it is currently unknown how broadly zinc regulation of meiosis is conserved in classes other than Mammalia, though in *Xenopus* proper zinc levels are necessary for prophase I (26-28) and AII (Figure 2.3) entry. To determine if zinc regulation of EMI2 is evolutionarily conserved, recombinant EMI2 from different vertebrate species should be purified and analyzed.

Signaling and regulatory ions are generally considered to be alkali and alkaline metals, with transition metal ions serving as protein cofactors. However, emerging evidence demonstrates that Zn^{2+} has a signal transduction role in both the brain (129) and pancreas. (3) If our planned experiments demonstrate that Zn^{2+} regulates meiotic progress through differential binding to EMI2, this will contribute to the emerging picture that transition metal ions can act as signaling agents, rather than just as protein cofactors.

Materials and Methods

Protein expression. To produce $EMI2^{ZRL}$, the following insert was cloned into a pMALc5x plasmid (New England Biolabs N8108S), which produces maltose-binding protein fusions:

```
actgatgaagctttaaagccttgcccgaggtgccaatcccctgctaagtaccagccgcacaaga
aaaggggctatgcagccgcctggcctgcggctttgacttctgtgtgttatgtctgtgcgctta
tcacgggtctgaagactgtagaagagggtcagcaaaggcgagaggtagcaaagatgttctccca
gggagtgcccaaagcaagcggaacttaaaacgcctctga
```

The plasmid was transformed into NEB Express *E. coli* (#C2523I). Bacteria were grown overnight at 37 C and transferred at a 1:100 dilution into Luria-Bertani broth containing 2 g/L glucose, 100 μg/L ampicillin, and 100 μg/L $ZnSO_4$. The bacteria were grown at 37 C until they reached logarithmic growth phase (OD 0.6-0.8). They were induced with IPTG (330 μM/L) and harvested after 4 hours.

Protein purification. All purification was performed at 4 C. The bacteria were resuspended in column buffer (20 mM HEPES, 200 mM NaCl, pH 7.4, containing 1 mM TCEP) and then homogenized using an Avestin Emulsiflex C5 (Recombinant Protein Production Core, Northwestern University). The lysate was loaded onto an amylose column (NEB #E8021L)

equilibrated in column buffer. The column was washed with 3 column volumes of buffer and then the protein was eluted with 3 column volumes of buffer containing 10 mM maltose.

The protein was then concentrated and exchanged into 20 mM HEPES, pH 7.4 containing 1 mM TCEP. The protein was loaded onto a HiPrep Q HP 16/10 column (GE #29018182) pre-equilibrated in the same buffer. The run was over a 0-300 mM NaCl gradient with a total elution volume of 600 ml.

Fractions containing pure protein were concentrated and exchanged into 20 mM HEPES, 100 mM NaCl, pH 7.4, containing 10 mM β-mercaptoethanol. Factor Xa (NEB #P8010L) was added at a ratio of 1 mg Factor Xa: 200 mg MBP-EMI2^{ZRL}. The cleavage proceeded for 24 hours at 4 C.

To separate EMI2^{ZRL} from cleaved MBP, Factor Xa, and off-target cleavage products, the sample was loaded onto a HiTrap SP HP column (GE #17115201) pre-equilibrated in 20 mM HEPES, 100 mM NaCl, pH 7.4, containing 1 mM TCEP. The run was over a 100-500 mM NaCl gradient with a total elution volume of 100 ml. Fractions containing pure EMI2^{ZRL} were concentrated using a centrifugal concentrator with a 3 kDa MWCO.

To demetallate the protein, it was loaded into a dialyzer cassette with a 3,500 kDa MWCO (ThermoFisher #66110). The cassette was placed in 500 ml of demetallation buffer (20 mM HEPES, 50 mM EDTA, 100 mM NaCl, pH 7.4 containing 1 mM TCEP) and stirred for at least 3 hours. The buffer was replaced twice for a total of 3 rounds of exchange. Titration buffer (50 mM HEPES, 100 mM NaCl, pH 7.4 containing 1 mM TCEP) was treated with 10 g Chelex 100 Molecular Biology Grade Resin (Biorad #1421253) per liter of buffer for at least 2 hours prior to use. To prepare the protein for titration, the cassette was placed in 500 ml of titration buffer and stirred for at least 3 hours. The buffer was replaced twice for a total of 3 rounds of exchange.

The protein was removed from the cassette and placed in a metal-free conical tube (VWR #89049-170). Protein concentration was determined by BCA assay (ThermoFisher #23252). To determine the amount of residual metal contamination, the protein was analyzed using a Thermo iCAP Q Inductively Coupled Plasma Mass Spectrometer (Quantitative Bio-element Imaging Center, Northwestern University).

Strong binding site competitive chelation experiments. A 20 mM stock solution of N,N,N',N'-Tetrakis(2-pyridylmethyl)ethylenediamine (TPEN - Sigma #P4413) in DMSO was created. Demetallated EMI2^{ZRL} and TPEN were added to Chelex-treated titration buffer in a quartz cuvette (Hellma #119004F-10-40) at final concentrations of 20 μM and 1 mM, respectively, in a total volume of 1 ml. The cuvette was stirred for 10 minutes in a PerkinElmer LS-55 Fluorescence Spectrometer at RT. The cuvette was excited at 278 nm and emission was measured at 311 nm. Using a syringe pump (JKEM Scientific #SYR-1200-PC), 21 titrations of 2.5 μl 20 mM $ZnSO_4$ were performed to achieve a final zinc occupancy of 52.5% (i.e. 105% of the strong-binding site). The solution was found to equilibrate after 10 minutes (Figure 3.5), so the solution in the cuvette was stirred for 10 minutes in the fluorimeter before each titration.

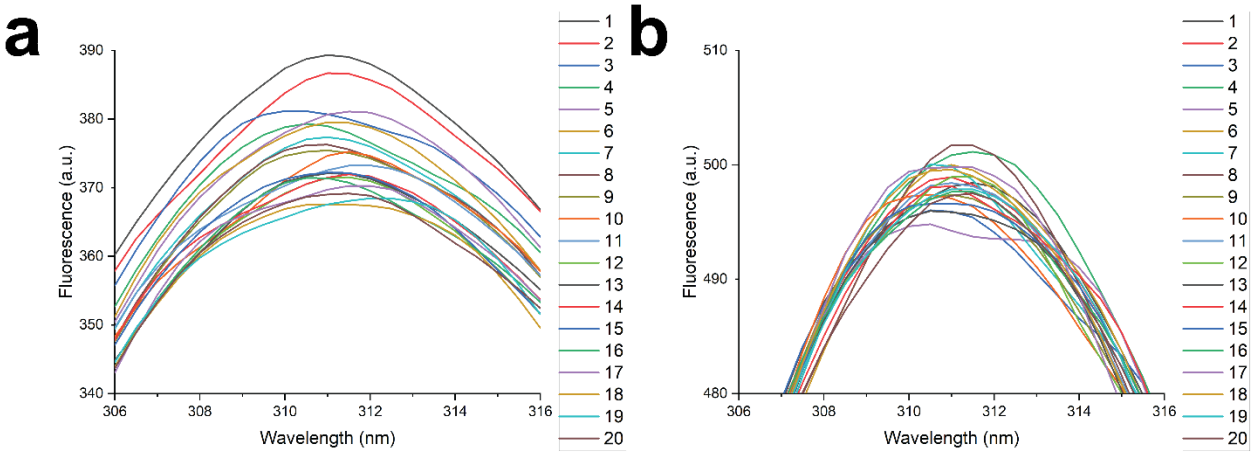

Minutes Post-Titration	Fluorescence (311 nm)	Percent Change
1	389.3418	
2	386.7042	0.68
3	380.7087	1.6
4	378.9594	0.46
5	380.6731	0.45
6	379.5278	0.30
7	377.3455	0.58
8	376.2695	0.29
9	375.4323	0.22
10	374.6629	0.21
11	372.5478	0.57
12	371.4348	0.30
13	372.1053	0.18
14	371.4651	0.17
15	372.2163	0.20
16	371.3969	0.22
17	369.7181	0.45
18	367.5055	0.60
19	367.5565	0.014
20	369.0117	0.39

Minutes Post-Titration	Fluorescence (311 nm)	Percent Change
1	498.1027	
2	498.9115	0.16
3	495.9203	0.60
4	500.857	1.0
5	494.235	1.3
6	499.9979	1.2
7	499.861	0.027
8	501.7382	0.38
9	497.3968	0.87
10	497.0755	0.065
11	498.4111	0.27
12	498.9418	0.11
13	495.8537	0.62
14	498.1356	0.46
15	496.6133	0.31
16	497.6438	0.21
17	499.7905	0.43
18	499.6047	0.037
19	497.8716	0.35
20	497.2975	0.12

Figure 3.5: Kinetics of TPEN competition demonstrating that equilibrium is reached within 10 minutes post-titration. **a.** Graph of fluorescence at 50% zinc occupancy. Each line represents one minute after zinc addition. **b.** Graph of fluorescence at 90% zinc occupancy. Each line represents one minute after zinc addition.

Data between 10-90% zinc occupancy were analyzed, which contains the greatest part of the slope of the binding isotherm. (118) Data were normalized so that the fluorescence at 10% zinc occupancy = 0 and fluorescence at 90% zinc occupancy = 1. The zinc binding affinity of the strong site was estimated using the following equation (121):

$$F = \frac{F_{min} * K_d EMI2^{ZRL} + F_{max} * [Zn_{Free}]}{K_d EMI2^{ZRL} + [Zn_{Free}]}$$

Equation 1

F is the fluorescence of $EMI2^{ZRL}$ after each titration.

$F_{max} = 1$.

$F_{min} = 0$.

$[Zn_{Free}]$ was estimated using the program SPE using pK_a and $logK_{Zn\text{-}TPEN}$ values of TPEN. (121, 130)

Weak binding site competitive chelation. In order to determine the zinc-binding affinity of the weak binding site, the strong-binding site of $EMI2^{ZRL}$ was filled with 1 molar equivalent of $ZnSO_4$. Because the difference in zinc-binding affinities is so great, virtually all of the added zinc should fill the strong-binding site. A 500 μM stock solution of FluoZin-3, Tetrapotassium Salt, Cell Impermeant (FZ3 - ThermoFisher #F24194) in MilliQ H_2O was created. $EMI2^{ZRL}$ (loaded with one molar equivalent of zinc) and FZ3 were added to Chelex-treated titration buffer in a quartz cuvette (Hellma #119F-10-40) at final concentrations of 2 μM and 20 μM, respectively, in a total volume of 2 ml. The solution was found to equilibrate after 5 minutes (Figure 3.6), so the solution in the cuvette was stirred for 5 minutes at 25C in the fluorimeter before each titration. 23 titrations of 2.5 μl 440 μM $ZnSO_4$ were performed to achieve a final zinc occupancy of 115% of the weak-binding site (107.5% zinc occupancy of $EMI2^{ZRL}$). FZ3 was excited at 425 nm. Emission was measured and integrated between 490 – 650 nm.

In order to determine the zinc-binding affinity of the weak-binding site, data between 10-90% zinc occupancy were analyzed using the program DynaFit. (131-133) The data were fit to the following equation:

$$S = S_0 + \Sigma_{i=1}^{n} r_i \, c_i$$

Equation 2

S is the fluorescence after each titration.

S_0 is offset on the signal axis from the instrument.

n is the number of molecular species in the reaction. n = 5 and the species are EMI2, Zinc, EMI2 bound to zinc, FluoZin-3, and FluoZin-3 bound to zinc.

c_i is the concentration of the ith species after each titration.

r_i is the molar response coefficient of the ith species.

The program solves a system of simultaneous first-order ordinary differential equations in order to determine concentrations at each timepoint and from those it estimates the K_D of EMI2's weak-binding site. (134)

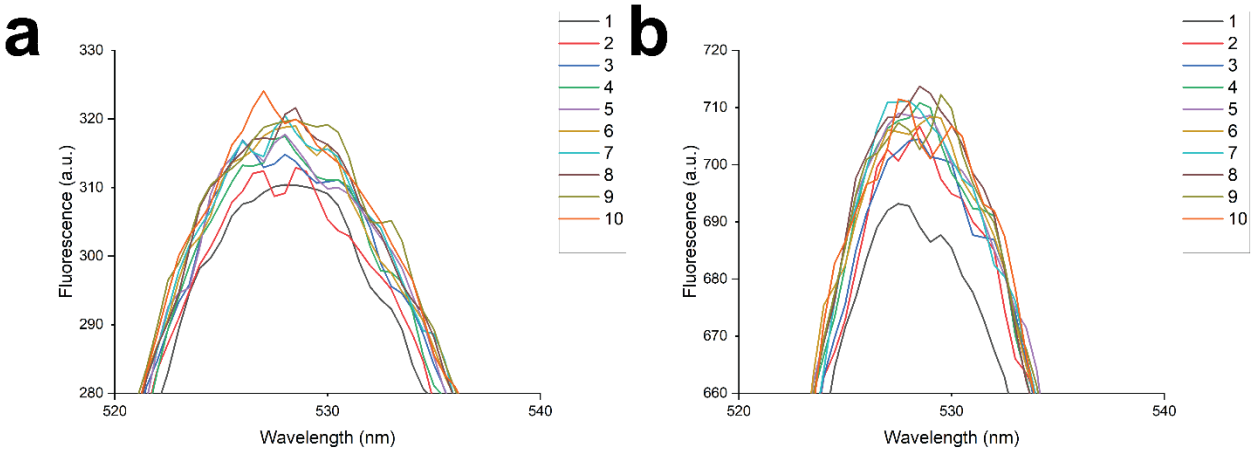

Minutes Post-Titration	Integrated Fluorescence	Percent Change
1	29703.42	
2	29965.47	0.87
3	30147.8	0.60
4	30242.9	0.31
5	30399.22	0.51
6	30546.3	0.48
7	30596.08	0.16
8	30611.42	0.050
9	30728.7	0.38
10	30711.69	0.055

Minutes Post-Titration	Integrated Fluorescence	Percent Change
1	65203.48	
2	66063.95	1.3
3	66369.94	0.46
4	66619.84	0.38
5	66737.46	0.18
6	66780.31	0.064
7	66777.75	0.0038
8	66870.91	0.14
9	66862.1	0.013
10	66888.87	0.040

Figure 3.6: Kinetics of FluoZin-3 competition demonstrating that equilibrium is reached within 5 minutes post-titration. **a.** Graph of fluorescence at 50% zinc occupancy. Each line represents one minute after zinc addition. **b.** Graph of fluorescence at 90% zinc occupancy. Each line represents one minute after zinc addition.

High-energy-resolution fluorescence detection spectroscopy. High energy resolution fluorescence detection (HERFD) spectroscopy data were collected at the SSRL using SPEC data acquisition software (Certified Scientific Software, Cambridge, Massachusetts, USA). Zn K near-edge spectra were measured on the 22 mm period 174-pole in vacuum undulator beam line 15-2 with Kirkpatrick-Baez focussing optics and employing a Si(311) double-crystal monochromator. All samples were measured at 10 K in HERFD mode using a single spherically bent Si(642) crystal analyzer in the Johan geometry with a 1 m Rowland's circle. (135) The Zn Kα1 fluorescence line with a peak emission energy of 8639.25 eV was used with the diffracted fluorescence measured using a silicon drift detector (Vortex EX-90, Hitachi High-Tech Science America, Inc.,

Schaumburg, Illinois, USA). The beam (size = 820 μm × 80 μm) was moved to a new position on the sample after every other scan; no photochemical changes to the sample (136) were observed between the first and second sweeps. Incident and downstream beam intensities were measured using photodiodes. Energy calibration was performed using the transmission spectra from a Zn foil positioned immediately downstream the sample between I1 and I2, with the first energy inflection assumed to be 9660.7 eV. All XAS data normalizing and processing was performed using EXAFSPAK (137) and MATLAB.

Chapter 4: The Effects of Chemical Fixation on the Metal Content of Eggs and Tissue

John F. Seeler, Yu-Ying Chen, Carole LaBonne, Teresa K. Woodruff, Reiner Bleher, Thomas V. O'Halloran

The data presented here are being prepared for publication in *Metallomics*.

The following people acquired and analyzed data used in this chapter:

Yu-Ying Chen: Modified Davidson's values in Table 4.1, Figure 4.6, Table B.4

Reiner Bleher: Figures 4.4 and 4.5

Abstract

The increasing sensitivity of electron- and X-ray-based analytical microscopes can provide images of biological samples at high spatial resolution with atomic-level sensitivities on the order of 10^5 atoms/μm^3, depending upon the element. Several of these imaging methods require sample preparation steps involving ultrathin sectioning of fixed and/or polymer-embedded samples. Chemical fixation of cells and tissues can lead to loss and redistribution of unbound and weakly-bound non-crystalline, diffusible elemental content or leaching of elements that are not tightly bound in the biological matrix. Timm's method was developed to retain the initial distribution of weakly-bound pools of transition metal ions in brain tissue by the formation of sulfide nanocrystals. In order to determine if a modified form of this fixation method, which bypasses the addition of silver, accurately preserves metal contents, we compared the elemental content of cell (*Xenopus laevis* eggs) and tissue (*Mus musculus* ovary) samples as determined by solution-based analytical methods. In *Xenopus* eggs the elemental content of the majority of transition metals was unchanged after sulfide treatment and we surprisingly obtained similar results for the non-sulfide treated group. There was a significant loss of sodium, phosphorus, and potassium in both treatment groups. Analysis of elemental localization within the eggs via scanning transmission electron microscopy energy dispersive X-ray spectroscopy showed similar results for both treatment groups. In the case of mouse ovaries, we find that sulfide fixation preserves zinc content but other transition metal content can become skewed during fixation. A common fixation protocol that employs acidic conditions (modified Davidson's) severely disrupts metal content. The data therefore suggest that transition metal retention is dependent on tissue type and fixation method.

Introduction

Elemental analysis has shown that chemical fixation leads to a significant loss of tissue metal content as the fixatives permeabilize membranes. (81-83, 138) Additionally, most diffusible ions (such as Na^+ and K^+) leave the cell during fixation. (80, 85) Previous research in our group has used an aldehyde fixative containing sulfide to preserve the zinc content of mouse eggs. (6) The method starts with the first step in Timm silver staining (88), i.e. addition of a solution of NaSH directly to biological samples. (90) At physiological pH, NaSH contains neutral H_2S, which can diffuse across biological membranes and into compartments that contain soluble and chemically available metal ions to ultimately form insoluble metal sulfides. In Timm's original method, aqueous solutions of silver salts and reducing agents are then added to the sample: under these conditions, Timm suggested that the metal sulfide deposits catalyze the formation of metallic silver particles, which are readily observed by light microscopy and electron microscopy. (88, 89, 139) In the decades following Timm's original publication his method has been adapted and modified: one common variation replaces alcohol with a glutaraldehyde solution; others replace the sulfide sources with selenide. (90) When one moves beyond tissue-based histochemistry into the realm of cellular and subcellular microcopy applications, a significant problem arises: the silver reaction in fact displaces the native metal (Emily Que and Reiner Bleher., unpublished data). Another drawback of the silver treatment is that the deposition of silver on the sulfide particles continues as long as there are silver ions and reducing agents available near the particle (86), so the size of the particle can grow well beyond the boundaries of the subcellular compartment. Thus the size of the particle often does not correspond to the size of the original subcellular compartment that contained the native metal ion. (88)

Our group's prior research in the inorganic physiology of the egg has demonstrated that the accumulation and release of zinc in cortical granules (CGs) play critical roles in development and fertilization. (4, 6, 7) These processes occur in monkeys (7), *H. sapiens* (15), *B. taurus* (16), *D. melanogaster* (20), *A. mexicanum* (17), and *D. rerio* (17, 18). The same zinc spark event is conserved in *Xenopus laevis* (the African Clawed Frog), an amphibian. Notably, we found the *Xenopus* egg CGs also contain manganese that is released following fertilization. (140)

Given the critical physiological roles of metal-containing vesicles, it is imperative to develop protocols that accurately quantify their elemental contents and spatially resolve their locations. The cortical vesicles in the fixed mouse egg were imaged with scanning transmission electron microscopy energy dispersive X-ray spectroscopy (STEM-EDS) and X-ray fluorescence microscopy (XFM). Importantly, Que *et al.* could not detect zinc within the CGs with these techniques unless the fixed mouse egg was also treated with sulfide. The native locations of the zinc granules in the mouse egg were preserved with a modified Timm's sulfide treatment protocol that also eliminated the silver enhancement step. (6) However, it is possible that the sulfide fixation step could still lead to some loss of zinc from the CGs. Because of the small size of mouse eggs (around 72 μm in diameter) (141) we were unable to quantify this possible change either via bulk elemental analysis or through the creation of frozen samples.

Xenopus eggs are ideal models to probe whether sulfide fixation can perturb cellular elemental content. Not only is the volume of a frog egg approximately 5000-fold greater than that of a mouse egg, a frog will provide hundreds of eggs in a single day. Herein, we employ inductively coupled plasma optical emission spectroscopy (ICP-OES) and inductively coupled plasma mass spectrometry (ICP-MS) to quantify the elemental contents of fixed *Xenopus* eggs with and without

sulfide treatment. To determine if metal localization changes following fixation, we used STEM-EDS to image the cortices of the frog eggs. Although we are most interested in transition metals, we analyzed other elements as well because of the broad range of ICP and STEM-EDS. Finally, to compare the *Xenopus* results with those of a different tissue type, we measured the elemental content of mouse ovaries treated with a range of different fixatives.

Results

Cryogenic fixation with high-pressure freezing or plunge freezing is the best sample preparation method for preserving both the content and ultrastructural location of mobile ions as well as soluble, unbound proteins and small molecules. (85, 142-146) However, with a diameter of 1.2–1.3 mm, *Xenopus* eggs are too large for high-pressure freezing and we therefore needed to chemically fix the samples. We fixed with a glutaraldehyde-formaldehyde mixture because it has been shown to better preserve metal content than formalin does. (82) Previous work has shown that fixation of *Xenopus* oocytes and embryos in 5% glutaraldehyde did not significantly alter measured zinc content. (41)

While glutaraldehyde or formaldehyde treatments “fix” large biopolymers and proteins in place in the cell by forming intermolecular crosslinks, these treatments do not “fix” most low molecular weight ionic species and complex ions. Zinc-specific fluorescent probe staining of CGs in mouse eggs was lost after treatment with sulfide, meaning that the two methods are not mutually compatible. (6) To directly address whether any of these fixation steps alone or in combination can lead to artifacts that alter metal content, we compared bulk metal content of *Xenopus* eggs after each step in the sample preparation process.

Metal Content of Solutions Used in Fixation

	Na (M)	Mg (M)	K (M)	Ca (M)	Mn (M)	Fe (M)	Cu (M)	Zn (M)	n
diH_2O	4×10^{-7}>	8×10^{-7}>	3×10^{-7}>	3×10^{-8} >	9×10^{-9} >	2×10^{-8} >	$4.1 \pm 2.3 \times 10^{-7}$	$2.0 \pm 1.2 \times 10^{-7}$	12
Ethanol	7×10^{-7}>	1×10^{-6} >	4×10^{-7}>	$2.0 \pm 0.14 \times 10^{-7}$	1×10^{-8} >	$6.1 \pm 8.2 \times 10^{-8}$ *	1×10^{-8} >	1×10^{-8} >	4
Formaldehyde	> 4×10^{-3}	7×10^{-6}>	$1.5 \pm 0.040 \times 10^{-5}$	$1.5 \pm 0.050 \times 10^{-6}$	6×10^{-8} >	$2.3 \pm 0.41 \times 10^{-7}$	$8.0 \pm 1.3 \times 10^{-8}$	$2.9 \pm 0.21 \times 10^{-5}$	4
Glutaraldehyde	$8.9 \pm 0.039 \times 10^{-5}$	$3.5 \pm 0.077 \times 10^{-8}$	$9.8 \pm 0.18 \times 10^{-6}$	$3.8 \pm 0.081 \times 10^{-6}$	$3.9 \pm 4.5 \times 10^{-7}$ *	$5.7 \pm 2.4 \times 10^{-6}$	5×10^{-7} >	$8.8 \pm 0.056 \times 10^{-7}$	3
Fixative	> 3×10^{-3}	5×10^{-6}>	$4.2 \pm 0.071 \times 10^{-4}$	$1.2 \pm 0.14 \times 10^{-7}$	6×10^{-8} >	$5.3 \pm 3.1 \times 10^{-7}$	$1.9 \pm 0.10 \times 10^{-7}$	$3.0 \pm 0.14 \times 10^{-6}$	4
Fixative (NaSH)	$2.7 \pm 0.10 \times 10^{-2}$	5×10^{-6}>	$1.0 \pm 0.0056 \times 10^{-3}$	$5.0 \pm 0.061 \times 10^{-6}$	5×10^{-8} >	$4.2 \pm 0.19 \times 10^{-7}$	$1.5 \pm 0.029 \times 10^{-7}$	$2.8 \pm 0.097 \times 10^{-6}$	4
Embed 812	$5.9 \pm 0.28 \times 10^{-5}$	$7.8 \pm 0.70 \times 10^{-6}$	$2.8 \pm 0.15 \times 10^{-5}$	$1.1 \pm 0.036 \times 10^{-5}$	9×10^{-7} >	$2.3 \pm 0.10 \times 10^{-6}$	8×10^{-7} >	$4.9 \pm 0.14 \times 10^{-6}$	3
Modified Davidson's	$1.9 \pm 0.042 \times 10^{-5}$	$3.1 \pm 0.49 \times 10^{-7}$	$1.5 \pm 0.18 \times 10^{-6}$	$2.4 \pm 0.95 \times 10^{-6}$	$1.5 \pm 0.038 \times 10^{-8}$	$5.3 \pm 0.26 \times 10^{-7}$	$1.9 \pm 0.14 \times 10^{-8}$	$9.3 \pm 0.19 \times 10^{-7}$	3-4

Table 4.1: Metal content of solutions used during fixation. There is significant iron contamination in the glutaraldehyde and Embed 812 and significant zinc contamination in the formaldehyde. Fixative: 2.5% glutaraldehyde, 2% formaldehyde in 0.1 M PIPES buffer. Fixative (NaSH): 2.5% glutaraldehyde, 2% formaldehyde in 0.1 M PIPES buffer with 20 mM NaSH. Values in M. Mean ± SD. *: Some values are below the standard curve.

Transition Metal Content is Preserved in *Xenopus* Eggs Following Fixation

We began by determining the metal contents of the solutions used in the fixation process in order to measure their levels of metal contamination (Table 4.1). Fixatives have previously been suspected of containing significant amounts of transition metals. (81) The DI water coming from the university's taps contained copper and zinc on the order of 10^{-7} M. This should be considered high when analyzing trace metals in biological samples. The fixative solutions used in this study contained iron and copper on the order of 0.1 μM, with zinc present at approximately an order of magnitude higher concentration (Table 4.1). An exception was the glutaraldehyde solution where the iron concentration was 6 μM. Finally, iron and zinc concentrations are also high in the Embed 812 resin relative to the other solutions. In an initial experiment in which the unfixed eggs were washed with MilliQ H_2O and the fixed eggs with diH_2O, there was a statistically significant increase in copper between the two groups (Figure 4.1, see Table B.1 for numerical values). Although the diH_2O has a lower copper concentration than the eggs ($4.1 \pm 2.3 \times 10^{-7}$ M vs. $5.0 \pm 0.28 \times 10^{-6}$ M), the 50% spike in copper content at the fixed but not dehydrated stage can be attributed to 10 eggs being in approximately 0.5 ml diH_2O before drying. Subsequent studies employed MilliQ H_2O, which eliminated the artifact.

Copper Contamination from DI Water

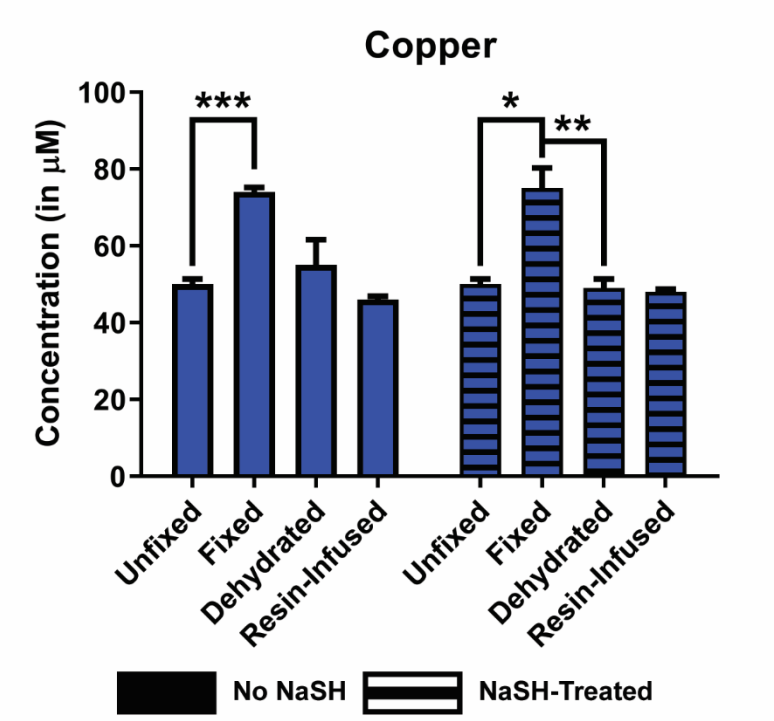

Figure 4.1: Copper content of unfixed eggs washed with MilliQ H_2O and fixed eggs washed with diH_2O. diH_2O contains enough residual copper to contaminate samples. Solid bars: Elemental content of *Xenopus* eggs fixed with paraformaldehyde and glutaraldehyde. Striped bars: Elemental content of *Xenopus* eggs fixed with paraformaldehyde, glutaraldehyde, and NaSH. Values in mM. Mean ± SEM, N = 4 frogs. *: 0.05 > p, **: 0.01 > p, ***: 0.001 > p.

Treatment with a formaldehyde-glutaraldehyde mixture led to a statistically significant loss of potassium content during the fixation step but no significant effect on other Group 1 and 2 metal (Figure 4.2, Tables B.2 and B.3) or on transition metal content (Figure 4.3, Tables B.2 and B.3). We note that aldehyde treatment alters the interior architecture of the eggs and permeabilizes their membranes (142) and the loss of potassium is expected according to previous studies. (80, 87) Given that potassium is found at higher concentrations than any other metal ion in most cell types, and given that a majority of the K^+ ions are not tightly bound in intracellular sites, we infer from

these results that formaldehyde-glutaraldehyde fixation disrupts the plasma membrane to the extent that potassium ions can leak from the cell.

No significant change in calcium or magnesium was observed upon fixation, which is surprising given their propensity to become redistributed and partially or completely lost. Eggs were fixed directly in 0.1X MMR buffer. Given that the buffer contains sodium, magnesium, and calcium, albeit the latter two at micromolar levels, those values in Figure 4.2 may not represent actual intracellular calcium or magnesium content. More likely, however, would be that the majority of calcium and magnesium is tightly bound in frog eggs. In the egg, much of the calcium is stored in the endoplasmic reticulum and used as a signaling agent following fertilization (93), so it is possible that the ER protects the calcium from the effects of the fixatives. Much of the magnesium is bound to nucleic acids, so as the mobile NTPs are removed from the egg during the fixation and dehydration process the magnesium travels with them.

There is a small increase in sodium content in the fixed eggs. The fixative solutions contain sodium at millimolar levels (Table 4.1), which combined with the 10 mM NaCl in the 0.1X MMR may account for this. As a mobile ion, sodium levels should drop during the fixation process (80), and they are significantly lower in the resin-infused eggs compared to the control.

Phosphorus content showed the same significant drop in both treatment groups between unfixed and resin-infused cells (31 ± 6.1% in control, 31 ± 4.9% in sulfide-fixed eggs). Like the loss of potassium upon fixation, the drop in phosphorus is most likely due to permeabilization of the membrane. Nucleoside triphosphates (NTPs) (147, 148) and inorganic phosphate (P_i) (148) are at low millimolar concentrations in the *Xenopus* egg, and are not likely to crosslinked by the aldehydes, but can leak after membranes are compromised. However, only around 4% of total

intracellular phosphorus is inorganic or contained in NTPs, with the majority of phosphate in the egg contained in yolk proteins (phosvitin and lipovitellin) and a significant amount in lipids as well. (148) Both glutaraldehyde and formaldehyde can cause lipid loss, with the majority occurring during dehydration. It is possible that the aldehydes create microscopic cracks in the fixed tissue, increasing the surface area with which the solvents can interact. (149) Lipids are not crosslinked by aldehydes and to avoid interference with STEM-EDS analysis we did not use any typical post-fixation treatments that increase contrast, such as uranyl acetate, which reacts with phosphate and amino groups (150), or osmium tetroxide, which reacts with unsaturated dicarbon bonds in cellular membranes. (151, 152) Phosphorus content probably continues to drop between the dehydration and resin-infusion steps because the resin is first introduced to the samples in a 1:1 mixture with ethanol.

Besides an anticipated increase in sulfur content (ca. 50%) following sulfide treatment, few differences in elemental content between the control and NaSH-treated eggs were observed. Total transition metal content in the egg was 3.0 mM, whereas total sulfur content increased by 70 mM following the fixation step (Table B.3). Assuming that virtually all of the metal reacts with sulfide, the sulfide therefore creates other moieties, i.e. through binding to biopolymers.

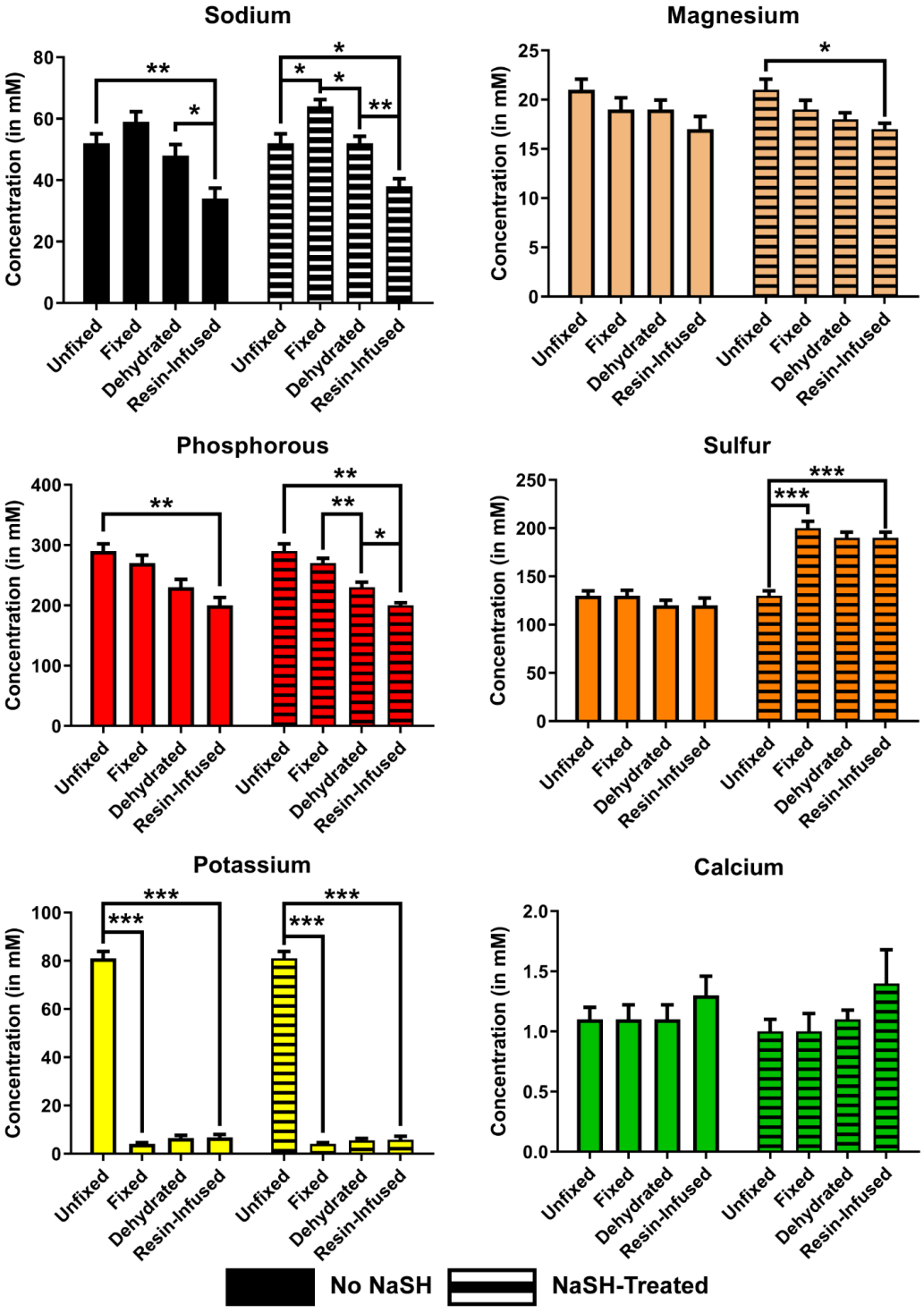

Figure 4.2: Transition metal content of *Xenopus* eggs during sample preparation. There is no change in manganese, copper, and zinc content of eggs fixed without NaSH, while there is iron contamination in both treatment groups. Solid bars: Elemental content of *Xenopus* eggs fixed with formaldehyde and glutaraldehyde. Striped bars: Elemental content of *Xenopus* eggs fixed with formaldehyde, glutaraldehyde, and NaSH. Mean ± SEM, n = 4 frogs. *: 0.05 > p.

The concentrations of manganese, copper, and zinc were preserved following fixation with sulfide. Surprisingly, unlike in mouse eggs, there was no significant change in the content of these metals in the non-sulfide-treated group. It is probable that the majority of the metal pool is tightly bound inside the egg. Over 90% of total intracellular zinc in *Xenopus laevis* eggs is bound to proteins in a type of organelle called the yolk platelet. (41) Additionally, we have found manganese, copper, and zinc are stored and tightly bound in cortical vesicles. Following fertilization, manganese and zinc are released from the egg in what is probably a highly regulated process.

The significant increase in total iron content between unfixed and resin-infused eggs (84 ± 32% for the control and 90 ± 47% for the sulfide-fixed eggs) was surprising. It is likely that the glutaraldehyde and Embed 812 contribute to the fixation-induced iron contamination in these samples.

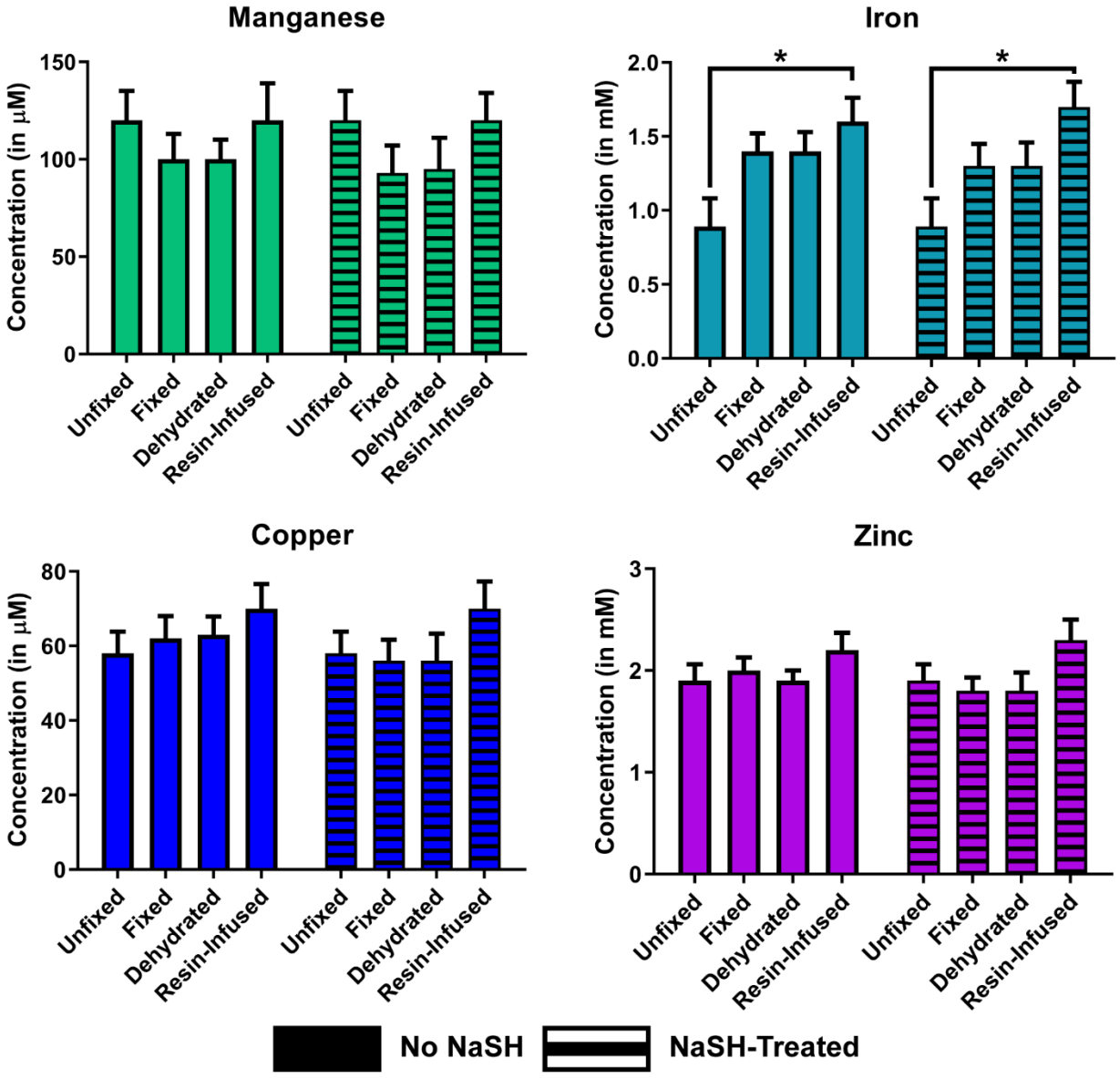

Figure 4.3: Transition metal content of *Xenopus* eggs during sample preparation. There is no change in manganese, copper, and zinc content of eggs fixed without NaSH, while there is iron contamination in both treatment groups. Solid bars: Elemental content of *Xenopus* eggs fixed with formaldehyde and glutaraldehyde. Striped bars: Elemental content of *Xenopus* eggs fixed with formaldehyde, glutaraldehyde, and NaSH. Mean ± SEM, n = 4 frogs. *: 0.05 > p.

Elemental Localization Does Not Change in *Xenopus* Egg Cortices

Aside from fixation-induced artifacts of iron contamination, we did not see a significant change in the transition metal content in eggs fixed without NaSH compared to those fixed with it. Although overall metal content did not change, it is possible that metal localization changed due to the presence of the sulfide. In order to explore this possibility, we analyzed the cortices of the eggs using STEM-EDS. The cortices have vesicles of around 500 nm in diameter that each contains multiple metals (Ca, Mn, Co, Ni, Cu, and Zn) (140), as well as larger yolk platelets that contain phosphoproteins. (42) Surprisingly, there is little difference in metal localization between the control and sulfide-containing eggs (Figure 4.4). Ca, Cu, and Zn were localized to the small sulfur-containing vesicles (concentrations of Mn, Co, and Ni were too low to be detected with our EDS system). Phosphorus is found throughout the cytoplasm, with higher concentrations in the yolk platelets. Mg, K, and Fe are randomly distributed throughout the slices (Figure 4.5). It is probable that at least in *Xenopus* eggs the metal contents are held tightly enough within intracellular vesicles that fixatives do not rinse them out.

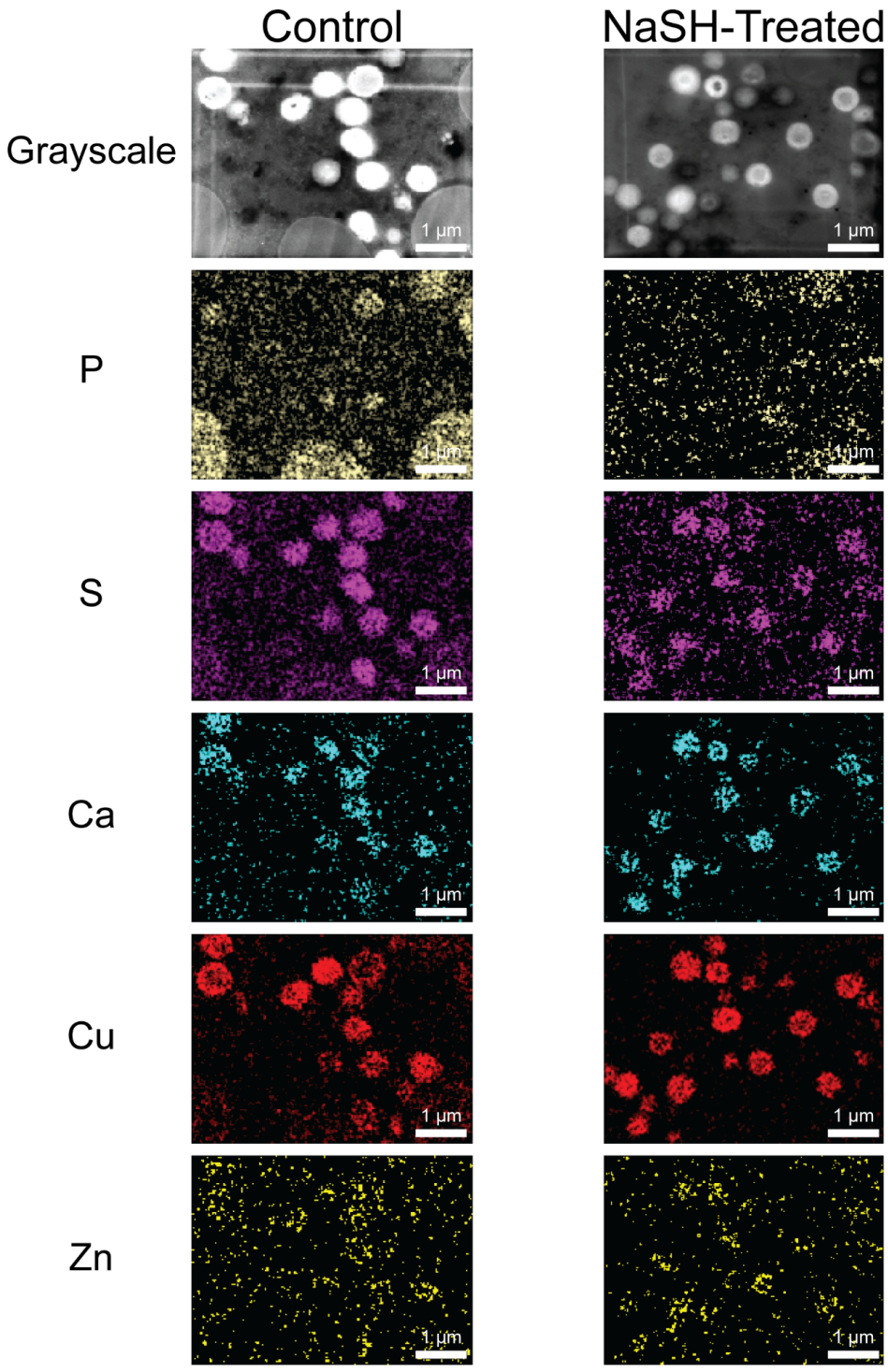

Figure 4.4: STEM-EDS images of slices of eggs fixed with and without NaSH. Metal localization is similar in both treatment conditions. The larger vesicles containing phosphorus are yolk platelets, while the smaller metal-rich vesicles are cortical granules. Images of the egg cortex. Slice thickness = 200 nm.

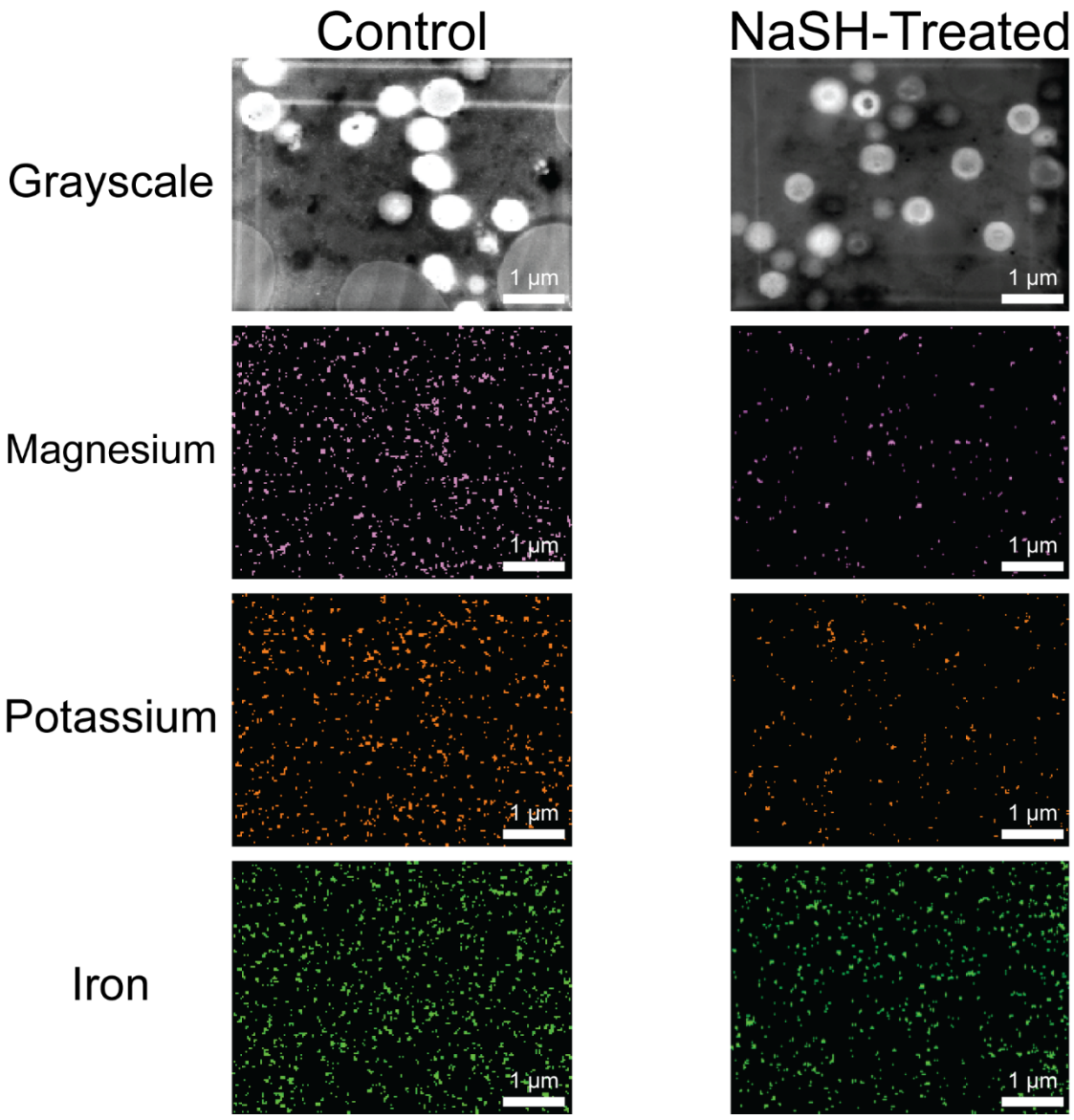

Figure 4.5: STEM-EDS images of slices of eggs fixed with and without NaSH. Magnesium, potassium, and iron show no pattern of localization in either treatment condition. Images of the egg cortex. Slice thickness = 200 nm.

Elemental Changes in Mouse Ovaries Following Fixation

In order to evaluate the effects of several aldehyde and sulfide fixation methods on the elemental content of multicellular tissue, we fixed and then analyzed mouse ovaries via ICP. In contrast to the frog egg, the ovary contains many fluid compartments and cell types, with the major

ones being germ, granulosa, stromal, endothelial, immune, and smooth muscle cells. (153) We expect the cells in a heterogenous sample to have different elemental profiles and different responses to treatment with fixatives.

Whole ovaries from 12-week-old non-perfused mice were collected, so there was some blood content in the samples. Ovaries were fixed in one of the following solutions: modified Davidson's fixative (MD), formaldehyde (FA), glutaraldehyde with formaldehyde and NaSH (GA/FA/NaSH), or with glutaraldehyde and formaldehyde (GA/FA). The MD solution contains 6.25% acetic acid and acts both as a cross-linking and a denaturing fixative and is commonly used for the histological preparation of gynecological tissues. (154, 155) According to ICP analysis, the manganese, iron, copper, and zinc contents of the MD solution are on the order of 10^{-7} – 10^{-8} M (Table 4.1), which should introduce minimal contamination to the samples.

When compared to the unfixed control ovaries, the calcium and magnesium contents were reduced by more than 65% in all fixation conditions, and there was a virtual elimination of potassium (Figure 4.6, see Table B.4 for numerical values). There were significant drops in phosphorus (30–42%) in all fixation conditions. These drops were expected because the permeabilization of the membranes should lead to a loss of mobile metal ions. However, there was a significant (49–66%) increase in sodium in the FA, GA/FA/NaSH, and GA/FA-fixed ovaries, while the ovaries fixed in MD showed a 100 ± 4.4% drop (n = 7, mean ± SEM). As stated above, the FA, the GA/FA, and the GA/FA/NaSH contained sodium on the millimolar range (Table 4.1), while the pre-mixed MD contained sodium at a concentration at least 100-fold lower. Since sodium loss is expected following fixation and it only occurred in the MD-fixed ovaries, it is possible that the other fixatives introduced it. There was a significant drop in sulfur content in all conditions

(24–43%) except for those ovaries treated with GA/FA/NaSH, in which there was a 39 ± 4.8% gain (n = 8, mean ± SEM).

Among the transition metals, manganese levels decreased by 29–63% in all treatment conditions. There was no significant change in iron levels, except for a 11 ± 4.1% (n = 7, mean ± SEM) drop in the GA/FA-treated ovaries. Copper decreased by 23–28% in both the GA/FA/NaSH and GA/FA conditions. Zinc showed a 9–73% decrease in MD, GA/FA/NaSH, and GA/FA fixed eggs, while there was a 27 ± 8.2% (n = 8, mean ± SEM) gain in FA-fixed eggs. Overall, MD treatment led to greater changes in transition metal levels (except for iron) than fixation with pure formaldehyde. The MD solution contains 6.25% acetic acid and thus the pH is much lower (pH 3.5) than the other fixatives prepared in buffer or in MilliQ H_2O. Because of this, it is possible that MD treatment of the tissue sections only mobilizes metals that are not tightly bound. For example, the majority of iron ions in the mouse ovaries may be held in heme prosthetic groups or in iron sulfur clusters that are insensitive towards acetic acid (156), while manganese and zinc are more readily mobilized. In support of this idea we note that heme prosthetic groups can be covalently bound to proteins: those that are not covalently bound exhibit very low dissociation constants (i.e. picomolar range). (157, 158) Copper is found in a wide range of metalloprotein binding sites, and many of these sites have tighter binding affinities than those of most other metals, including zinc. (159, 160) Zinc fingers, on the other hand, have a wide range of binding affinities, with many of them lower. (128) Interestingly, treatment with FA alone led to a 25% increase in tissue zinc levels; however, the source of that increase is unclear and probably due to sample contamination.

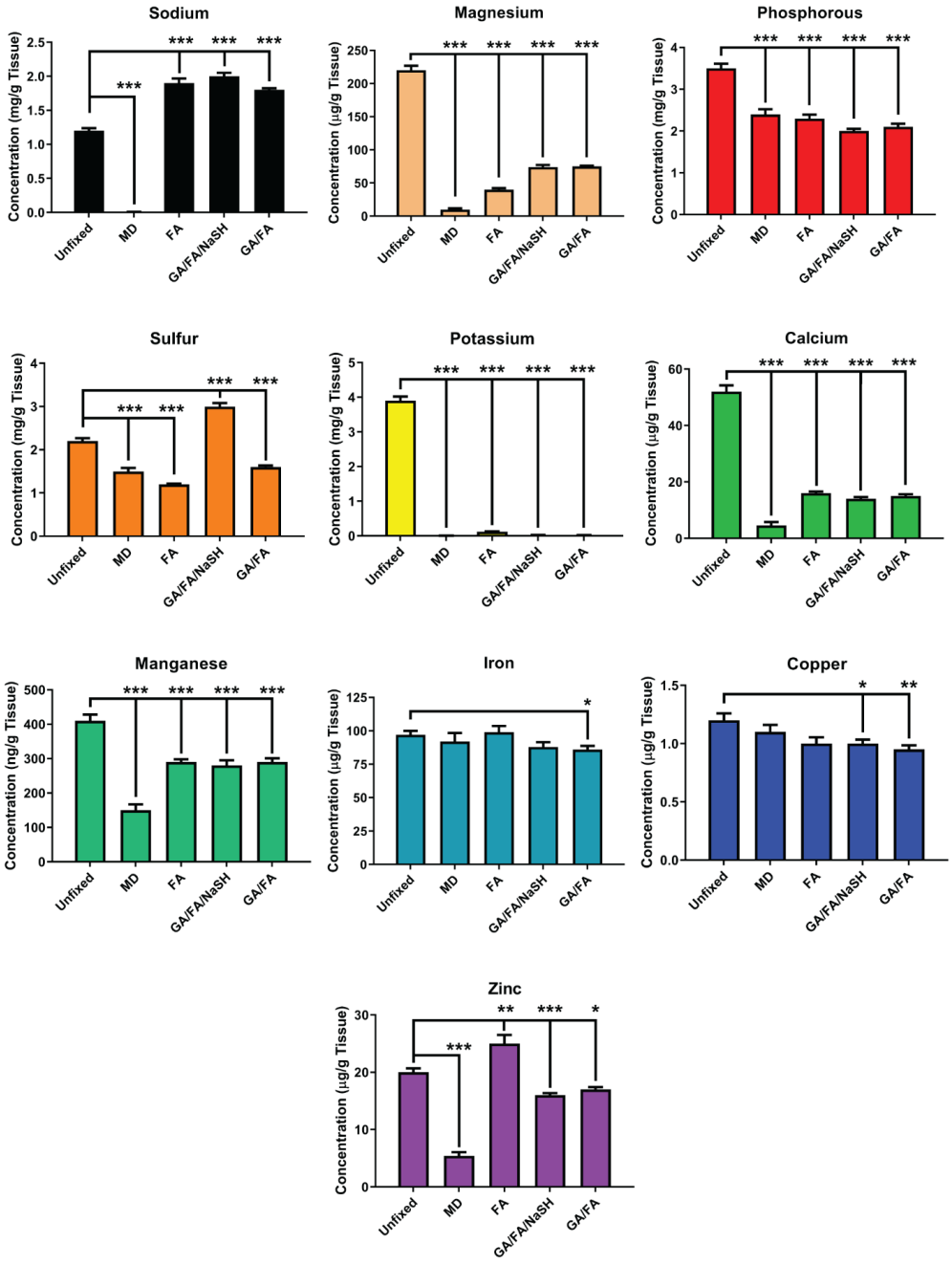

Figure 4.6: Fixed mouse ovaries show a greater decrease in s block metal ions than in transition metals. Elemental content of mouse ovaries (by wet weight) fixed with the following: MD: modified Davidson's Fixative (14% denatured ethanol, 37.5% formalin, 6.25% acetic acid in diH_2O), FA: 4% formaldehyde in diH_2O, GA/FA/NaSH: 2.5% glutaraldehyde, 2% formaldehyde in 0.1 M PIPES buffer with 20 mM NaSH, GA/FA: 2.5% glutaraldehyde, 2% formaldehyde in 0.1 M PIPES buffer. Values as mean ± SEM, n = 7-8 ovaries per condition. p values compare the change in elemental content between unfixed ovaries and the different fixation conditions. *: 0.05 > p, **: 0.01 > p, ***: 0.001 > p.

Conclusion

Here we show how specific chemical fixation protocols can induce changes in the metal content of cell and tissue samples. While several protocols introduce minor changes in metal content that can be controlled for, other methods introduce artifacts that completely remove some elements. Other researchers have shown that the retention of labile metal ions is based on tissue or cell type: the biochemical composition of different samples has a significant impact on the mobilization of metal ions during fixation. (146) Here we show how specific fixation protocols perturb two types of samples in reproductive biology. *Xenopus* eggs are single cells, while the mouse ovary is a heterogenous collection of cell types, including follicle structures that contain oocytes in a variety of developmental stages. The two sample types have different extracellular environments: eggs from this amphibian species are laid in hypotonic bodies of water and have evolved to be impermeable to ion loss. (161) In contrast, the ovary contains both cells and extracellular space and as an internal organ is not a self-contained system. Because of this, we anticipated different responses to chemical perturbations involved in each type of fixation protocol.

In the case of unfixed *Xenopus* eggs, we found the majority of the elemental contents to be consistent with literature values determined with atomic absorption spectroscopy and flame spectroscopy methods, (Table 4.2). In *Xenopus* eggs, fixation using aldehydes with or without sulfide does not alter the cellular Ca, Mn, Cu, and Zn contents and allows for ultrastructural study of subcellular distribution. Overall elemental localization within the frog eggs remains similar despite treatment with sulfide. In mouse ovaries, none of the fixation protocols preserved transition metal content. Fixation with MD is actually slightly less effective than fixation in pure formaldehyde. Fixation with NaSH does not appear to alter metal content of tissue that has

undergone aldehyde crosslinking, only preserving the content of one of the four measured transition metals. We attribute the greater metal loss from the ovaries compared to the frog eggs to the more robust nature of latter: *Xenopus* eggs are externally fertilized and they have evolved to function in an unregulated extracellular environment where they have numerous barriers to exchange with extracellular fluids and components.

Literature *Xenopus* Egg Elemental Content

Na (mM)	Mg (mM)	P (mM)	S (mM)	K (mM)	Ca (mM)	Mn (mM)	Fe (mM)	Ni (mM)	Cu (mM)	Zn (mM)	Source
52 ± 3.1 (ICP)	21 ± 1.1 (ICP)	290 ± 12 (ICP)	130 ± 5.0 (ICP)	81 ± 2.9 (ICP)	1.1 ± 0.10 (ICP)	0.12 ± 0.015 (ICP)	0.89 ± 0.19 (ICP)	Below LOD (ICP)	0.058 ± 0.0058 (ICP)	1.9 ± 0.16 (ICP)	This Paper
	13.5 ± 1.3 (AAS)				4.02 ± 0.37 (AAS)	0.18 ± 0.018 (AAS)	0.59 ± 0.07 (AAS)	0.003 ± 0.0005 (AAS)	0.031 ± 0.002 (AAS)	1.1 ± 0.05 (AAS)	(43)
~20 (ACT)											(162)
24.3 ± 2.3 (ACT)				91.0 ± 15.2 (ACT)							(163)
	20 ± 1 (AAS)	210 ± 21 (NMR)			2.0 ± 0.4 (AAS)						(148)
58.6 (ACT)				87.3 (FS/ACT)							(91)
60.7 ± 2.6 (FS), 14.3 ± 1.2 (ACT)	15.90 ± 0.69 (FS)			58.5 ± 2.0 (FS)	7.4 ± 1.23 (FS)						(164)

This Paper: Mean ± SEM, n = 4 frogs
1. Mean ± SD, n = 10. Values provided as ng/oocyte, converted to mM
2. No statistics provided in paper
3. Average of egg to 4-cell stage. Mean ± SD, n = 14 (Na), n = 40 (K)
4. Error type and n not given. Values given as nmol/egg, converted to mM
5. Mean, n = 89 (Na), n = 112 (K). Combined values of embryo measured at first and second cleavage. Combined FS and ACT measurements for K
6. Mean ± SEM, n = 22 (Na and K), n = 6 (Mg and Ca)

Table 4.2: Literature values of *Xenopus* egg/early embryo elemental content. Data in mM. Data acquired using the following techniques: AAS: Atomic absorption spectroscopy, ACT: Activity, FS: Flame spectroscopy, ICP: Inductively coupled plasma mass spectrometry/optical emission spectroscopy, NMR: Nuclear magnetic resonance.

Cells have an overcapacity for chelating transition metals (165-167): they actively transport several metals and ultimately accrue them to concentrations that are several orders of magnitude higher than what is observed in most physiological fluids of multicellular organisms. This may explain why the treatment of cells with reagents that have transition metal contaminants at low concentrations can ultimately lead to doping of the samples: if the contaminating metals are bound much less tightly in the components of the fixatives, they may be taken up and bound by intracellular factors and thus skew the apparent metal content to higher levels.

Another concern is that some transition metal ions can be sequestered or stored in intracellular compartments in labile or rapidly exchanging states; however, it appears that a majority of transition metal ions are bound tightly in metalloenzyme sites that exchange slowly. In the latter case, we anticipate that the loss of membrane integrity itself would lead to minor losses of some transition metals; however, cells that compartmentalize significant pools of labile metals, such as the mouse egg (6) or mossy fiber terminals in the hippocampal formation of mammalian brains (2) may be susceptible to more significant losses upon treatment with membrane-permeable reagents and conditions. For instance, a previous study in which formaldehyde fixation of mouse brains showed transition metal losses of at most 20%. (87)

Comparison of element profiles in unfixed samples

By converting the data in Figures 4.2 and 4.3 into g element/g tissue (Figures 4.7 and 4.8) we can perform a rough comparison of elemental concentration in unfixed *Xenopus* eggs and mouse ovaries. The higher phosphorus content in the *Xenopus* eggs is likely due to the yolk phosphoproteins: these act as nutrient stores that are consumed until the tadpole starts feeding itself. (148) Both potassium and calcium are higher in the unfixed ovary than in the frog egg. All cells contain less sodium than potassium, with human cells having a sodium to potassium ratio of

1:10. (168) The whole ovary samples have a 1:2.9 ratio, probably because as complete organs they contain matrix tissue components between the various follicle structures as well as extracellular fluid, which has a higher sodium: potassium ratio than intact cells. Surprisingly, unfixed single *Xenopus* eggs have a lower ratio (1:1.6), though it increases during development and is higher in adult cells, with much of the sodium contained (and bound) in the egg is transported to the intracellular fluid during embryonic development. (91, 164) There are significant differences in transition metal content between the two sample sets. The mouse ovaries have 3-fold more iron, probably due to residual blood, as the animals were not perfused, while the *Xenopus* eggs have 2-fold more copper, 4-fold more zinc, and 10-fold more manganese than the ovarian tissue. The manganese plays a role in fertilization; over 50% is released following sperm entry and acts as a block to fertilization (140), possibly by preventing polyspermy. (46) *Xenopus* eggs contain 3-fold more copper and 5-fold more zinc than mammalian eggs. (13) Because *Xenopus* embryos are closed systems until hatching, they need to contain all the necessary nutrients for development, unlike mammalian embryos, which develop in the womb. (43) Limiting zinc (169) and copper (170) leads to teratogenic effects in developing *Xenopus* embryos.

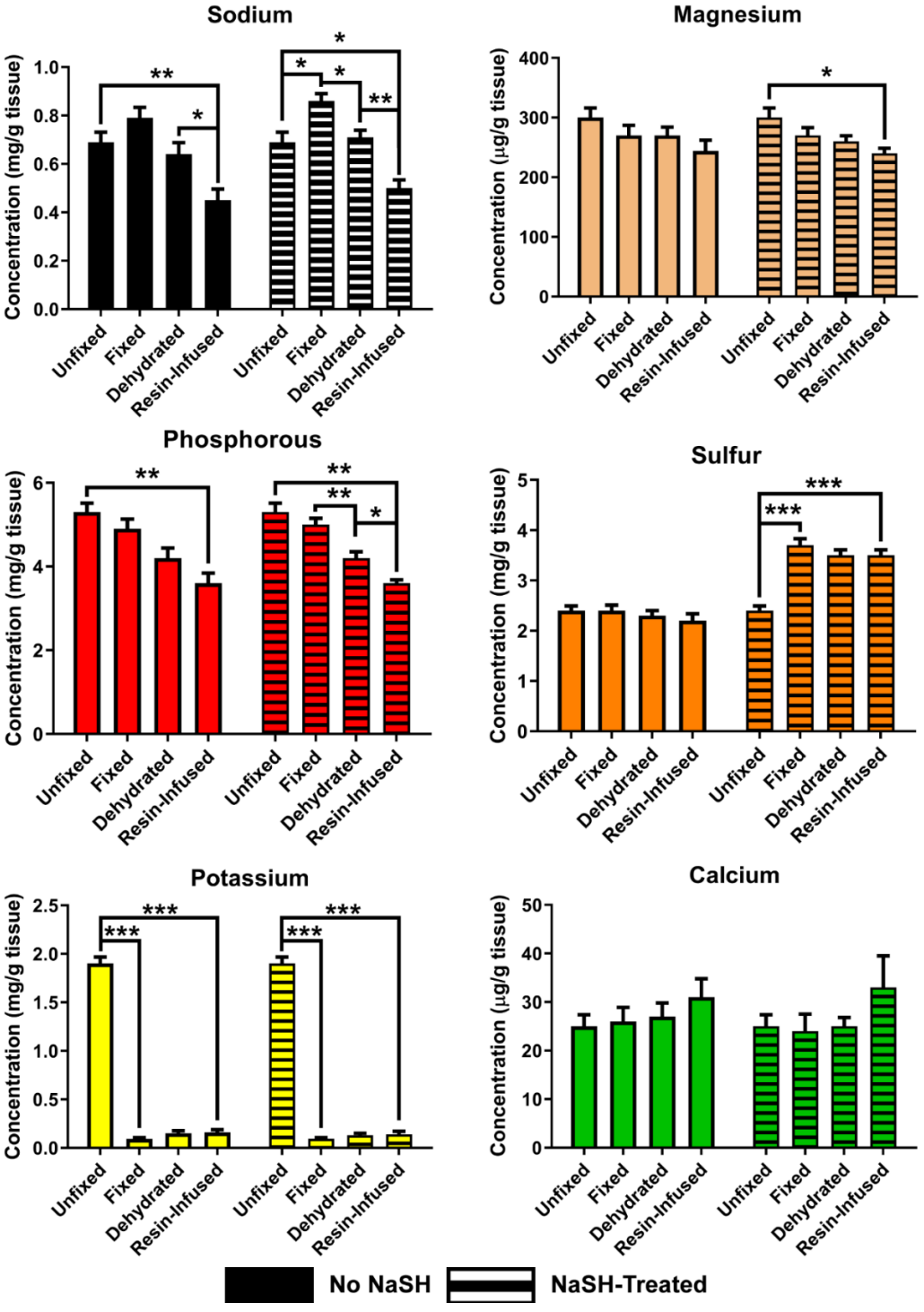

Figure 4.7: Elemental content of *Xenopus* eggs during different stages of fixation graphed as g element/g tissue (wet weight). Solid bars: Elemental content of *Xenopus* eggs fixed with formaldehyde and glutaraldehyde. Striped bars: Elemental content of *Xenopus* eggs fixed with formaldehyde, glutaraldehyde, and NaSH. Mean ± SEM, n = 4 frogs. *: 0.05 > p, **: 0.01 > p, ***: 0.001 > p

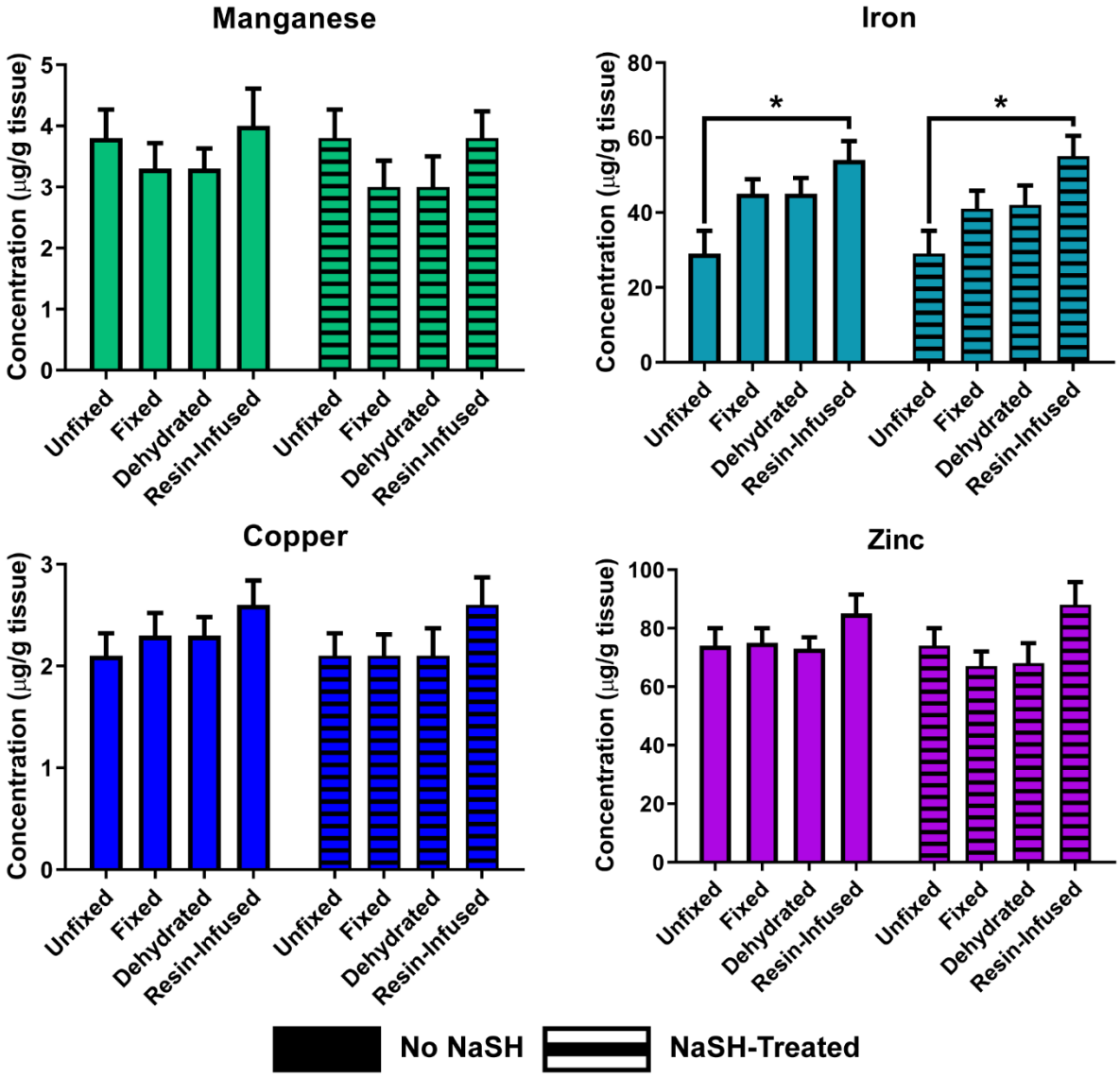

Figure 4.8: Transition metal content of *Xenopus* eggs during sample preparation graphed as g element/g tissue (wet weight). Solid bars: Elemental content of *Xenopus* eggs fixed with formaldehyde and glutaraldehyde. Striped bars: Elemental content of *Xenopus* eggs fixed with formaldehyde, glutaraldehyde, and NaSH. Mean ± SEM, n = 4 frogs. *: 0.05 > p, **: 0.01 > p, ***: 0.001 > p.

In conclusion, our results provide some guidance on which components of fixation reagents can alter metal content in robust samples such as amphibian eggs and more sensitive sections of internal organs. These results should be taken into consideration in the interpretation of

microanalytical studies claiming accurate elemental quantification. These factors should be weighed when quantitative elemental mapping studies are undertaken with a number of emerging methods including X-ray fluorescence microscopy (145), laser ablation ICP-MS (171), secondary ion mass spectrometry (172, 173), and analytical electron microscopy (78) when chemical fixation is required.

Materials and Methods

All animal procedures were approved by the Institutional Animal Care and Use Committee, Northwestern University, and are in accordance with the National Institutes of Health's Guide for the Care and Use of Laboratory Animals.

Xenopus laevis Sample Preparation:

Egg Acquisition. *Xenopus* eggs were obtained via established methods. The jelly coat of the eggs was removed through soaking in a 3% w/v solution of cysteine-HCl, pH 8 for 10 minutes. The eggs were then rinsed in 0.1X Marc's Modified Ringer's buffer (MMR: 10 mM NaCl, 200 μM KCl, 100 μM $MgSO_4$, 200 μM $CaCl_2$, 10 μM EDTA, 500 μM HEPES, pH 7.4). To prepare samples for ICP, 10 eggs were placed in a metal-free conical tube (#89049-170, VWR, Radnor, PA) with a transfer pipet and rinsed 3X with 15 mL H_2O provided by a MilliQ Ultrapure Water System (Millipore, Bedford MA). See Appendix B for calculations on the amount of salts remaining in tubes after washing.

Chemical Fixation Step. For chemical fixation, the majority of the supernatant was removed and 10 mL of fixation solution (2.5% glutaraldehyde, 2% formaldehyde in 0.1 M PIPES buffer, pH 7.4) was added. Eggs were fixed for 36 hours at 4 C. We used 16% paraformaldehyde

(#15710), 25% glutaraldehyde (#16220) and 0.3 M PIPES stock solutions (#11610) from EMS, Hatfield, PA. For the sulfide-containing fixative, 20 mM NaSH (#161527-5G, Sigma-Aldrich, St Louis, MO) from a 1 M stock solution was added before the pH was adjusted. The eggs were washed in 0.1 M PIPES for 10 minutes. 10 eggs were placed in a metal-free conical tube and rinsed 3X with MilliQ H_2O.

Dehydration Procedure. After fixation, the eggs were rinsed for 10 minutes in 0.1 M PIPES and 3 x 5 minutes in diH_2O, followed by dehydration in 30%, 50%, 70%, and 90% ethanol (#15055, EMS, Hatfield, PA) for 15 minutes each, and finally in pure ethanol for 2 x 10 minutes. 10 dehydrated eggs were placed in metal-free conical tubes.

Resin Infusion. After dehydration, eggs were placed in a 1:1 ethanol: Embed 812 resin (#14120, EMS, Hatfield, PA) solution overnight. The next morning, the mixture was removed and replaced with pure resin for 2 hours. The eggs were placed on filter paper to wick off excess resin and then 10 eggs were placed in metal-free conical tubes.

ICP Sample Preparation. Following sample collection, eggs were dried overnight at 70 C. Eggs were then dissolved overnight at 70 C in 450 µL 67-70% trace-metal free nitric acid (#NX0407, Supelco, Burlington, MA). The solution was diluted to 15 mL with MilliQ H_2O for a final concentration of 3% HNO_3.

Murine Ovary Sample Preparation:

Ovary Acquisition. CD-1 mice purchased from Envigo, Indianapolis, IN, were housed and bred in a barrier facility within Northwestern University's Center for Comparative Medicine. Mice were provided with food and water *ad libitum* and kept in a 14 hour light, 10 hour dark cycle

with constant temperature and humidity. 40 ovaries were dissected from 12-week-old female mice. The mice were not perfused before sacrifice.

Sample Preparation. The ovaries were fixed in the following solutions at 4 C for 12 hours: 4% formaldehyde, modified Davidson's Fixative (14% denatured ethanol, 37.5% formalin, 6.25% glacial acetic acid in dH_2O – #64133-50 EMS), as well as the glutaraldehyde/formaldehyde fixative described above in the *Xenopus* section, both with and without NaSH. After fixation, the ovaries were rinsed three times in 70% ethanol (#2701, Decon Labs, King of Prussia, PA) for 5 minutes each. Each ovary was then transferred to one 15 mL metal-free centrifuge tube for digestion. Samples were digested in 150 µL 69% nitric acid (#84385, Honeywell Fluka, Charlotte, NC) with 40 µL 30% hydrogen peroxide (#16911, MilliporeSigma, Burlington, MA) at 60 C for at least 16 hours. 4,810 µL MilliQ H_2O was then added to produce a final solution in a total sample volume of 5 mL.

Solution Sample Preparation:

The elemental content of the starting materials, fixative solutions and reagents were determined by ICP-MS after digestion in nitric acid. 67-70% trace-metal free nitric acid (#NX0407, Supelco, Burlington, MA) was added to deionized water from the Northwestern University taps (used to make the fixative solutions), in metal-free tubes at a final concentration of 3%. Samples of >99.9% Ethanol (#15055, EMS), formaldehyde (#15710 EMS), modified Davidson's Fixative (#64133-50 EMS), and the aldehyde-containing fixation solutions, with and without NaSH, were heated to dryness in metal-free tubes at 70 C. HNO_3 was added and the residue was dissolved for at least 5 hours. MilliQ H_2O was added to dilute the acid to a final concentration of 3%.

Samples of glutaraldehyde and Embed 812 were digested by microwave because they polymerized after drying or after acid digestion at 70 C. 500 mg of Embed 812 was placed in 4 mL of a 1:1 low trace metal HNO_3:H_2O_2 solution (HNO_3, #A509-P212, Thermo Fisher, Waltham, MA; H_2O_2, #11782, GFS, Columbus, Ohio) and 1 g of glutaraldehyde was treated similarly. The samples were then microwaved for 40 minutes at 220 C with a 20 minute ramp and 30 minute exhaust in a Milestone EthosEZ Microwave Digestion System **(**Quantitative Bio-element Imaging Center, Northwestern University). The digested samples were then diluted with MilliQ H_2O to give approximate final dilutions of 1:50 for Embed 812 and 1:35 for the glutaraldehyde. The densities of the fixative solutions were assumed to be 1 g/mL.

ICP-MS and ICP-OES:

Analysis. ICP elemental standards were obtained from Inorganic Ventures (Christiansburg, Virginia). Samples were analyzed using a Thermo Scientific iCAP 7600 ICP-OES and a Thermo iCAP Q ICP-MS (both Quantitative Bio-element Imaging Center, Northwestern University). In order to calculate the molarity of the *Xenopus* eggs, their average volume was assumed to be 1 μL. (174) Figures 4.7 and 4.8 were graphed using an average wet weight of 1.71 mg/egg. (164)

Mouse ovary samples were first analyzed by ICP-MS. Because of the small sample volumes, they were then further diluted 3-fold and analyzed by ICP-OES.

***Xenopus* Statistics.** Two sample groups were compared: eggs fixed with aldehydes and eggs fixed with aldehydes and sodium sulfide. For each sample group, eggs were taken from 4 separate frogs. For each frog we compared unfixed eggs to 3 different treatment conditions: 1. fixed eggs, 2. fixed and dehydrated in an ascending ethanol series as described above, and 3. resin-

infused eggs. There were 3-5 sample tubes per frog per treatment group. Q-tests on technical replicates removed outliers ($\alpha = 0.05$; 4 out of 1150 measurements were removed). Technical replicates were averaged in order to obtain biological replicates. Two-tailed, heteroscedastic T-tests were run between treatment groups in order to determine significant differences between fixation steps.

Murine Statistics. Each datapoint in each condition represents the average elemental content of 8 different ovaries. Outliers were removed by Dixson's Q-test ($\alpha = 0.05$; 10 out of 400 measurements were removed). Statistical analysis was carried out by Student's T-test (as described above) comparing the unfixed control to each experimental group.

Scanning Transmission Electron Microscopy Energy Dispersive X-Ray Spectroscopy:

For STEM-EDS analysis, samples were chemically fixed, dehydrated with ethanol, and infiltrated with resin as described above. Infiltrated *Xenopus* eggs were transferred into fresh resin in silicon molds and polymerized at 65 C for 24 hours. Sections with a nominal thickness of 200 nm were generated with an ultramicrotome (Ultracut-S, Leica Microsystems, Wetzlar, Germany) and placed on Formvar/carbon coated slot grids (#FCF2010, EMS, Hatfield, PA). STEM-EDS analysis was performed with a HD2300 STEM (Hitachi High-Technologies Corporation, Ibaraki, Japan) equipped with a Dual-EDS system and NSS software (Thermo Electron North America LLC, Madison, WI). The STEM was operated at 200 kV acceleration voltage.

Chapter 5: General Discussion

Summary and Significance of Findings

Xenopus

In my second chapter, I demonstrate that the zinc spark occurs in *Xenopus* and that a decrease in accessible intracellular zinc content leads to anaphase II entry. The majority of intracellular manganese leaves the embryo following fertilization. The manganese is mostly bound to a low molecular weight carboxylate in both the egg and embryo. The zinc and manganese, along with calcium and additional transition metals, are stored in cortical vesicles, most of which disappear following fertilization. Finally, both extracellular zinc and manganese act as blocks to fertilization.

When I started my research, meiotic zinc dynamics had been studied in different mammalian species (4, 7, 15, 16), but it was unknown if they were conserved in different classes of animals. Fertilization has been studied in *Xenopus* since the frogs' original use as a pregnancy test in the first half of the twentieth century (175). We decided to use *Xenopus* eggs because their development is well characterized and because of their large size, which allowed for a new suite of experimental techniques that were impractical for mammalian eggs. Although the metal content of *Xenopus* oocytes (40) and eggs (Table 4.2) had previously been measured, no one had detected differences in zinc and manganese content post-fertilization.

This is the first time that a zinc release and the necessity of a drop in accessible zinc has been shown to occur in a different class of animal (note that since starting my thesis project multiple groups have published on the conservation of zinc fluxes in different organisms). (17-20) Amphibians were the first tetrapod lineage to evolutionarily diverge, approximately 340 million years ago (176), so the zinc regulation of meiosis is a truly ancient phenomenon. It is interesting

that the zinc efflux is conserved in both internal and external fertilizers as well as terrestrial and aquatic species. The efflux would seem more likely to occur in internal fertilizers, as the environment surrounding the egg would be more controlled. Since *Xenopus* eggs are laid in water, it is likely that the zinc affects the vitelline envelope (similar to mice), as zinc diffuses in an aqueous environment, suggesting that the concentration would be too low to directly interact with sperm.

Interspecies Comparisons

There are some significant differences in meiotic metal fluxes between amphibians and mammals. In mouse eggs, there are more zinc-containing vesicles in the vegetal pole (VP) than in the animal pole (AP). (6) In contrast, I have found significantly more metal-containing vesicles in the AP than the VP in *Xenopus*. The AP is the site of sperm entry in *Xenopus*, as it contains the maternal DNA. Therefore, the greater concentration of vesicles in the AP could act as a block to polyspermy. Sperm entry is more likely to occur in the VP of the mouse egg than the AP, though fertilization occurs successfully after entry into either pole. (177) It is possible that the preponderance of cortical granules (CGs) in the mouse VP correlates with the propensity of sperm entry point, but since the diameter of a mouse egg is only 6% that of a *Xenopus* egg, zinc is able to diffuse quickly even if sperm enters the AP.

Proportionally less zinc is released from *Xenopus* eggs than mouse eggs. Mouse eggs lose 20% of their intracellular zinc following fertilization (4, 6), while I was unable to measure the drop in zinc from *Xenopus* eggs via ICP-MS. Since 90% of total intracellular zinc is stored in yolk platelets (43), less than 10% would be available for release. There are a few possible reasons for why frog embryos would release less zinc than murine embryos do. First, the difference may be a result of simple geometry. The diameter of a *Xenopus* egg is about 15x that of a murine egg. As a

result, the volume of the frog egg is 4000x greater, while the surface area is only 250x greater. If the *Xenopus* egg releases the same density of zinc per unit of surface area as a mouse egg, proportionally only 1/16 as much zinc would need be released. Second, frog eggs can be considered "closed systems", as they contain all the nutrients required for a developing embryo, while mammalian eggs take in nutrients from the mother's womb (40). Late stage (Dumont stage V and VI) oocytes and eggs do not acquire or lose ions to the solution that they are in, including when their jelly coats are removed. This because *Xenopus* eggs are laid in ponds, which are hypotonic environments. (91, 161, 163) The frog may have evolved to release less zinc than mammals, as it is impractical to take in zinc from pond water.

Zinc acts as a block to polyspermy in both *Xenopus* and mammals. According to my 1,10-phenanthroline (OP) chelation experiment, changes in accessible zinc levels are necessary for anaphase II entry in *Xenopus*, which is similar to mammalian eggs. (5, 7) Unlike mouse eggs, there is no zinc influx post-fertilization in *Xenopus*, so it is probable that the concentration of zinc in the cytosol is altered through a rearrangement of intracellular zinc binding and storage.

The concentration of zinc stored within *Xenopus* cortical vesicles (20 mM) is an order of magnitude lower than that of mouse (200 mM). (6) Even after summing the concentrations of the different transition metals in the *Xenopus* vesicles and assuming that my concentration calculations are underestimates, the concentrations in the mouse CGs are still around 5-fold higher. However, the volume of a *Xenopus* vesicle is around 7X that of mouse, so the absolute amount of metal contained in the two species' CGs are similar, and because there are probably interspecies differences in the amount of metal needed to be released in order to block polyspermy, differences in CG metal concentration are to be expected.

Manganese and Intravesicular Metals

I discovered a drop in intracellular manganese content following fertilization when performing ICP-MS experiments. This was serendipitous – I analyzed the changes in the contents of other transition metals besides zinc, expecting them to remain similar in both eggs and embryos. Neither the biological roles of manganese nor its subcellular localization are well known. (178) Manganese is primarily considered to be a protein cofactor. Studies in humans have focused on the metal's role in neurological disease. Elevated levels – either from workplace exposure or mutated transport proteins – lead to Parkinson's-like systems. (105, 178) Although there is currently no evidence that meiotic manganese fluxes play a regulatory role like zinc fluxes do, extracellular manganese blocks polyspermy. Further experiments will be needed to determine the mechanics of this block and if the manganese efflux is conserved in different classes of animal.

Besides zinc and manganese, I found that calcium and multiple transition metals are stored in cortical vesicles in *Xenopus* at low millimolar concentrations. Through analysis of transmission electron microscopy images, the majority of electron-dense vesicles disappear following fertilization, suggesting that in addition to zinc and manganese calcium, copper, cobalt, and nickel leave the egg as well. There are three possibilities for why the vesicles contain multiple metals: First, the metals could act in addition to zinc and manganese as blocks to fertilization. Extracellular cobalt, nickel, and copper block polyspermy (see below). (17) Second, the egg could put metals in the vesicles as a detoxification method if concentrations are too high. Elevated levels of cytosolic transition metals would affect cellular homeostasis and can be genotoxic. Third, the vesicles could contain advantageous metal transporters that load the other metals in addition to zinc and manganese. Because nickel is contained in the vesicles but has no biological function in the frog or any other vertebrate species, the first option is not likely. A combination of the second and third

possibilities is probably true – the egg maintains metal homeostasis through a combination of binding to proteins, peptides, and cofactors as well as through transport. Assuming that the vesicles are loaded with metal through transporters, it is possible that if cytosolic concentrations of metals besides zinc and manganese are above homeostatic levels the metals will be available to be loaded into the vesicles through promiscuous transporters.

Since the first discovery of zinc sparks in mouse, Zn(II)'s anion has been unknown. Intracellular zinc is usually bound to proteins; however zinc involved in neurotransmission colocalizes with glutamate in certain synaptic vesicles. (2) Although we did not discover the exact anion of the metals in *Xenopus* cortical vesicles, we have narrowed down the possibilities of what it can be. Using multiple electronic paramagnetic resonance (EPR) methods, we found that the majority of manganese is bound to a low molecular weight carboxylate. This suggests that the manganese ion itself somehow functions as a block to polyspermy, rather than serving in its expected role as a cofactor to a protein that would alter the vitelline envelope, jelly coat, or the sperm itself. We can assume that the other metal ions in the small cortical vesicles will be coordinated to the same chemical as manganese, so this provides further directions of study.

Corroborating Reports of Zinc Sparks

Two intriguing papers reported corroborating results on zinc sparks in amphibian and fish eggs as my Nature Chemistry paper was finishing review. Zinc sparks occur following fertilization in zebrafish (*D. rerio*) eggs following fertilization. (17, 18) Zinc is stored in cortical vesicles in metaphase II eggs and a calcium wave proceeds zinc release from the vesicles. The zinc transporter ZIP9 is necessary for proper zinc modulation; cortical vesicles do not develop properly in $zip9^{-/-}$ eggs and they release less zinc than wild type eggs. (18) ZIP6 and ZIP10 are necessary for proper mammalian oocyte meiosis and their localization is enhanced in the oocyte cortex (11), so this

report demonstrates that the necessity of the ZIP family for meiotic progress is evolutionarily conserved in vertebrates.

While my paper was in review, another group published their results on the zinc spark in *Xenopus*. (17) There are some similarities between the two papers, though we diverged in our research directions. Wozniak *et al.* determined the amount of zinc released from the egg via both fluorimetry and ICP-MS of the buffer post-activation and -fertilization. Around $10^{12} – 10^{13}$ zinc atoms per egg are released, corresponding to 1 – 10% of total intracellular zinc. This is expected, as 90% of the zinc is tightly stored in yolk platelets. Using the standard deviations for my ICP measurements of eggs and embryos, at $p = 0.05$ I would have been able to detect around a 20% difference between the two groups, so Woznaik *et al.*'s data do not contradict mine. In another experiment, Wozniak *et al.* determined that extracellular zinc does not alter the jelly coat of the egg, although the jelly does slow the diffusion of zinc away from the egg. This study claims that the zinc alters a protein or receptor to prevent polyspermy, which is possible, but does not provide further evidence to back this claim.

We both tested whether extracellular $ZnSO_4$ blocks fertilization. Coincidentally, we both pre-incubated eggs for 15 minutes in zinc-containing buffer, though Wozniak *et al.* then washed the eggs and fertilized them whereas I fertilized and incubated them in zinc-containing buffer. We calculated similar IC_{50} values: I obtained 53 μM (95% CI = 47 - 61 μM) $ZnSO_4$, whereas they obtained 31 ± 10 μM (± SEM). Additionally, we both tested the effects on fertilization of different extracellular metals. Wozniak *et al.* found that $CuCl_2$ (IC_{50} = 9.1 ± 3.0 μM), $NiCl_2$ (IC_{50} = 224 ± 23 μM), and $CoCl_2$ (IC_{50} = 971 ± 92 μM) can all block fertilization, though unlike me they did not test manganese. Their data suggest that the copper, cobalt, and nickel I see stored in the cortical vesicles could be playing a role in the block to fertilization. Wozniak *et al.* did not evaluate the

presence of or changes in manganese, nor did they address any questions of intracellular metal localization, focusing in the rest of the paper on the role of zinc in the fertilization of other lower organisms.

There are two sections in which Wozniak *et al.* do not fully follow through with their experiments. First, they attempted to see if *Xenopus* eggs can be parthenogenetically activated via zinc chelation and state that they cannot. However, they only incubated the eggs in 1.5 mM N,N,N′,N′-Tetrakis(2-pyridylmethyl)ethylenediamine (TPEN), which I found to be insufficient. In my experiments, 3 mM TPEN (the highest concentration that can be dissolved in aqueous buffer) was unable to activate eggs. However, 10 mM OP, a metal chelator that binds zinc two orders of magnitude more tightly than TPEN (179, 180), was able to activate them. Second, while Wozniak *et al.* conclude that zinc is released from *Xenopus* CGs and then acts as a block to fertilization it appears that their argument is based on the assumption of interspecies similarity: they do not actually show that *Xenopus* CGs contain zinc and, at the time of the publication of their paper, neither had any other research group.

Overall, Converse and Thomas' and Wozniak *et al.*'s studies corroborate my findings that zinc fluxes are conserved throughout Chordata. Wozniak *et al.*'s results are in accord with mine when there was overlap between our experiments. Although Wozniak *et al.* did not perform experiments to determine if there is a zinc efflux in the invertebrate species they studied, their results add to the evidence that zinc plays a role in the fertilization of at least some invertebrates.

My *Xenopus* results provide evidence that zinc is a meiotic regulatory factor. Since I found that the decrease in zinc post-fertilization is necessary for entry into anaphase II, differing zinc levels are necessary for meiotic progress. Since the phenomenon has been conserved for hundreds

of millions of years, it would not be surprising that it serves a regulatory role, which we hypothesize governs the function of the protein EMI2.

EMI2

In my third chapter, I studied the zinc-binding affinities of the spindle checkpoint protein EMI2. I first described the changes made to the purification process and competitive chelation experiments in order to obtain non-oxidized protein and good titration data. I then used competitive chelation experiments to calculate the affinities of EMI2's two zinc binding sites, demonstrating that one site binds zinc five orders of magnitude tighter than the other. Finally, using high-energy-resolution fluorescence detection (HERFD) spectroscopy, the binding site containing four cysteines was found to have the higher zinc-binding affinity.

The difference in affinities for three RING proteins have been determined and all have a difference of two orders of magnitude between their two binding sites. (58, 125, 126) According to my competitive chelation results, there is an approximately 420,000-fold difference in the zinc-binding affinities of EMI2's two binding sites. This therefore suggests that one site in EMI2 could be structural while the other could be regulatory. Additionally, one of EMI2's binding sites binds zinc tighter than previously studied RING proteins do. The exact affinities for two of the proteins were calculated via cobalt binding. Because it is a soft metal with a similar ionic radius, cobalt mimics zinc binding, though around 3-4 orders of magnitude less tightly. (181) The zinc-binding affinities of the RING proteins are therefore between 10^{-9} – 10^{-12} M (58, 125), similar to EMI2's second site but significantly weaker than the first. Although *in vitro*/*in vivo* experiments are necessary to establish if differential zinc binding regulates EMI2 inhibition of the APC/C (vide infra), these initial experiments suggest that it is possible.

The HERFD experiment demonstrates that EMI2's C_4 site binds zinc more tightly than the C_3H site. Both previously-studied RING proteins showed similar results (58, 125) – however, this cannot be viewed as a trend. Short, engineered zinc finger peptides have mixed results on whether C_4 or C_3H binds tighter. (120, 127, 181) In natural proteins, variation in zinc finger binding affinity is over 7 orders of magnitude (120, 128), with both C_4 and C_3H sites demonstrating a wide range of affinities. (128) There are several biophysical reasons for this. Cysteine's thiolate domain binds Zn(II) tighter than histidine's imidazole domain does, though at physiological pH this effect is negated because of proton competition for the cysteine. (127) Additionally, protein structure will affect thiol acidity. (128) The physical properties of non-binding amino acids in the coordination sphere will affect binding (128); the second coordination sphere can affect the binding affinity of a zinc finger based on properties such as hydrophilicity/-phobicity of amino acids and hydrogen bonding. By itself, the hydrophobicity of amino acids surrounding the binding pocket can alter binding by up to four orders of magnitude. (120) In sum, the identification of EMI2's C_4 site as the strong-binding site does not accord with a trend, but rather will allow further experimentation to focus on how the structure of the protein changes as zinc fills the C_3H site.

Structurally, it is logical that the C_4 site has the tighter binding affinity. Residues 618-641 are disordered (Figure 5.1) (57), meaning that the C_3H site has fewer secondary structural elements near it. C-terminal constructs of EMI2 are sufficient to inhibit the APC/C, with the RL tail (the last two amino acids – 640 and 641 in mouse) binding to ANAPC2. (57) Zinc binding in the C_3H site could provide enough structure to the C-terminus in order to allow for its interaction with and inhibition of the APC/C.

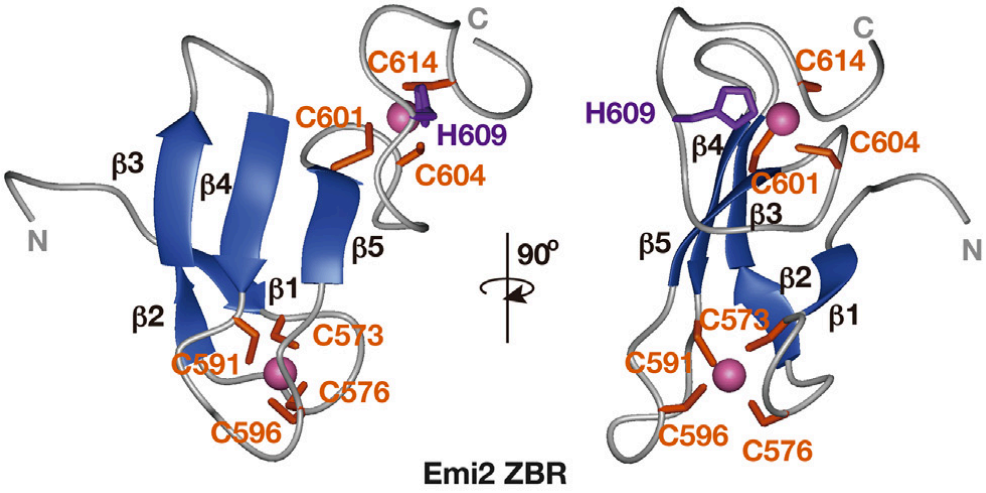

Figure 5.1: NMR structure of EMI2's zinc-binding region. From (57).

It is possible that zinc, rather than an alkali or alkaline earth metal, acts as a regulatory agent during meiosis because its interactions can be more controlled. Ions (Na^+ and K^+) in the cytoplasm do not bind tightly to proteins and are at concentrations around one to three orders of magnitude higher than those of transition metals. Neuronal action potential – the most well-known ionic regulatory process – is based on large changes in ion concentration, leading to intra- and extracellular charge differentials. On the other hand, zinc and other transition metals are held in homeostasis through tight binding, for example with a calculated average of less than one free Zn^{2+} ion per *E. coli* cell. (165) Therefore, smaller relative and absolute changes in the concentration of Zn^{2+} compared to Na^+ or K^+ would be necessary for an intracellular effect and would affect a smaller number of binding moieties than the latter two ions.

A proposed method of EMI2 regulation is as follows: EMI2 is expressed during anaphase I. With an affinity of 10^{-15} M, the C_4 binding site is tighter than the majority of intracellular proteins and is immediately filled with zinc. As zinc levels increase and other zinc-binding moieties in the egg are filled, the C_3H (weak) binding site fills with zinc, altering the structure of the protein.

Because the C_3H site is proximal to the disordered C-terminus, the major structural changes probably occur in that binding site's vicinity. EMI2 then fully inhibits the APC/C. As intracellular zinc levels decrease following fertilization, other zinc-binding moieties with affinities greater than 10^{-10} M are now apo, causing the C_3H site to lose its Zn^{2+} ion. This then alters EMI2's structure, freeing it from the APC/C. EMI2 is degraded by the pathways described in the Introduction, which are probably at least partially independent of EMI2's change in structure. Future experiments, particularly NMR of EMI2 and the APC/C at different levels of zinc occupancy, will demonstrate the validity of this hypothesis.

Understanding the molecular mechanisms controlling the cell cycle may identify new specific targets for chemotherapeutics. Cancer is characterized by dysregulated cell division as well as chromosomal abnormalities (aneuploidy, etc.). EMI1 and EMI2 play vital roles in assuring proper chromosome division. As a mitotic protein, EMI1 has been found to play a role in cancer. For example, overexpression of EMI1 and APC/C substrates positively correlates with tumor malignancy (182); patients with ovarian clear cell carcinoma and esophageal squamous cell carcinoma who overexpress EMI1 have poorer prognoses compared to those who do not. (183, 184) EMI overexpression in $p53^{-/-}$ cells leads to aneuploidy and chromosomal rearrangements. (185) The HPV16 E7 oncoprotein of the human papilloma virus inhibits $SCF\beta^{TrCP}$-mediated EMI1 ubiquitylation, leading to mitotic abnormalities. (186) Knocking down EMI1 with siRNA in cancer cell lines improves the efficacity of doxorubicin and radiotherapy. (187) Understanding the metalloregulation of these checkpoint proteins will provide more information about their dysregulation and could hopefully lead to medical applications.

My inorganic approach to developmental research provides more information about transition metals in oocyte maturation, fertilization, and early embryonic development. Most

biologists consider transition metals to serve as cofactors, i.e. structural elements, or at high levels as environmental toxins spread primarily through anthropogenic activity. Although these are two major biological roles, my research in these two chapters concludes that transition metal ions act as biological agents themselves. In my *Xenopus* research, zinc and manganese ions which are not bound to proteins act as blocks to polyspermy. In the EMI2 project, zinc binds to the protein, but rather than being a static structural element, hypothesized changes in zinc occupancy lead to dramatic cellular effects. Just as new types and roles of RNA have been discovered in the past decades, my results will hopefully spur further interest into the study of transition metals' varied roles.

Sulfide Fixation

In my fourth chapter, I studied the effects of a modified form of Timm's sulfide fixation method on elemental content and localization in *Xenopus* eggs. Using a stepwise analysis of the fixation through resin-infusion process, I found that the majority of elemental change occurs during the fixation step. Surprisingly, besides iron contamination, there was no difference in the content or localization of transition metals in eggs fixed with or without sulfide. The egg results were compared with those of mouse ovaries, which show greater elemental change following fixation, though there was a much greater loss of small, mobile ions than of transition metals.

This was the first experiment in which bulk elemental content was measured after sulfide fixation – previous work focused merely on maintaining and/or enhancing metal localization post-fixation. There was no significant difference in transition metal content between the control and sulfide-treated eggs. Although iron was the only transition metal to be completely preserved in the ovaries, the other three had at most a 30% loss following fixation. This is less significant than the

drops in potassium, magnesium, and calcium, suggesting that the sulfide and/or binding environment of the transition metals served to preserve them.

One of the major findings of the chapter, confirming previous work (146), is that post-fixation elemental content strongly depends on the tissue type being analyzed. Although small mobile ions like K^+ will almost always be lost during the fixation process, transition metal retention varies. In our lab's previous experiments with mouse eggs, fixing without sulfide led to zinc loss from the CGs. (6) In comparison, fixing *Xenopus* eggs with aldehydes but without sulfide does not alter either bulk transition metal content or localization (except for a gain in iron due to contaminants in the solution). This could be due to two reasons: First, as stated above, *Xenopus* eggs are laid in pond water and are therefore impermeable to ion losses, so their membranes may be tougher than those of mammalian cells, leading to less aldehyde permeabilization. Second, and more likely, transition metals are bound extremely tightly inside the eggs. Most transition metals are tightly bound by proteins or inside organelles. In *Xenopus* eggs metals are localized in the yolk platelets and small cortical vesicles and may be more tightly bound than zinc is in murine CGs.

Although the addition of sulfide neither significantly affected the transition metal content of *Xenopus* eggs nor their cortical localization, and was only partially successful in mouse ovaries, I would still recommend its use when trying to image transition metals. It was necessary for imaging mouse eggs as well as a variety of tissue types imaged by different groups. (86, 90) The only disadvantage of sulfide fixation is that it increases intratissue sulfur content, with the majority of sulfide binding to biopolymers instead of metals. However, most researchers probably do not need to concurrently map both sulfur and transition metal contents, so this should not be a problem.

None of the four fixation methods used for mouse ovaries were able to accurately preserve transition metal contents. In comparison to frog eggs, the ovary is a multicellular, excised tissue

containing blood and other fluids. There will therefore be elemental loss from fluids and the cells will be more permeable than frog eggs. There are a couple possible ways to improve the fixation procedure for the mouse ovaries. First, rather than chemically fix the entire ovary, a small piece of the ovary could be excised and then frozen or freeze-dried it. Although dissection will always lead to some elemental loss, a frozen-hydrated or dried sample will avoid the major elemental loss caused by chemical permeabilization. Second, if one is interested in the elemental content/distribution of a certain cell type, they can be cultured. Cultured cells are easier to freeze and image than tissue. The disadvantage of imaging cultured tissue is that the growth conditions in an incubator are different than in an organism, so elemental content and distribution may differ. Additionally, if immortalized cells are used, they could contain mutations that alter their elemental content.

An additional finding of this paper is that the solutions used in the fixation and resin-infusion process can contain enough metal contamination to affect experimental results, which few previous researchers have taken into account. Except for hyperaccumulators (72), biological transition metal concentrations range from the low micromolar to the low millimolar. Therefore, according to my results, a fixative containing a transition metal at an order of magnitude less than that of the biological sample can lead to detectable contamination. I would recommend that all chemicals be analyzed via ICP before use. ddH_2O or its equivalent should be used instead of diH_2O. The fixatives and embedding resin used in my experiments were microscopy-grade and most contained transition metal content on the micromolar range. Most researchers fix samples in order to study ultrastructure and/or protein distribution rather than elemental localization, so the manufacturer probably does not prioritize minimizing metal content in its chemicals. Instead of using microscopy-grade chemicals, many solutions are available as biological- or HPLC-grade,

both of which should contain lower metal content. For example, Sigma BioReagent-grade formaldehyde is tested to ensure low metal contamination. It contains Na at 100 ppm ≥, K at 20 ppm ≥, Ca at 5 ppm ≥, and transition metals at 1 ppm ≥ (188) meaning that its residual zinc content is an order of magnitude less than that of the EMS formaldehyde I used (Table 4.1).

In sum, when preparing biological samples for elemental mapping experiments it is recommended to optimize the sample preparation procedure before obtaining final data. Poor technique and/or chemicals with high metal contents can lead to improper sample preservation and possibly metal contamination. Performing these control experiments can take some time, but they are necessary for ensuring accurate results. Whenever possible, frozen-hydrated or dried samples should be used (see Chapter 1 for discussion of their advantages). If samples need to be chemically-fixed, fixatives and resins should be checked for metal contamination via ICP. Finally, the ICP results of an unfixed sample should be compared with those of a fixed, resin-infused sample. If there are significant differences in transition metal content between them, the chemical composition of the fixative can be tweaked or a stepwise comparison can be performed to find the step or step(s) in the fixation, dehydration, and resin infusion process that led to the gain or loss of metal, which can then be optimized.

Future Directions

In this section I will discuss new lines of research stemming from my results along with possible experimental approaches.

Future *Xenopus* and Metal Flux Experiments

What is the counter ion to the metal cations in the cortical vesicles? The identity of zinc's binding partner has been unknown since zinc-containing CGs were discovered in mouse eggs a decade ago. In *Xenopus*, EPR has shown that most manganese is bound to a low molecular weight carboxylate. We can assume that in a small vesicle the other metals would share the same anion. It is possible that this carboxylate is glutamate, which is the anion of the zinc used in neuronal signaling. (2) *Xenopus* eggs can be sectioned and treated with an anti-glutamate antibody. The cortices will then be imaged for fluorescence. Another way to determine the counter ion would be to artificially activate dejellied eggs in a small volume of buffer. Following CG dehiscence (which is finished within approximately 10 minutes post-activation) the buffer can be collected. Depending on the number of eggs analyzed and the sensitivity of the instrument, a mass spectrometer will be able to determine the identity of the counter ion. Finally, the CGs of frozen mammalian eggs can be analyzed using X-ray absorption near edge structure (XANES) to determine zinc's coordination environment.

How is manganese transported in *Xenopus* oocytes? Zinc is transported into *Xenopus* oocytes through the protein vitellogenin (43) with CG formation occurring over months. (174) Is manganese loaded in a similar manner as zinc? How is manganese sequestered in the vesicles? Although some manganese transporters have been definitely identified, most are promiscuous, and

many are still unknown. (105, 178, 189) SLC39A8 and SLC39A14 are identified as major manganese transporters, though they transport other metals as well. (178) SLC30A10 has been identified in mammals, zebrafish, and nematodes as a specific manganese transporter, or at least a protein whose deletion affects manganese homeostasis but not zinc. (178, 189) All three of these proteins are expressed in *Xenopus*. (190-192) *Xenopus* oocytes at different developmental stages should be probed for these transporters, with specific emphasis on the developing CGs. If there appears to be localization to the CGs, then knockout strains can be created to determine if manganese content/localization decreases.

Is the post-fertilization release of manganese conserved in different classes of animals? It is currently unknown if there is manganese storage and if release occurs from the eggs of other species besides *Xenopus*. Previous X-ray fluorescence microscopy (XFM) analysis of mouse and cow eggs at Argonne used Beamline 2-ID-E and the Bionanoprobe (4, 6, 16), neither of which provide sufficient incident flux for manganese detection, even with extended scan times. The cortices of metaphase II-arrested mammalian eggs can be imaged at Beamline 2-ID-D to provide manganese detection. Additionally, the lab will continue to collaborate with Professor Brian Hoffman to study eggs from different species with EPR. EPR should be able to easily analyze larger eggs such as from sea urchins and zebrafish, though thousands of mammalian eggs would be necessary for a single experiment.

What is the role of manganese in the block to fertilization? In mouse eggs, the zinc spark alters the structure of the zona pellucida, preventing polyspermy. (12) Although I have found that manganese acts as a block to fertilization in *Xenopus*, its mechanism is still unknown. Similar to the mouse experiments, the structure of the vitelline envelope (the name of the extracellular matrix in *Xenopus* equivalent to the zona pellucida in mammals) can be imaged by electron

microscopy both with and without the addition of manganese to determine if the metal alters its structure. The jelly surrounding *Xenopus* eggs consists of glycoconjugates and small proteins (193) and is another possible target of alteration. It is also possible that the manganese interacts directly with the sperm rather than with the zygote. In experiments using murine sperm, increasing Mn^{2+} concentrations lead to decreased sperm galactosyltransferase activity, which leads to decreased sperm-zona pellucida binding. (46) Similar experiments can be performed using *Xenopus* sperm.

Are *Xenopus* cortical vesicles acting as a metal detoxification system? Besides zinc and manganese, I found calcium, copper, nickel, and cobalt in the cortical vesicles. Copper and cobalt have biological functions in vertebrates, while nickel does not. (194) High cytoplasmic levels of these metals would be toxic. Does the *Xenopus* oocyte therefore store these metals in the vesicles as a detoxification system? To confirm this metal localization is not due to this specific group of frogs or the system in which they are held, eggs should be collected from different laboratories as well as from the wild and then be imaged via XFM and/or Analytical Electron Microscopy. Oocytes at different developmental stages can be analyzed as well, with the results additionally providing information on when zinc and manganese enter the CGs. Because of the length of *Xenopus* oogenesis, it would be difficult to limit metal content in food and water. However, it would be much simpler to increase the amount of frogs' metal exposure and then determine if the amount of metal stored in the eggs' cortical vesicles increases. Finally, it is possible that the vesicles are meant to be loaded with zinc and manganese, but promiscuous transporters load them with additional metals as well. Knockdown experiments can determine if this plays a role.

Future EMI2 Experiments

Altering the EMI2^{ZRL} purification protocol. The yield of purified EMI2^{ZRL} is fairly low. The cleavage of the MBP tag is inefficient – it requires a large amount of expensive Factor Xa enzyme. Additionally, Factor Xa often cleaves off-target (195, 196), which leads to a ~6 kDa cleavage product in the EMI2^{ZRL} preps. The EMI2^{ZRL} constructs (wild type and mutant) will be cloned into a pMCSG10 plasmid, which contains a 6x His-GST-TEV leader. (197) Cleaving with the TEV protease should hopefully be more efficient.

How does changing zinc occupancy affect EMI2 function? Although I have shown EMI2's two zinc-binding sites have a five order of magnitude difference in their binding affinities, further experiments are needed to determine whether differential zinc occupancy can regulate EMI2 function. A minimal functional E3 unit of the APC/C can be established using truncated constructs of APC2, APC11, and EMI2 combined with the E1 and E2C enzymes and ubiquitin. The E2C enzyme is auto-ubiquitylated and the amount of ubiquitylation that occurs over a given time can be analyzed using a western blot. (57) If EMI2 inhibits the APC/C, there should be no ubiquitylation. If EMI2 does not inhibit the APC, ubiquitylation should occur while partial inhibition will lead to an intermediate result. Once established, this complex can be exposed to different concentrations of zinc to determine if full zinc occupancy of EMI2 leads to complete inhibition of the APC/C's ubiquitylation function. EMI2 with mutant zinc binding sites can be analyzed as well, with the expectation that they will show partial or no inhibition. (5, 29, 71) Another possible *in vitro* experiment is the creation of *Xenopus* egg extracts in which EMI2^{WT} is immunodepleted and replaced with mutant protein. Defects in spindle assembly can then be analyzed. Because the spindle complex consists of many components, some of which probably

require zinc binding, I would not recommend zinc chelation in CSF extracts because it could have off-target effects.

The function of EMI2 zinc occupancy can be studied *in vivo* as well. Custom antibodies have been designed against EMI2's two zinc binding sites. The antibodies will be microinjected into maturing mouse oocytes as EMI2 begins to be expressed. The proportion of oocytes to reach proper metaphase II arrest will then be measured to determine the effects of blocking each or both of the zinc-binding sites.

Does zinc regulate EMI2 function in sperm? Separate papers have shown that zinc fluxes are necessary for proper sperm function (21) and that EMI2 is necessary for meiosis I in sperm – the protein's role in meiosis II still has not been studied. (70) In order to determine if EMI2 zinc binding plays a role in regulating sperm meiosis, the most straightforward experiment would be to create strains of mice containing EMI2 with different mutations in its zinc-binding region (ZBR). These experiments will demonstrate whether EMI2's ZBR is necessary for proper meiotic progress in sperm and as well as the relative importance and function of the two binding sites.

Does zinc regulate EMI2 in different species? If EMI2 is a zinc-dependent switch in mammals, would it act similarly in *Xenopus* and other vertebrates? The *in vitro* and *in vivo* experiments described above can be repeated with EMI2 and APC/C components and antibodies and oocytes, respectively, from different species. There are definite differences in interspecies zinc fluxes: mouse eggs show a proportionally larger efflux of zinc than *Xenopus* do (possibly because so much of the zinc in a *Xenopus* egg is bound in the yolk) as well as a post-fertilization zinc influx (Seth Garwin, unpublished data), which does not occur in *Xenopus*. It will be interesting to see if and how EMI2 function is conserved.

Do EMI1's two zinc-binding sites have as wide a range of zinc-binding affinities as EMI2's? EMI1 and EMI2 share highly conserved ZBRs (Figure 1.3), so it is possible that the two proteins have similar zinc-binding affinities. Recombinant EMI1 should be expressed and undergo the same competitive chelation experiments as EMI2 to determine its two zinc binding affinities. If EMI1's zinc binding is similar to EMI2's, this would lead to the following question: Do mitotic cells display similar zinc fluxes to meiotic cells? Some studies have shown that zinc levels flux in mitotic cells (22, 23), though because of the difficulty in syncing the cell cycle in cultured cells these should be considered to be initial results that will require follow-up experiments for confirmation.

What are the differences between EMI1 and EMI2 in *Xenopus*? In mammals, EMI2 is only expressed during meiosis, whereas EMI1 is found in all mitotic cells (Figure 1.4). Because the mid-blastula transition (MBT) does not occur until the 13th mitotic cell cycle in *Xenopus*, EMI2 is used in early mitosis. Building off of the above question, does regulation of EMI1 and EMI2 differ in early *Xenopus* mitosis? If *Xenopus* EMI2's regulation is governed by differential zinc occupancy, would there be zinc fluxes in early *Xenopus* mitotic cells? It is possible that zinc is redistributed during early *Xenopus* mitosis. Besides studying the zinc-binding affinities and functionalities of recombinant xEMI1 and xEMI2, slices of pre-MBT embryos at different timepoints can be analyzed using XFM to see if intra- and extra-cellular zinc distribution varies during the mitotic cell cycle.

Summary of Significance

In sum, I have discovered that both zinc and manganese are released from amphibian eggs following fertilization. The metals act as blocks to polyspermy. *Xenopus* eggs contain small

cortical vesicles which store multiple metals in addition to zinc and manganese, possibly acting as a detoxification system. EPR experiments show that the majority of manganese is bound to a low molecular weight carboxylate. These results demonstrate that zinc fluxes are an ancient and conserved meiotic phenomenon while the manganese discovery shows that other transition metal ions have roles besides protein cofactors. Fixation experiments using a modified Timm's method demonstrate that, unlike other tissue types, the addition of sodium sulfide was not necessary for the preservation of transition metal content and localization in *Xenopus* eggs. My results contribute to the evidence that different fixation methods have advantages for different tissue types and that procedural optimizations are recommended before preparing samples for elemental mapping experiments. Finally, I have shown that the meiotic spindle checkpoint protein EMI2 binds two atoms of zinc with a 420,000-fold difference in affinity with the first, C_4 site possessing tighter affinity. If the hypothesis is true, and Zn^{2+} regulates meiotic progress through differential binding to EMI2, this would contribute to the emerging picture that transition metal ions can act as signaling agents.

REFERENCES

1. Klug A. The discovery of zinc fingers and their applications in gene regulation and genome manipulation. Annu Rev Biochem. 2010;79:213-31. Epub 2010/03/03. doi: 10.1146/annurev-biochem-010909-095056. PubMed PMID: 20192761.
2. Toth K. Zinc in neurotransmission. Annu Rev Nutr. 2011;31:139-53. Epub 2011/05/10. doi: 10.1146/annurev-nutr-072610-145218. PubMed PMID: 21548772.
3. Ghazvini Zadeh EH, Huang Z, Xia J, Li D, Davidson HW, Li WH. ZIGIR, a Granule-Specific Zn(2+) Indicator, Reveals Human Islet α Cell Heterogeneity. Cell reports. 2020;32(2):107904. Epub 2020/07/16. doi: 10.1016/j.celrep.2020.107904. PubMed PMID: 32668245; PMCID: PMC7410119.
4. Kim AM, Vogt S, O'Halloran TV, Woodruff TK. Zinc availability regulates exit from meiosis in maturing mammalian oocytes. Nat Chem Biol. 2010;6(9):674-81. Epub 2010/08/10. doi: 10.1038/nchembio.419. PubMed PMID: 20693991; PMCID: PMC2924620.
5. Bernhardt ML, Kong BY, Kim AM, O'Halloran TV, Woodruff TK. A zinc-dependent mechanism regulates meiotic progression in mammalian oocytes. Biol Reprod. 2012;86(4):114. Epub 2012/02/04. doi: 10.1095/biolreprod.111.097253. PubMed PMID: 22302686; PMCID: PMC3338659.
6. Que EL, Bleher R, Duncan FE, Kong BY, Gleber SC, Vogt S, Chen S, Garwin SA, Bayer AR, Dravid VP, Woodruff TK, O'Halloran TV. Quantitative mapping of zinc fluxes in the mammalian egg reveals the origin of fertilization-induced zinc sparks. Nat Chem. 2015;7(2):130-9. Epub 2015/01/24. doi: 10.1038/nchem.2133. PubMed PMID: 25615666; PMCID: PMC4315321.
7. Kim AM, Bernhardt ML, Kong BY, Ahn RW, Vogt S, Woodruff TK, O'Halloran TV. Zinc sparks are triggered by fertilization and facilitate cell cycle resumption in mammalian eggs. ACS Chem Biol. 2011;6(7):716-23. Epub 2011/04/30. doi: 10.1021/cb200084y. PubMed PMID: 21526836; PMCID: PMC3171139.
8. Kong BY, Bernhardt ML, Kim AM, O'Halloran TV, Woodruff TK. Zinc maintains prophase I arrest in mouse oocytes through regulation of the MOS-MAPK pathway. Biol Reprod. 2012;87(1):11, 1-2. Epub 2012/04/28. doi: 10.1095/biolreprod.112.099390. PubMed PMID: 22539682; PMCID: PMC3406555.
9. Tokuhiro K, Dean J. Glycan-Independent Gamete Recognition Triggers Egg Zinc Sparks and ZP2 Cleavage to Prevent Polyspermy. Dev Cell. 2018;46(5):627-40.e5. Epub 2018/08/21. doi: 10.1016/j.devcel.2018.07.020. PubMed PMID: 30122633; PMCID: PMC6549238.
10. Lindsay LL, Wallace MA, Hedrick JL. A hatching enzyme substrate in the Xenopus laevis egg envelope is a high molecular weight ZPA homolog. Dev Growth Differ. 2001;43(3):305-13. Epub 2001/06/26. doi: 10.1046/j.1440-169x.2001.00577.x. PubMed PMID: 11422296.
11. Kong BY, Duncan FE, Que EL, Kim AM, O'Halloran TV, Woodruff TK. Maternally-derived zinc transporters ZIP6 and ZIP10 drive the mammalian oocyte-to-egg transition. Mol Hum Reprod. 2014;20(11):1077-89. Epub 2014/08/22. doi: 10.1093/molehr/gau066. PubMed PMID: 25143461; PMCID: PMC4209882.
12. Que EL, Duncan FE, Bayer AR, Philips SJ, Roth EW, Bleher R, Gleber SC, Vogt S, Woodruff TK, O'Halloran TV. Zinc sparks induce physiochemical changes in the egg zona

pellucida that prevent polyspermy. Integr Biol (Camb). 2017;9(2):135-44. Epub 2017/01/20. doi: 10.1039/c6ib00212a. PubMed PMID: 28102396; PMCID: PMC5439353.
13. Kong BY, Duncan FE, Que EL, Xu Y, Vogt S, O'Halloran TV, Woodruff TK. The inorganic anatomy of the mammalian preimplantation embryo and the requirement of zinc during the first mitotic divisions. Dev Dyn. 2015;244(8):935-47. Epub 2015/04/24. doi: 10.1002/dvdy.24285. PubMed PMID: 25903945; PMCID: PMC4617753.
14. Zhang N, Duncan FE, Que EL, O'Halloran TV, Woodruff TK. The fertilization-induced zinc spark is a novel biomarker of mouse embryo quality and early development. Sci Rep. 2016;6:22772. Epub 2016/03/19. doi: 10.1038/srep22772. PubMed PMID: 26987302; PMCID: PMC4796984.
15. Duncan FE, Que EL, Zhang N, Feinberg EC, O'Halloran TV, Woodruff TK. The zinc spark is an inorganic signature of human egg activation. Sci Rep. 2016;6:24737. Epub 2016/04/27. doi: 10.1038/srep24737. PubMed PMID: 27113677; PMCID: PMC4845039.
16. Que EL, Duncan FE, Lee HC, Hornick JE, Vogt S, Fissore RA, O'Halloran TV, Woodruff TK. Bovine eggs release zinc in response to parthenogenetic and sperm-induced egg activation. Theriogenology. 2019;127:41-8. Epub 2019/01/15. doi: 10.1016/j.theriogenology.2018.12.031. PubMed PMID: 30639695.
17. Wozniak KL, Bainbridge RE, Summerville DW, Tembo M, Phelps WA, Sauer ML, Wisner BW, Czekalski ME, Pasumarthy S, Hanson ML, Linderman MB, Luu CH, Boehm ME, Sanders SM, Buckley KM, Bain DJ, Nicotra ML, Lee MT, Carlson AE. Zinc protection of fertilized eggs is an ancient feature of sexual reproduction in animals. PLoS Biol. 2020;18(7):e3000811. Epub 2020/08/01. doi: 10.1371/journal.pbio.3000811. PubMed PMID: 32735558; PMCID: PMC7423145.
18. Converse A, Thomas P. The zinc transporter ZIP9 (Slc39a9) regulates zinc dynamics essential to egg activation in zebrafish. Sci Rep. 2020;10(1):15673. Epub 2020/09/26. doi: 10.1038/s41598-020-72515-4. PubMed PMID: 32973303; PMCID: PMC7518430.
19. Mendoza AD, Woodruff TK, Wignall SM, O'Halloran TV. Zinc availability during germline development impacts embryo viability in Caenorhabditis elegans. Comp Biochem Physiol C Toxicol Pharmacol. 2017;191:194-202. Epub 2016/09/25. doi: 10.1016/j.cbpc.2016.09.007. PubMed PMID: 27664515; PMCID: PMC5210184.
20. Hu Q, Duncan FE, Nowakowski AB, Antipova OA, Woodruff TK, O'Halloran TV, Wolfner MF. Zinc Dynamics during Drosophila Oocyte Maturation and Egg Activation. iScience. 2020;23(7):101275. Epub 2020/07/03. doi: 10.1016/j.isci.2020.101275. PubMed PMID: 32615472; PMCID: PMC7330606.
21. Kerns K, Zigo M, Drobnis EZ, Sutovsky M, Sutovsky P. Zinc ion flux during mammalian sperm capacitation. Nat Commun. 2018;9(1):2061. Epub 2018/05/29. doi: 10.1038/s41467-018-04523-y. PubMed PMID: 29802294; PMCID: PMC5970269.
22. McRae R, Lai B, Fahrni CJ. Subcellular redistribution and mitotic inheritance of transition metals in proliferating mouse fibroblast cells. Metallomics : integrated biometal science. 2013;5(1):52-61. Epub 2012/12/06. doi: 10.1039/c2mt20176c. PubMed PMID: 23212029; PMCID: PMC3769613.
23. Li Y, Maret W. Transient fluctuations of intracellular zinc ions in cell proliferation. Exp Cell Res. 2009;315(14):2463-70. Epub 2009/05/27. doi: 10.1016/j.yexcr.2009.05.016. PubMed PMID: 19467229.

24. Marvin RG, Wolford JL, Kidd MJ, Murphy S, Ward J, Que EL, Mayer ML, Penner-Hahn JE, Haldar K, O'Halloran TV. Fluxes in "free" and total zinc are essential for progression of intraerythrocytic stages of Plasmodium falciparum. Chem Biol. 2012;19(6):731-41. Epub 2012/06/26. doi: 10.1016/j.chembiol.2012.04.013. PubMed PMID: 22726687; PMCID: PMC3601789.
25. Sun L, Chai Y, Hannigan R, Bhogaraju VK, Machaca K. Zinc regulates the ability of Cdc25C to activate MPF/cdk1. J Cell Physiol. 2007;213(1):98-104. Epub 2007/04/20. doi: 10.1002/jcp.21090. PubMed PMID: 17443687.
26. Schaefer-Ramadan S, Hubrack S, Machaca K. Transition metal dependent regulation of the signal transduction cascade driving oocyte meiosis. J Cell Physiol. 2018;233(4):3164-75. Epub 2017/08/18. doi: 10.1002/jcp.26157. PubMed PMID: 28816348.
27. Bruinsma JJ, Jirakulaporn T, Muslin AJ, Kornfeld K. Zinc ions and cation diffusion facilitator proteins regulate Ras-mediated signaling. Dev Cell. 2002;2(5):567-78. Epub 2002/05/23. doi: 10.1016/s1534-5807(02)00151-x. PubMed PMID: 12015965.
28. Watanabe K, Tokumoto T, Ishikawa K. 1,10-Phenanthroline phosphorylates (activates) MAP kinase in Xenopus oocytes. Cell Signal. 2003;15(12):1139-47. Epub 2003/10/25. doi: 10.1016/s0898-6568(03)00116-5. PubMed PMID: 14575869.
29. Suzuki T, Suzuki E, Yoshida N, Kubo A, Li H, Okuda E, Amanai M, Perry AC. Mouse Emi2 as a distinctive regulatory hub in second meiotic metaphase. Development. 2010;137(19):3281-91. Epub 2010/08/21. doi: 10.1242/dev.052480. PubMed PMID: 20724447; PMCID: PMC2934736.
30. Wallace RA, Misulovin Z, Etkin LD. Full-grown oocytes from Xenopus laevis resume growth when placed in culture. Proc Natl Acad Sci U S A. 1981;78(5):3078-82. Epub 1981/05/01. PubMed PMID: 16593019; PMCID: PMC319503.
31. Lin-Moshier Y, Marchant JS. The Xenopus oocyte: a single-cell model for studying Ca2+ signaling. Cold Spring Harb Protoc. 2013;2013(3). Epub 2013/03/05. doi: 10.1101/pdb.top066308. PubMed PMID: 23457336; PMCID: PMC4017334.
32. Dumont JN. Oogenesis in Xenopus laevis (Daudin). I. Stages of oocyte development in laboratory maintained animals. J Morphol. 1972;136(2):153-79. Epub 1972/02/01. doi: 10.1002/jmor.1051360203. PubMed PMID: 4109871.
33. Nuccitelli R, Yim DL, Smart T. The sperm-induced Ca2+ wave following fertilization of the Xenopus egg requires the production of Ins(1, 4, 5)P3. Dev Biol. 1993;158(1):200-12. Epub 1993/07/01. doi: 10.1006/dbio.1993.1179. PubMed PMID: 7687224.
34. Gillespie PJ, Gambus A, Blow JJ. Preparation and use of Xenopus egg extracts to study DNA replication and chromatin associated proteins. Methods. 2012;57(2):203-13. Epub 2012/04/24. doi: 10.1016/j.ymeth.2012.03.029. PubMed PMID: 22521908; PMCID: PMC3437562.
35. Maresca TJ, Heald R. Methods for studying spindle assembly and chromosome condensation in Xenopus egg extracts. Methods Mol Biol. 2006;322:459-74. Epub 2006/06/03. doi: 10.1007/978-1-59745-000-3_33. PubMed PMID: 16739744.
36. Ohsumi K, Yamamoto TM, Iwabuchi M. Oocyte extracts for the study of meiotic M-M transition. Methods Mol Biol. 2006;322:445-58. Epub 2006/06/03. doi: 10.1007/978-1-59745-000-3_32. PubMed PMID: 16739743.

37. Hannak E, Heald R. Investigating mitotic spindle assembly and function in vitro using Xenopus laevis egg extracts. Nat Protoc. 2006;1(5):2305-14. Epub 2007/04/05. doi: 10.1038/nprot.2006.396. PubMed PMID: 17406472.
38. Session AM, Uno Y, Kwon T, Chapman JA, Toyoda A, Takahashi S, Fukui A, Hikosaka A, Suzuki A, Kondo M, van Heeringen SJ, Quigley I, Heinz S, Ogino H, Ochi H, Hellsten U, Lyons JB, Simakov O, Putnam N, Stites J, Kuroki Y, Tanaka T, Michiue T, Watanabe M, Bogdanovic O, Lister R, Georgiou G, Paranjpe SS, van Kruijsbergen I, Shu S, Carlson J, Kinoshita T, Ohta Y, Mawaribuchi S, Jenkins J, Grimwood J, Schmutz J, Mitros T, Mozaffari SV, Suzuki Y, Haramoto Y, Yamamoto TS, Takagi C, Heald R, Miller K, Haudenschild C, Kitzman J, Nakayama T, Izutsu Y, Robert J, Fortriede J, Burns K, Lotay V, Karimi K, Yasuoka Y, Dichmann DS, Flajnik MF, Houston DW, Shendure J, DuPasquier L, Vize PD, Zorn AM, Ito M, Marcotte EM, Wallingford JB, Ito Y, Asashima M, Ueno N, Matsuda Y, Veenstra GJ, Fujiyama A, Harland RM, Taira M, Rokhsar DS. Genome evolution in the allotetraploid frog Xenopus laevis. Nature. 2016;538(7625):336-43. Epub 2016/10/21. doi: 10.1038/nature19840. PubMed PMID: 27762356; PMCID: PMC5313049.
39. Wang F, Shi Z, Cui Y, Guo X, Shi Y-B, Chen Y. Targeted gene disruption in Xenopus laevis using CRISPR/Cas9. Cell & Bioscience. 2015;5(1):15. doi: 10.1186/s13578-015-0006-1.
40. Nomizu T, Falchuk KH, Vallee BL. Zinc, iron, and copper contents of Xenopus laevis oocytes and embryos. Mol Reprod Dev. 1993;36(4):419-23. Epub 1993/12/01. doi: 10.1002/mrd.1080360403. PubMed PMID: 8305203.
41. Falchuk KH, Montorzi M, Vallee BL. Zinc uptake and distribution in Xenopus laevis oocytes and embryos. Biochemistry. 1995;34(50):16524-31. Epub 1995/12/19. PubMed PMID: 8845382.
42. Montorzi M, Falchuk KH, Vallee BL. Vitellogenin and lipovitellin: zinc proteins of Xenopus laevis oocytes. Biochemistry. 1995;34(34):10851-8. Epub 1995/08/29. doi: 10.1021/bi00034a018. PubMed PMID: 7662665.
43. Falchuk KH, Montorzi M. Zinc physiology and biochemistry in oocytes and embryos. Biometals. 2001;14(3-4):385-95. Epub 2002/02/08. PubMed PMID: 11831467.
44. Eriksson SP. Variations of manganese in the eggs of the Norway lobster, Nephrops norvegicus (L.). Aquat Toxicol. 2000;48(2-3):291-5. Epub 2001/02/07. doi: 10.1016/s0166-445x(99)00034-x. PubMed PMID: 10686333.
45. Michibata H, Hori R. The accumulation of manganese from the environmental medium by the egg of Oryzias latipes. J Cell Physiol. 1979;98(1):241-3. Epub 1979/01/01. doi: 10.1002/jcp.1040980126. PubMed PMID: 762199.
46. Benau DA, McGuire EJ, Storey BT. Further characterization of the mouse sperm surface zona-binding site with galactosyltransferase activity. Mol Reprod Dev. 1990;25(4):393-9. Epub 1990/04/01. doi: 10.1002/mrd.1080250413. PubMed PMID: 2109619.
47. Sivakumar S, Gorbsky GJ. Spatiotemporal regulation of the anaphase-promoting complex in mitosis. Nat Rev Mol Cell Biol. 2015;16(2):82-94. Epub 2015/01/22. doi: 10.1038/nrm3934. PubMed PMID: 25604195; PMCID: PMC4386896.
48. Sobinoff AP, Sutherland JM, McLaughlin EA. Intracellular signalling during female gametogenesis. Mol Hum Reprod. 2013;19(5):265-78. Epub 2012/12/19. doi: 10.1093/molehr/gas065. PubMed PMID: 23247812.

49. Wu JQ, Kornbluth S. Across the meiotic divide - CSF activity in the post-Emi2/XErp1 era. J Cell Sci. 2008;121(Pt 21):3509-14. Epub 2008/10/24. doi: 10.1242/jcs.036855. PubMed PMID: 18946022.
50. Heber-Katz E, Zhang Y, Bedelbaeva K, Song F, Chen X, Stocum DL. Cell cycle regulation and regeneration. Curr Top Microbiol Immunol. 2013;367:253-76. Epub 2012/12/25. doi: 10.1007/82_2012_294. PubMed PMID: 23263201.
51. Chang L, Zhang Z, Yang J, McLaughlin SH, Barford D. Atomic structure of the APC/C and its mechanism of protein ubiquitination. Nature. 2015;522(7557):450-4. Epub 2015/06/18. doi: 10.1038/nature14471. PubMed PMID: 26083744; PMCID: PMC4608048.
52. Reimann JD, Freed E, Hsu JY, Kramer ER, Peters JM, Jackson PK. Emi1 is a mitotic regulator that interacts with Cdc20 and inhibits the anaphase promoting complex. Cell. 2001;105(5):645-55. Epub 2001/06/08. PubMed PMID: 11389834.
53. Reimann JD, Gardner BE, Margottin-Goguet F, Jackson PK. Emi1 regulates the anaphase-promoting complex by a different mechanism than Mad2 proteins. Genes Dev. 2001;15(24):3278-85. Epub 2001/12/26. doi: 10.1101/gad.945701. PubMed PMID: 11751633; PMCID: PMC312853.
54. Tung JJ, Jackson PK. Emi1 class of proteins regulate entry into meiosis and the meiosis I to meiosis II transition in Xenopus oocytes. Cell Cycle. 2005;4(3):478-82. Epub 2005/02/11. doi: 10.4161/cc.4.3.1532. PubMed PMID: 15701974.
55. Masui Y, Markert CL. Cytoplasmic control of nuclear behavior during meiotic maturation of frog oocytes. J Exp Zool. 1971;177(2):129-45. Epub 1971/06/01. doi: 10.1002/jez.1401770202. PubMed PMID: 5106340.
56. Tung JJ, Hansen DV, Ban KH, Loktev AV, Summers MK, Adler JR, 3rd, Jackson PK. A role for the anaphase-promoting complex inhibitor Emi2/XErp1, a homolog of early mitotic inhibitor 1, in cytostatic factor arrest of Xenopus eggs. Proc Natl Acad Sci U S A. 2005;102(12):4318-23. Epub 2005/03/09. doi: 10.1073/pnas.0501108102. PubMed PMID: 15753281; PMCID: PMC552977.
57. Shoji S, Muto Y, Ikeda M, He F, Tsuda K, Ohsawa N, Akasaka R, Terada T, Wakiyama M, Shirouzu M, Yokoyama S. The zinc-binding region (ZBR) fragment of Emi2 can inhibit APC/C by targeting its association with the coactivator Cdc20 and UBE2C-mediated ubiquitylation. FEBS Open Bio. 2014;4:689-703. Epub 2014/08/28. doi: 10.1016/j.fob.2014.06.010. PubMed PMID: 25161877; PMCID: PMC4141206.
58. Roehm PC, Berg JM. Sequential metal binding by the RING finger domain of BRCA1. Biochemistry. 1997;36(33):10240-5. Epub 1997/08/19. doi: 10.1021/bi970863d. PubMed PMID: 9254622.
59. Freemont PS, Hanson IM, Trowsdale J. A novel cysteine-rich sequence motif. Cell. 1991;64(3):483-4. Epub 1991/02/08. doi: 10.1016/0092-8674(91)90229-r. PubMed PMID: 1991318.
60. Ohe M, Inoue D, Kanemori Y, Sagata N. Erp1/Emi2 is essential for the meiosis I to meiosis II transition in Xenopus oocytes. Dev Biol. 2007;303(1):157-64. Epub 2006/12/05. doi: 10.1016/j.ydbio.2006.10.044. PubMed PMID: 17141208.
61. Belloc E, Mendez R. A deadenylation negative feedback mechanism governs meiotic metaphase arrest. Nature. 2008;452(7190):1017-21. Epub 2008/04/04. doi: 10.1038/nature06809. PubMed PMID: 18385675.

62. Ohe M, Kawamura Y, Ueno H, Inoue D, Kanemori Y, Senoo C, Isoda M, Nakajo N, Sagata N. Emi2 inhibition of the anaphase-promoting complex/cyclosome absolutely requires Emi2 binding via the C-terminal RL tail. Mol Biol Cell. 2010;21(6):905-13. Epub 2010/01/22. doi: 10.1091/mbc.E09-11-0974. PubMed PMID: 20089832; PMCID: PMC2836971.
63. Madgwick S, Hansen DV, Levasseur M, Jackson PK, Jones KT. Mouse Emi2 is required to enter meiosis II by reestablishing cyclin B1 during interkinesis. J Cell Biol. 2006;174(6):791-801. Epub 2006/09/13. doi: 10.1083/jcb.200604140. PubMed PMID: 16966421; PMCID: PMC2064334.
64. Hormanseder E, Tischer T, Mayer TU. Modulation of cell cycle control during oocyte-to-embryo transitions. EMBO J. 2013;32(16):2191-203. Epub 2013/07/31. doi: 10.1038/emboj.2013.164. PubMed PMID: 23892458; PMCID: PMC3746200.
65. Tischer T, Hormanseder E, Mayer TU. The APC/C inhibitor XErp1/Emi2 is essential for Xenopus early embryonic divisions. Science. 2012;338(6106):520-4. Epub 2012/09/29. doi: 10.1126/science.1228394. PubMed PMID: 23019610.
66. Fontanilla RA, Nuccitelli R. Characterization of the sperm-induced calcium wave in Xenopus eggs using confocal microscopy. Biophys J. 1998;75(4):2079-87. Epub 1998/09/24. doi: 10.1016/s0006-3495(98)77650-7. PubMed PMID: 9746550; PMCID: PMC1299880.
67. Runft LL, Watras J, Jaffe LA. Calcium release at fertilization of Xenopus eggs requires type I IP(3) receptors, but not SH2 domain-mediated activation of PLCgamma or G(q)-mediated activation of PLCbeta. Dev Biol. 1999;214(2):399-411. Epub 1999/10/20. doi: 10.1006/dbio.1999.9415. PubMed PMID: 10525343.
68. Heim A, Tischer T, Mayer TU. Calcineurin promotes APC/C activation at meiotic exit by acting on both XErp1 and Cdc20. EMBO reports. 2018;19(12). Epub 2018/10/31. doi: 10.15252/embr.201846433. PubMed PMID: 30373936; PMCID: PMC6280790.
69. Sako K, Suzuki K, Isoda M, Yoshikai S, Senoo C, Nakajo N, Ohe M, Sagata N. Emi2 mediates meiotic MII arrest by competitively inhibiting the binding of Ube2S to the APC/C. Nat Commun. 2014;5:3667. Epub 2014/04/29. doi: 10.1038/ncomms4667. PubMed PMID: 24770399.
70. Gopinathan L, Szmyd R, Low D, Diril MK, Chang HY, Coppola V, Liu K, Tessarollo L, Guccione E, van Pelt AMM, Kaldis P. Emi2 Is Essential for Mouse Spermatogenesis. Cell reports. 2017;20(3):697-708. Epub 2017/07/21. doi: 10.1016/j.celrep.2017.06.033. PubMed PMID: 28723571.
71. Schmidt A, Duncan PI, Rauh NR, Sauer G, Fry AM, Nigg EA, Mayer TU. Xenopus polo-like kinase Plx1 regulates XErp1, a novel inhibitor of APC/C activity. Genes Dev. 2005;19(4):502-13. Epub 2005/02/17. doi: 10.1101/gad.320705. PubMed PMID: 15713843; PMCID: PMC548950.
72. van der Ent A, Przybyłowicz WJ, de Jonge MD, Harris HH, Ryan CG, Tylko G, Paterson DJ, Barnabas AD, Kopittke PM, Mesjasz-Przybyłowicz J. X-ray elemental mapping techniques for elucidating the ecophysiology of hyperaccumulator plants2018;218(2):432-52. doi: https://doi.org/10.1111/nph.14810.
73. Scimeca M, Bischetti S, Lamsira HK, Bonfiglio R, Bonanno E. Energy Dispersive X-ray (EDX) microanalysis: A powerful tool in biomedical research and diagnosis. Eur J Histochem. 2018;62(1):2841. Epub 2018/03/24. doi: 10.4081/ejh.2018.2841. PubMed PMID: 29569878; PMCID: PMC5907194.

74. Chen S, Deng J, Yuan Y, Flachenecker C, Mak R, Hornberger B, Jin Q, Shu D, Lai B, Maser J, Roehrig C, Paunesku T, Gleber SC, Vine DJ, Finney L, VonOsinski J, Bolbat M, Spink I, Chen Z, Steele J, Trapp D, Irwin J, Feser M, Snyder E, Brister K, Jacobsen C, Woloschak G, Vogt S. The Bionanoprobe: hard X-ray fluorescence nanoprobe with cryogenic capabilities. Journal of synchrotron radiation. 2014;21(Pt 1):66-75. Epub 2013/12/25. doi: 10.1107/s1600577513029676. PubMed PMID: 24365918; PMCID: PMC3874019.
75. Sanchez-Cano C, Romero-Canelón I, Yang Y, Hands-Portman IJ, Bohic S, Cloetens P, Sadler PJ. Synchrotron X-Ray Fluorescence Nanoprobe Reveals Target Sites for Organo-Osmium Complex in Human Ovarian Cancer Cells. Chemistry (Easton). 2017;23(11):2512-6. Epub 2016/12/25. doi: 10.1002/chem.201605911. PubMed PMID: 28012260; PMCID: PMC5412901.
76. Zaluzec NJ. Improving the sensitivity of X-ray microanalysis in the analytical electron microscope. Ultramicroscopy. 2019;203:163-9. doi: https://doi.org/10.1016/j.ultramic.2018.11.008.
77. Zaluzec NJ. Analytical Formulae for Calculation of X-Ray Detector Solid Angles in the Scanning and Scanning/Transmission Analytical Electron Microscope. Microsc Microanal. 2014;20(4):1318-26. Epub 2014/05/22. doi: 10.1017/S1431927614000956.
78. Zaluzec NJ, Seeler J, Bleher R, O'Halloran T. Challenges in Biological X-ray Microanalysis in the AEM. Microsc Microanal. 2019;25(S2):1076-7. Epub 2019/08/05. doi: 10.1017/S1431927619006111.
79. Lugg NR, Kothleitner G, Shibata N, Ikuhara Y. On the quantitativeness of EDS STEM. Ultramicroscopy. 2015;151:150-9. Epub 2014/12/24. doi: 10.1016/j.ultramic.2014.11.029. PubMed PMID: 25535061.
80. Stika KM, Bielat KL, Morrison GH. Diffusible ion localization by ion microscopy: a comparison of chemically prepared and fast-frozen, freeze-dried, unfixed liver sections. J Microsc. 1980;118(4):409-20. Epub 1980/04/01. PubMed PMID: 7392047.
81. Schrag M, Dickson A, Jiffry A, Kirsch D, Vinters HV, Kirsch W. The effect of formalin fixation on the levels of brain transition metals in archived samples. Biometals. 2010;23(6):1123-7. Epub 2010/06/29. doi: 10.1007/s10534-010-9359-4. PubMed PMID: 20582563; PMCID: PMC3129265.
82. Punshon T, Chen S, Finney L, Howard L, Jackson BP, Karagas MR, Ornvold K. High-resolution elemental mapping of human placental chorionic villi using synchrotron X-ray fluorescence spectroscopy. Anal Bioanal Chem. 2015;407(22):6839-50. Epub 2015/07/04. doi: 10.1007/s00216-015-8861-5. PubMed PMID: 26138895; PMCID: PMC4663034.
83. Fox CH, Johnson FB, Whiting J, Roller PP. Formaldehyde fixation. J Histochem Cytochem. 1985;33(8):845-53. Epub 1985/08/01. doi: 10.1177/33.8.3894502. PubMed PMID: 3894502.
84. Chung K, Wallace J, Kim SY, Kalyanasundaram S, Andalman AS, Davidson TJ, Mirzabekov JJ, Zalocusky KA, Mattis J, Denisin AK, Pak S, Bernstein H, Ramakrishnan C, Grosenick L, Gradinaru V, Deisseroth K. Structural and molecular interrogation of intact biological systems. Nature. 2013;497(7449):332-7. Epub 2013/04/12. doi: 10.1038/nature12107. PubMed PMID: 23575631; PMCID: PMC4092167.
85. Smart KE, Smith JA, Kilburn MR, Martin BG, Hawes C, Grovenor CR. High-resolution elemental localization in vacuolate plant cells by nanoscale secondary ion mass spectrometry.

Plant J. 2010;63(5):870-9. Epub 2010/06/22. doi: 10.1111/j.1365-313X.2010.04279.x. PubMed PMID: 20561256.
86. Danscher G, Stoltenberg M. Silver enhancement of quantum dots resulting from (1) metabolism of toxic metals in animals and humans, (2) in vivo, in vitro and immersion created zinc-sulphur/zinc-selenium nanocrystals, (3) metal ions liberated from metal implants and particles. Prog Histochem Cytochem. 2006;41(2):57-139. Epub 2006/09/05. doi: 10.1016/j.proghi.2006.06.001. PubMed PMID: 16949439.
87. Hare DJ, George JL, Bray L, Volitakis I, Vais A, Ryan TM, Cherny RA, Bush AI, Masters CL, Adlard PA, Doble PA, Finkelstein DI. The effect of paraformaldehyde fixation and sucrose cryoprotection on metal concentration in murine neurological tissue. Journal of Analytical Atomic Spectrometry. 2014;29(3):565-70. doi: 10.1039/C3JA50281C.
88. Timm F. Zur Histochemie der Schwermetalle Das Sulfid-Silberverfahren. Dtsch Z Gesamte Gerichtl Med. 1958;46(5):706-11. doi: 10.1007/bf00665092.
89. Timm F, Schulz G. Hoden und Schwermetalle. Histochemie. 1966;7(1):15-21. doi: 10.1007/BF00306914.
90. Danscher G, Stoltenberg M, Bruhn M, Søndergaard C, Jensen D. Immersion Autometallography: Histochemical In Situ Capturing of Zinc Ions in Catalytic Zinc-Sulfur Nanocrystals. J Histochem Cytochem. 2004;52(12):1619-25. doi: 10.1369/jhc.4A6371.2004. PubMed PMID: 15557216.
91. de Laat SW, Buwalda RJ, Habets AM. Intracellular ionic distribution, cell membrane permeability and membrane potential of the Xenopus egg during first cleavage. Exp Cell Res. 1974;89(1):1-14. Epub 1974/11/01. PubMed PMID: 4435056.
92. Snow P, Yim DL, Leibow JD, Saini S, Nuccitelli R. Fertilization stimulates an increase in inositol trisphosphate and inositol lipid levels in Xenopus eggs. Dev Biol. 1996;180(1):108-18. Epub 1996/11/25. doi: 10.1006/dbio.1996.0288. PubMed PMID: 8948578.
93. Stith BJ. Phospholipase C and D regulation of Src, calcium release and membrane fusion during Xenopus laevis development. Dev Biol. 2015;401(2):188-205. Epub 2015/03/10. doi: 10.1016/j.ydbio.2015.02.020. PubMed PMID: 25748412; PMCID: PMC4424143.
94. Lindsay LL, Hedrick JL. Proteolysis of Xenopus laevis egg envelope ZPA triggers envelope hardening. Biochem Biophys Res Commun. 2004;324(2):648-54. Epub 2004/10/12. doi: 10.1016/j.bbrc.2004.09.099. PubMed PMID: 15474476.
95. Marszalek I, Krezel A, Goch W, Zhukov I, Paczkowska I, Bal W. Revised stability constant, spectroscopic properties and binding mode of Zn(II) to FluoZin-3, the most common zinc probe in life sciences. J Inorg Biochem. 2016;161:107-14. Epub 2016/05/25. doi: 10.1016/j.jinorgbio.2016.05.009. PubMed PMID: 27216451.
96. Fahrni CJ, O'Halloran TV. Aqueous Coordination Chemistry of Quinoline-Based Fluorescence Probes for the Biological Chemistry of Zinc. J Am Chem Soc. 1999;121(49):11448-58. doi: 10.1021/ja992709f.
97. Smirnova J, Kabin E, Järving I, Bragina O, Tõugu V, Plitz T, Palumaa P. Copper(I)-binding properties of de-coppering drugs for the treatment of Wilson disease. α-Lipoic acid as a potential anti-copper agent. Sci Rep. 2018;8(1):1463. Epub 2018/01/25. doi: 10.1038/s41598-018-19873-2. PubMed PMID: 29362485; PMCID: PMC5780470.
98. Auld DS, Falchuk KH, Zhang K, Montorzi M, Vallee BL. X-ray absorption fine structure as a monitor of zinc coordination sites during oogenesis of Xenopus laevis. Proc Natl Acad Sci U

S A. 1996;93(8):3227-31. Epub 1996/04/16. doi: 10.1073/pnas.93.8.3227. PubMed PMID: 8622918; PMCID: PMC39587.
99. Gunter TE, Miller LM, Gavin CE, Eliseev R, Salter J, Buntinas L, Alexandrov A, Hammond S, Gunter KK. Determination of the oxidation states of manganese in brain, liver, and heart mitochondria. J Neurochem. 2004;88(2):266-80. Epub 2003/12/24. doi: 10.1046/j.1471-4159.2003.02122.x. PubMed PMID: 14690515.
100. Ducic T, Barski E, Salome M, Koch JC, Bahr M, Lingor P. X-ray fluorescence analysis of iron and manganese distribution in primary dopaminergic neurons. J Neurochem. 2013;124(2):250-61. Epub 2012/10/31. doi: 10.1111/jnc.12073. PubMed PMID: 23106162; PMCID: PMC3563009.
101. Tsednee M, Castruita M, Salome PA, Sharma A, Lewis BE, Schmollinger SR, Strenkert D, Holbrook K, Otegui MS, Khatua K, Das S, Datta A, Chen S, Ramon C, Ralle M, Weber PK, Stemmler TL, Pett-Ridge J, Hoffman BM, Merchant SS. Manganese co-localizes with calcium and phosphorus in Chlamydomonas acidocalcisomes and is mobilized in manganese-deficient conditions. J Biol Chem. 2019;294(46):17626-41. Epub 2019/09/19. doi: 10.1074/jbc.RA119.009130. PubMed PMID: 31527081; PMCID: PMC6873200.
102. McNaughton RL, Reddi AR, Clement MH, Sharma A, Barnese K, Rosenfeld L, Gralla EB, Valentine JS, Culotta VC, Hoffman BM. Probing in vivo Mn2+ speciation and oxidative stress resistance in yeast cells with electron-nuclear double resonance spectroscopy. Proc Natl Acad Sci U S A. 2010;107(35):15335-9. Epub 2010/08/13. doi: 10.1073/pnas.1009648107. PubMed PMID: 20702768; PMCID: PMC2932569.
103. Sharma A, Gaidamakova EK, Matrosova VY, Bennett B, Daly MJ, Hoffman BM. Responses of Mn2+ speciation in Deinococcus radiodurans and Escherichia coli to gamma-radiation by advanced paramagnetic resonance methods. Proc Natl Acad Sci U S A. 2013;110(15):5945-50. Epub 2013/03/29. doi: 10.1073/pnas.1303376110. PubMed PMID: 23536297; PMCID: PMC3625348.
104. Sharma A, Gaidamakova EK, Grichenko O, Matrosova VY, Hoeke V, Klimenkova P, Conze IH, Volpe RP, Tkavc R, Gostincar C, Gunde-Cimerman N, DiRuggiero J, Shuryak I, Ozarowski A, Hoffman BM, Daly MJ. Across the tree of life, radiation resistance is governed by antioxidant Mn(2+), gauged by paramagnetic resonance. Proc Natl Acad Sci U S A. 2017;114(44):E9253-e60. Epub 2017/10/19. doi: 10.1073/pnas.1713608114. PubMed PMID: 29042516; PMCID: PMC5676931.
105. Horning KJ, Caito SW, Tipps KG, Bowman AB, Aschner M. Manganese Is Essential for Neuronal Health. Annu Rev Nutr. 2015;35:71-108. Epub 2015/05/15. doi: 10.1146/annurev-nutr-071714-034419. PubMed PMID: 25974698; PMCID: PMC6525788.
106. Tan X, Bernardo M, Thomann H, Scholes CP. Pulsed and continuous wave electron nuclear double resonance patterns of aquo protons coordinated in frozen solution to high spin MN2+. The Journal of Chemical Physics. 1993;98(7):5147-57. doi: 10.1063/1.464917.
107. Dworkin MB, Dworkin-Rastl E. Carbon metabolism in early amphibian embryos. Trends Biochem Sci. 1991;16:229-34. doi: https://doi.org/10.1016/0968-0004(91)90091-9.
108. Chen S, Ducic T, Jin Q, Wu X, Zaluzec N, Lai B. Synchrotron-based X-ray Fluorescence Microscopy as a Complementary Tool to Light Microscopy/Electron Microscopy for Multi-scale and Multi-modality Analysis. Microsc Microanal. 2018;24(S2):86-7. Epub 2018/08/10. doi: 10.1017/S1431927618012825.

109. Grey RD, Wolf DP, Hedrick JL. Formation and structure of the fertilization envelope in Xenopus laevis. Dev Biol. 1974;36(1):44-61. Epub 1974/01/01. PubMed PMID: 4822839.
110. Imoh H. Establishment and movement of egg regions revealed by the size class of yolk platelets in Xenopus laevis. Roux Arch Dev Biol. 1995;205(3-4):128-37. Epub 1995/11/01. doi: 10.1007/bf00357759. PubMed PMID: 28306074.
111. Zaluzec NJ. Thin film characterization using analytical electron microscopy. Thin Solid Films. 1980;72(1):177-92. doi: https://doi.org/10.1016/0040-6090(80)90572-6.
112. Kotani M, Ikenishi K, Tanabe K. Cortical granules remaining after fertilization in Xenopus laevis. Dev Biol. 1973;30(1):228-32. Epub 1973/01/01. PubMed PMID: 4735367.
113. Campanella C, Andreuccetti P. Ultrastructural observations on cortical endoplasmic reticulum and on residual cortical granules in the egg of Xenopus laevis. Dev Biol. 1977;56(1):1-10. Epub 1977/03/01. PubMed PMID: 838127.
114. Werst MM, Davoust CE, Hoffman BM. Ligand spin densities in blue copper proteins by q-band proton and nitrogen-14 ENDOR spectroscopy. J Am Chem Soc. 1991;113(5):1533-8. doi: 10.1021/ja00005a011.
115. Davoust CE, Doan PE, Hoffman BM. Q-Band Pulsed Electron Spin-Echo Spectrometer and Its Application to ENDOR and ESEEM. Journal of Magnetic Resonance, Series A. 1996;119(1):38-44. doi: https://doi.org/10.1006/jmra.1996.0049.
116. Ohkura H. Meiosis: an overview of key differences from mitosis. Cold Spring Harb Perspect Biol. 2015;7(5). Epub 2015/01/22. doi: 10.1101/cshperspect.a015859. PubMed PMID: 25605710.
117. Getz EB, Xiao M, Chakrabarty T, Cooke R, Selvin PR. A comparison between the sulfhydryl reductants tris(2-carboxyethyl)phosphine and dithiothreitol for use in protein biochemistry. Anal Biochem. 1999;273(1):73-80. Epub 1999/08/24. doi: 10.1006/abio.1999.4203. PubMed PMID: 10452801.
118. Fahrni CJ, Bourassa D, Dikdan R. Probing Biological Trace Metals with Fluorescent Indicators. In: White AR, editor. Metals in the Brain: Measurement and Imaging. New York, NY: Springer New York; 2017. p. 71-107.
119. Jordan MR, Wang J, Weiss A, Skaar EP, Capdevila DA, Giedroc DP. Mechanistic Insights into the Metal-Dependent Activation of Zn(II)-Dependent Metallochaperones. Inorg Chem. 2019;58(20):13661-72. Epub 2019/06/30. doi: 10.1021/acs.inorgchem.9b01173. PubMed PMID: 31247880; PMCID: PMC7005846.
120. Sénèque O, Latour JM. Coordination properties of zinc finger peptides revisited: ligand competition studies reveal higher affinities for zinc and cobalt. J Am Chem Soc. 2010;132(50):17760-74. Epub 2010/11/26. doi: 10.1021/ja104992h. PubMed PMID: 21105707.
121. Hitomi Y, Outten CE, O'Halloran TV. Extreme zinc-binding thermodynamics of the metal sensor/regulator protein, ZntR. J Am Chem Soc. 2001;123(35):8614-5. Epub 2001/08/30. PubMed PMID: 11525677.
122. Bauer M. HERFD-XAS and valence-to-core-XES: new tools to push the limits in research with hard X-rays? Phys Chem Chem Phys. 2014;16(27):13827-37. doi: 10.1039/C4CP00904E.
123. Proux O, Lahera E, Del Net W, Kieffer I, Rovezzi M, Testemale D, Irar M, Thomas S, Aguilar-Tapia A, Bazarkina EF, Prat A, Tella M, Auffan M, Rose J, Hazemann J-L. High-Energy Resolution Fluorescence Detected X-Ray Absorption Spectroscopy: A Powerful New

Structural Tool in Environmental Biogeochemistry Sciences. J Environ Qual. 2017;46(6):1146-57. doi: 10.2134/jeq2017.01.0023. PubMed PMID: 29293835.
124. Thomas SA, Mishra B, Myneni SCB. High Energy Resolution-X-ray Absorption Near Edge Structure Spectroscopy Reveals Zn Ligation in Whole Cell Bacteria. The Journal of Physical Chemistry Letters. 2019;10(10):2585-92. doi: 10.1021/acs.jpclett.9b01186.
125. Lai Z, Freedman DA, Levine AJ, McLendon GL. Metal and RNA binding properties of the hdm2 RING finger domain. Biochemistry. 1998;37(48):7005-15. Epub 1998/12/04. doi: 10.1021/bi980596r. PubMed PMID: 9836595.
126. Hennig J, Ottosson L, Andrésen C, Horvath L, Kuchroo VK, Broo K, Wahren-Herlenius M, Sunnerhagen M. Structural organization and Zn2+-dependent subdomain interactions involving autoantigenic epitopes in the Ring-B-box-coiled-coil (RBCC) region of Ro52. J Biol Chem. 2005;280(39):33250-61. Epub 2005/06/21. doi: 10.1074/jbc.M503066200. PubMed PMID: 15964842.
127. Reddi AR, Guzman TR, Breece RM, Tierney DL, Gibney BR. Deducing the energetic cost of protein folding in zinc finger proteins using designed metallopeptides. J Am Chem Soc. 2007;129(42):12815-27. Epub 2007/10/02. doi: 10.1021/ja073902+. PubMed PMID: 17902663.
128. Kluska K, Adamczyk J, Krężel A. Metal binding properties, stability and reactivity of zinc fingers. Coord Chem Rev. 2018;367:18-64. doi: https://doi.org/10.1016/j.ccr.2018.04.009.
129. McAllister BB, Dyck RH. Zinc transporter 3 (ZnT3) and vesicular zinc in central nervous system function. Neurosci Biobehav Rev. 2017;80:329-50. Epub 2017/06/19. doi: 10.1016/j.neubiorev.2017.06.006. PubMed PMID: 28624432.
130. Martell AE, Motekaitis RJ. Determination and Use of Stability Constants. 2 ed: Wiley; 1992.
131. Kuzmic P. Program DYNAFIT for the analysis of enzyme kinetic data: application to HIV proteinase. Anal Biochem. 1996;237(2):260-73. Epub 1996/06/01. doi: 10.1006/abio.1996.0238. PubMed PMID: 8660575.
132. Reyes-Caballero H, Guerra AJ, Jacobsen FE, Kazmierczak KM, Cowart D, Koppolu UM, Scott RA, Winkler ME, Giedroc DP. The metalloregulatory zinc site in Streptococcus pneumoniae AdcR, a zinc-activated MarR family repressor. J Mol Biol. 2010;403(2):197-216. Epub 2010/09/02. doi: 10.1016/j.jmb.2010.08.030. PubMed PMID: 20804771; PMCID: PMC2949468.
133. Yatsunyk LA, Easton JA, Kim LR, Sugarbaker SA, Bennett B, Breece RM, Vorontsov, II, Tierney DL, Crowder MW, Rosenzweig AC. Structure and metal binding properties of ZnuA, a periplasmic zinc transporter from Escherichia coli. J Biol Inorg Chem. 2008;13(2):271-88. Epub 2007/11/21. doi: 10.1007/s00775-007-0320-0. PubMed PMID: 18027003; PMCID: PMC2630496.
134. Kuzmic P. Determination of substrate kinetic parameters from progress curve data: A DynaFit tutorial Watertown, MA2015. Available from: www.biokin.com/TN/2015/05.
135. Sokaras D, Weng TC, Nordlund D, Alonso-Mori R, Velikov P, Wenger D, Garachtchenko A, George M, Borzenets V, Johnson B, Rabedeau T, Bergmann U. A seven-crystal Johann-type hard x-ray spectrometer at the Stanford Synchrotron Radiation Lightsource. The Review of scientific instruments. 2013;84(5):053102-. doi: 10.1063/1.4803669. PubMed PMID: 23742527.
136. George GN, Pickering IJ, Pushie MJ, Nienaber K, Hackett MJ, Ascone I, Hedman B, Hodgson KO, Aitken JB, Levina A, Glover C, Lay PA. X-ray-induced photo-chemistry and X-

ray absorption spectroscopy of biological samples. Journal of synchrotron radiation. 2012;19(Pt 6):875-86. Epub 2012/10/18. doi: 10.1107/S090904951203943X. PubMed PMID: 23093745.
137. George GN. 2001. Available from: http://www-ssrl.slac.stanford.edu/exafspak.html
138. Cheng R, Zhang F, Li M, Wo X, Su YW, Wang W. Influence of Fixation and Permeabilization on the Mass Density of Single Cells: A Surface Plasmon Resonance Imaging Study. Frontiers in chemistry. 2019;7:588. Epub 2019/09/12. doi: 10.3389/fchem.2019.00588. PubMed PMID: 31508410; PMCID: PMC6716545.
139. Stoltenberg M, Sørensen MB, Danscher G, Juhl S, Andreasen A, Ernst E. Autometallographic demonstration of zinc ions in rat sperm cells. Mol Hum Reprod. 1997;3(9):763-7. Epub 1997/11/14. doi: 10.1093/molehr/3.9.763. PubMed PMID: 9358001.
140. Seeler JF, Sharma A, Zaluzec NJ, Bleher R, Lai B, Schultz EG, Hoffman BM, LaBonne C, Woodruff TK, O'Halloran TV. Metal Ion Fluxes Controlling Amphibian Fertilization. Nat Chem. In Press.
141. Griffin J, Emery BR, Huang I, Peterson CM, Carrell DT. Comparative analysis of follicle morphology and oocyte diameter in four mammalian species (mouse, hamster, pig, and human). J Exp Clin Assist Reprod. 2006;3:2. Epub 2006/03/03. doi: 10.1186/1743-1050-3-2. PubMed PMID: 16509981; PMCID: PMC1413548.
142. Hippe-Sanwald S. Impact of freeze substitution on biological electron microscopy. Microsc Res Tech. 1993;24(5):400-22. Epub 1993/04/01. doi: 10.1002/jemt.1070240506. PubMed PMID: 8318724.
143. Kashiv Y, Austin JR, 2nd, Lai B, Rose V, Vogt S, El-Muayed M. Imaging trace element distributions in single organelles and subcellular features. Sci Rep. 2016;6:21437. Epub 2016/02/26. doi: 10.1038/srep21437. PubMed PMID: 26911251; PMCID: PMC4766485.
144. Zierold K, Schafer D, Pietruschka F. The element distribution in ultrathin cryosections of cultivated fibroblast cells. Histochemistry. 1984;80(4):333-7. Epub 1984/01/01. doi: 10.1007/bf00495413. PubMed PMID: 6735746.
145. Jin Q, Paunesku T, Lai B, Gleber SC, Chen SI, Finney L, Vine D, Vogt S, Woloschak G, Jacobsen C. Preserving elemental content in adherent mammalian cells for analysis by synchrotron-based x-ray fluorescence microscopy. J Microsc. 2017;265(1):81-93. Epub 2016/09/01. doi: 10.1111/jmi.12466. PubMed PMID: 27580164; PMCID: PMC5217071.
146. Edelmann L. Freeze-substitution and the preservation of diffusible ions. J Microsc. 1991;161(Pt 2):217-28. Epub 1991/02/01. PubMed PMID: 2038031.
147. Woodland HR, Pestell RQ. Determination of the nucleoside triphosphate contents of eggs and oocytes of Xenopus laevis. Biochem J. 1972;127(3):597-605. Epub 1972/04/01. doi: 10.1042/bj1270597. PubMed PMID: 4672799; PMCID: PMC1178701.
148. Colman A, Gadian DG. 31P nuclear-magnetic-resonance studies on the developing embryos of Xenopus laevis. Eur J Biochem. 1976;61(2):387-96. Epub 1976/01/15. doi: 10.1111/j.1432-1033.1976.tb10032.x. PubMed PMID: 1248465.
149. Leist DP, Nettleton GS, Feldhoff RC. Determination of lipid loss during aqueous and phase partition fixation using formalin and glutaraldehyde. J Histochem Cytochem. 1986;34(4):437-41. Epub 1986/04/01. doi: 10.1177/34.4.3081623. PubMed PMID: 3081623.
150. Höög JL, Gluenz E, Vaughan S, Gull K. Chapter 8 - Ultrastructural Investigation Methods for Trypanosoma brucei. In: Müller-Reichert T, editor. Methods Cell Biol: Academic Press; 2010. p. 175-96.

151. Riemersma JC. Chapter II - Chemical Effects of Fixation on Biological Specimens. In: Parsons DF, editor. Some Biological Techniques in Electron Microscopy. Cambridge, Massachusetts: Academic Press; 1970. p. 69-99.
152. Nielson AJ, Griffith WP. Tissue fixation by osmium tetroxide. A possible role for proteins. J Histochem Cytochem. 1979;27(5):997-9. Epub 1979/05/01. doi: 10.1177/27.5.479559. PubMed PMID: 479559.
153. Fan X, Bialecka M, Moustakas I, Lam E, Torrens-Juaneda V, Borggreven NV, Trouw L, Louwe LA, Pilgram GSK, Mei H, van der Westerlaken L, Chuva de Sousa Lopes SM. Single-cell reconstruction of follicular remodeling in the human adult ovary. Nature Communications. 2019;10(1):3164. doi: 10.1038/s41467-019-11036-9.
154. Latendresse JR, Warbrittion AR, Jonassen H, Creasy DM. Fixation of testes and eyes using a modified Davidson's fluid: comparison with Bouin's fluid and conventional Davidson's fluid. Toxicol Pathol. 2002;30(4):524-33. Epub 2002/08/22. doi: 10.1080/01926230290105721. PubMed PMID: 12187944.
155. Rowley JE, Rubenstein GE, Manuel SL, Johnson NL, Surgnier J, Kapitsinou PP, Duncan FE, Pritchard MT. Tissue-specific Fixation Methods Are Required for Optimal In Situ Visualization of Hyaluronan in the Ovary, Kidney, and Liver. J Histochem Cytochem. 2020;68(1):75-91. Epub 2019/11/13. doi: 10.1369/0022155419884879. PubMed PMID: 31714169; PMCID: PMC6931168.
156. Wachnowsky C, Fidai I, Cowan JA. Iron-sulfur cluster biosynthesis and trafficking - impact on human disease conditions. Metallomics : integrated biometal science. 2018;10(1):9-29. Epub 2017/10/12. doi: 10.1039/c7mt00180k. PubMed PMID: 29019354; PMCID: PMC5783746.
157. Baker HM, Anderson BF, Baker EN. Dealing with iron: Common structural principles in proteins that transport iron and heme2003;100(7):3579-83. doi: 10.1073/pnas.0637295100 %J Proceedings of the National Academy of Sciences.
158. Landfried DA, Vuletich DA, Pond MP, Lecomte JT. Structural and thermodynamic consequences of b heme binding for monomeric apoglobins and other apoproteins. Gene. 2007;398(1-2):12-28. Epub 2007/06/07. doi: 10.1016/j.gene.2007.02.046. PubMed PMID: 17550789; PMCID: PMC2394511.
159. Xiao Z, Brose J, Schimo S, Ackland SM, La Fontaine S, Wedd AG. Unification of the copper(I) binding affinities of the metallo-chaperones Atx1, Atox1, and related proteins: detection probes and affinity standards. J Biol Chem. 2011;286(13):11047-55. Epub 2011/01/25. doi: 10.1074/jbc.M110.213074. PubMed PMID: 21258123; PMCID: PMC3064159.
160. Ariöz C, Wittung-Stafshede P. Folding of copper proteins: role of the metal? Q Rev Biophys. 2018;51:e4. Epub 2018/03/07. doi: 10.1017/S0033583518000021.
161. Kelly SM, Butler JP, Macklem PT. Control of cell volume in oocytes and eggs from Xenopus laevis. Comp Biochem Physiol A Physiol. 1995;111(4):681-91. Epub 1995/08/01. PubMed PMID: 7671156.
162. Webb DJ, Nuccitelli R. Fertilization potential and electrical properties of the Xenopus laevis egg. Dev Biol. 1985;107(2):395-406. Epub 1985/02/01. PubMed PMID: 3972161.
163. Gillespie JI. The distribution of small ions during the early development of Xenopus laevis and Ambystoma mexicanum embryos. J Physiol. 1983;344:359-77. Epub 1983/11/01. PubMed PMID: 6655587; PMCID: PMC1193846.

164. Slack C, Warner AE, Warren RL. The distribution of sodium and potassium in amphibian embryos during early development. J Physiol. 1973;232(2):297-312. Epub 1973/07/01. PubMed PMID: 4737869; PMCID: PMC1350456.
165. Outten CE, O'Halloran TV. Femtomolar sensitivity of metalloregulatory proteins controlling zinc homeostasis. Science. 2001;292(5526):2488-92. Epub 2001/06/09. doi: 10.1126/science.1060331. PubMed PMID: 11397910.
166. Changela A, Chen K, Xue Y, Holschen J, Outten CE, O'Halloran TV, Mondragón A. Molecular basis of metal-ion selectivity and zeptomolar sensitivity by CueR. Science. 2003;301(5638):1383-7. Epub 2003/09/06. doi: 10.1126/science.1085950. PubMed PMID: 12958362.
167. Finney LA, O'Halloran TV. Transition metal speciation in the cell: insights from the chemistry of metal ion receptors. Science. 2003;300(5621):931-6. Epub 2003/05/10. doi: 10.1126/science.1085049. PubMed PMID: 12738850.
168. Jansson B. Dietary, total body, and intracellular potassium-to-sodium ratios and their influence on cancer. Cancer Detect Prev. 1990;14(5):563-5. Epub 1990/01/01. PubMed PMID: 2224920.
169. Jornvall H, Falchuk KH, Geraci G, Vallee BL. 1,10-Phenanthroline and Xenopus laevis teratology. Biochem Biophys Res Commun. 1994;200(3):1398-406. Epub 1994/05/16. doi: 10.1006/bbrc.1994.1606. PubMed PMID: 8185592.
170. Fort DJ, Stover EL, Rogers RL, Copley HF, Morgan LA, Foster ER. Chronic boron or copper deficiency induces limb teratogenesis in Xenopus. Biol Trace Elem Res. 2000;77(2):173-87. Epub 2000/12/02. doi: 10.1385/bter:77:2:173. PubMed PMID: 11101049.
171. Bonta M, Török S, Hegedus B, Döme B, Limbeck A. A comparison of sample preparation strategies for biological tissues and subsequent trace element analysis using LA-ICP-MS. Anal Bioanal Chem. 2017;409(7):1805-14. Epub 2016/12/15. doi: 10.1007/s00216-016-0124-6. PubMed PMID: 27966170; PMCID: PMC5591616.
172. Tucker KR, Li Z, Rubakhin SS, Sweedler JV. Secondary ion mass spectrometry imaging of molecular distributions in cultured neurons and their processes: comparative analysis of sample preparation. J Am Soc Mass Spectrom. 2012;23(11):1931-8. Epub 2012/08/30. doi: 10.1007/s13361-012-0472-1. PubMed PMID: 22930440; PMCID: PMC3475608.
173. Wu K, Jia F, Zheng W, Luo Q, Zhao Y, Wang F. Visualization of metallodrugs in single cells by secondary ion mass spectrometry imaging. J Biol Inorg Chem. 2017;22(5):653-61. Epub 2017/05/17. doi: 10.1007/s00775-017-1462-3. PubMed PMID: 28508381.
174. Hausen P, Riebesell M. The Early Development of Xenopus Laevis: An Atlas of the Histology: Verlag der Zeitschrift für Naturforschung; 1991.
175. Elkan ER. The Xenopus Pregnancy Test. Br Med J. 1938;2(4067):1253-74.2. Epub 1938/12/17. doi: 10.1136/bmj.2.4067.1253. PubMed PMID: 20781969; PMCID: PMC2211252.
176. Marshall M. Timeline: The Evolution of Life. New Scientist. 2009 July 14.
177. Gray D, Plusa B, Piotrowska K, Na J, Tom B, Glover DM, Zernicka-Goetz M. First cleavage of the mouse embryo responds to change in egg shape at fertilization. Curr Biol. 2004;14(5):397-405. Epub 2004/03/19. doi: 10.1016/j.cub.2004.02.031. PubMed PMID: 15028215.
178. Balachandran RC, Mukhopadhyay S, McBride D, Veevers J, Harrison FE, Aschner M, Haynes EN, Bowman AB. Brain manganese and the balance between essential roles and

neurotoxicity. J Biol Chem. 2020;295(19):6312-29. Epub 2020/03/20. doi: 10.1074/jbc.REV119.009453. PubMed PMID: 32188696; PMCID: PMC7212623.
179. Martell A. Critical Stability Constants: Volume 2: Amines: Springer US; 1975.
180. Arslan P, Di Virgilio F, Beltrame M, Tsien RY, Pozzan T. Cytosolic Ca2+ homeostasis in Ehrlich and Yoshida carcinomas. A new, membrane-permeant chelator of heavy metals reveals that these ascites tumor cell lines have normal cytosolic free Ca2+. J Biol Chem. 1985;260(5):2719-27. Epub 1985/03/10. PubMed PMID: 3919006.
181. Krizek BA, Merkle DL, Berg JM. Ligand variation and metal ion binding specificity in zinc finger peptides. Inorg Chem. 1993;32(6):937-40. doi: 10.1021/ic00058a030.
182. Lehman NL, Tibshirani R, Hsu JY, Natkunam Y, Harris BT, West RB, Masek MA, Montgomery K, van de Rijn M, Jackson PK. Oncogenic regulators and substrates of the anaphase promoting complex/cyclosome are frequently overexpressed in malignant tumors. Am J Pathol. 2007;170(5):1793-805. Epub 2007/04/26. doi: 10.2353/ajpath.2007.060767. PubMed PMID: 17456782; PMCID: PMC1854971.
183. Min KW, Park MH, Hong SR, Lee H, Kwon SY, Hong SH, Joo HJ, Park IA, An HJ, Suh KS, Oh HK, Yoo CW, Kim MJ, Chang HK, Jun SY, Yoon HK, Chang ED, Kim DW, Kim I. Clear cell carcinomas of the ovary: a multi-institutional study of 129 cases in Korea with prognostic significance of Emi1 and Galectin-3. Int J Gynecol Pathol. 2013;32(1):3-14. Epub 2012/12/04. doi: 10.1097/PGP.0b013e31825554e9. PubMed PMID: 23202783.
184. Guan C, Zhang J, Zhang J, Shi H, Ni R. Enhanced expression of early mitotic inhibitor-1 predicts a poor prognosis in esophageal squamous cell carcinoma patients. Oncol Lett. 2016;12(1):114-20. Epub 2016/06/28. doi: 10.3892/ol.2016.4611. PubMed PMID: 27347110; PMCID: PMC4906579.
185. Lehman NL, Verschuren EW, Hsu JY, Cherry AM, Jackson PK. Overexpression of the anaphase promoting complex/cyclosome inhibitor Emi1 leads to tetraploidy and genomic instability of p53-deficient cells. Cell Cycle. 2006;5(14):1569-73. Epub 2006/07/25. doi: 10.4161/cc.5.14.2925. PubMed PMID: 16861914.
186. Yu Y, Munger K. Human papillomavirus type 16 E7 oncoprotein inhibits the anaphase promoting complex/cyclosome activity by dysregulating EMI1 expression in mitosis. Virology. 2013;446(1-2):251-9. Epub 2013/10/01. doi: 10.1016/j.virol.2013.08.013. PubMed PMID: 24074588; PMCID: PMC3799973.
187. Shimizu N, Nakajima NI, Tsunematsu T, Ogawa I, Kawai H, Hirayama R, Fujimori A, Yamada A, Okayasu R, Ishimaru N, Takata T, Kudo Y. Selective enhancing effect of early mitotic inhibitor 1 (Emi1) depletion on the sensitivity of doxorubicin or X-ray treatment in human cancer cells. J Biol Chem. 2013;288(24):17238-52. Epub 2013/05/07. doi: 10.1074/jbc.M112.446351. PubMed PMID: 23645673; PMCID: PMC3682528.
188. Sigma. Formaldehyde solution, for molecular biology, BioReagent, ≥36.0% in H2O specification sheet. Available from: https://www.sigmaaldrich.com/catalog/DataSheetPage.do?brandKey=SIGMA&symbol=47608.
189. Mercadante CJ, Prajapati M, Conboy HL, Dash ME, Herrera C, Pettiglio MA, Cintron-Rivera L, Salesky MA, Rao DB, Bartnikas TB. Manganese transporter Slc30a10 controls physiological manganese excretion and toxicity. J Clin Invest. 2019;129(12):5442-61. Epub 2019/09/19. doi: 10.1172/jci129710. PubMed PMID: 31527311; PMCID: PMC6877324.
190. Xenbase. slc39a8. Available from: http://www.xenbase.org/gene/showgene.do?method=displayGeneSummary&geneId=1011740.

191. Xenbase. slc30a10. Available from: http://www.xenbase.org/gene/showgene.do?method=displayGeneSummary&geneId=1003782.
192. Xenbase. slc39a14. Available from: http://www.xenbase.org/gene/showgene.do?method=displayGeneSummary&geneId=982218&.
193. Bonnell BS, Reinhart D, Chandler DE. Xenopus laevis egg jelly coats consist of small diffusible proteins bound to a complex system of structurally stable networks composed of high-molecular-weight glycoconjugates. Dev Biol. 1996;174(1):32-42. Epub 1996/02/25. doi: 10.1006/dbio.1996.0049. PubMed PMID: 8626019.
194. Gerwien F, Skrahina V, Kasper L, Hube B, Brunke S. Metals in fungal virulence. FEMS Microbiol Rev. 2018;42(1). Epub 2017/10/27. doi: 10.1093/femsre/fux050. PubMed PMID: 29069482; PMCID: PMC5812535.
195. Waugh DS. Making the most of affinity tags. Trends Biotechnol. 2005;23(6):316-20. doi: https://doi.org/10.1016/j.tibtech.2005.03.012.
196. Purbey PK, Jayakumar PC, Deepalakshmi PD, Patole MS, Galande S. GST fusion vector with caspase-6 cleavage site for removal of fusion tag during column purification. Biotechniques. 2005;38(3):360, 2, 4 passim. Epub 2005/03/25. doi: 10.2144/05383bm03. PubMed PMID: 15786802.
197. Eschenfeldt WH, Lucy S, Millard CS, Joachimiak A, Mark ID. A family of LIC vectors for high-throughput cloning and purification of proteins. Methods Mol Biol. 2009;498:105-15. Epub 2008/11/07. doi: 10.1007/978-1-59745-196-3_7. PubMed PMID: 18988021; PMCID: PMC2771622.
198. Schneider CA, Rasband WS, Eliceiri KW. NIH Image to ImageJ: 25 years of image analysis. Nature methods. 2012;9(7):671-5. Epub 2012/08/30. doi: 10.1038/nmeth.2089. PubMed PMID: 22930834; PMCID: PMC5554542.
199. Martell AE, Smith RM. Critical Stability Constants: First Supplement: Springer US; 1982.
200. Schweiger AJ, Gunnar. Principles of Pulse Electron Paramagnetic Resonance. Oxford: Oxford University Press; 2001.
201. Salikhov KM. Schweiger, A., Jeschke, G.:Principles of pulse electron paramagnetic resonance. Applied Magnetic Resonance. 2002;22(2):319. doi: 10.1007/bf03166113.
202. Vogt S. MAPS : A set of software tools for analysis and visualization of 3D X-ray fluorescence data sets. J Phys IV France. 2003;104:635-8.
203. Thevenaz P, Unser M. User-friendly semiautomated assembly of accurate image mosaics in microscopy. Microsc Res Tech. 2007;70(2):135-46. Epub 2006/11/30. doi: 10.1002/jemt.20393. PubMed PMID: 17133410.

APPENDIX A: SUPPLEMENTARY METHODS, CALCULATIONS, FIGURES, TABLES, AND VIDEO CAPTIONS FOR METAL ION FLUXES CONTROLLING AMPHIBIAN FERTILIZATION

Materials and Methods:

Confocal Imaging Parameters: All confocal imaging was done on a Leica SP5 laser scanning confocal using the Leica Application Suite AF software in the Biological Imaging Facility at Northwestern University (RRID: SCR_017767). Images were taken with a 2.5x0.07 NA objective with an open pinhole (600 μm = 7.91 airy units). The excitation laser used was an argon laser (488 nm) coupled with a DD 488/561 beamsplitter. A Leica Hybrid (HyD) detector was set to collect emission wavelengths of 505-575 nm, using gain of 100%. Transmitted light images were taken with a transmitted light PMT using the 488 nm laser as an illumination source. For the fertilization timeseries, images were taken every 2.573 seconds for a total time of 19 minutes. Using FIJI, brightness/contrast were adjusted to 12/72. For the ionomycin timeseries, images were taken every 1.29 seconds for a total time of 9.5 minutes. Using FIJI, brightness/contrast were adjusted to 35/131. For clarity, brightness and contrast were adjusted to 19/46 in Figure 2.2A.

Determination of the Rate of the Zinc Spark: The stack of confocal images of the zinc spark was analyzed using ImageJ. (198) The egg was modeled as a sphere. Using a custom macro, 18 areas (circles with radii of 50 μM) were placed around the periphery of the egg. The circles were placed 20º apart, with 0º at the approximate beginning of the zinc release (Figure 2.2A). The software measured the average white value (i.e. fluorescence) of each circle in every frame. The data were then graphed (Figure 2.2B and 2.2C). The zinc spark travels approximately linearly in time around most of the circumference of the egg, the linear portions were analyzed.

The circumference of the egg was calculated from its diameter and every degree on the circle could therefore be given a distance. The time at which each circle reached half-maximal fluorescence was determined. To determine the rate of zinc release, the distance of each circle

along the circumference from the origin was plotted against the time at which it reached half-maximal fluorescence. A linear fit was then taken and the calculated velocities from the zinc release traveling clockwise and counterclockwise from the origin were averaged for a final value.

Evaluating the Ability of Intracellular Chelators to Induce Parthenogenetic Activation of *Xenopus* Eggs: *Xenopus* eggs were obtained via established methods. The jelly coat of the eggs was removed through soaking in a 3% w/v solution of cysteine-HCl, pH 8 for 10 minutes. ~20-30 dejellied eggs were put into a well of a 12-well dish. A 20-minute video was taken with an Olympus SZX12 microscope using a Q-Color 3 Camera. To quantify the data, each individual egg was followed over the course of the video and assigned one of three conditions: activated, not activated, or dead. None of the following treatment conditions showed signs of toxicity. Activated eggs were those which showed shrinkage/darkening of the pigment in their animal pole and shrinkage of the white activation spot. The ratio of activated eggs to activated + not activated was then calculated. Eggs tested in all four conditions came from the same frog. For replication, eggs from 3 frogs were tested. The ratios from the 3 frogs were averaged and plotted with standard deviations.

Four milliliters of standard media for *Xenopus* eggs (0.1X Marc's Modified Ringer's [MMR] buffer, – 10 mM NaCl, 200 μM KCl, 100 μM $MgSO_4$, 200 μM $CaCl_2$, 500 μM HEPES, 10 μM EDTA, pH 7.4) were placed in the wells of a 12-well dish along with the following:

1. 1% DMSO (control)
2. 10 mM 1,10-phenanthroline monohydrate (Sigma) in 1% DMSO
3. 20 μM ionomycin calcium salt (Sigma) dissolved in 1% DMSO
4. 10 mM ammonium tetrathiomolybdate (Sigma) in 1% DMSO

Egg activation was scored for the untreated group (buffer alone) as a negative control and eggs treated with 20 μM ionomycin as a positive control (Figure 2.3, Videos A.3-6). Ionomycin led to complete activation. Treatment with 10 mM 1,10-phenanthroline (OP - K_D Mn [II] = 5 x 10^{-11} M, K_D Fe [II] = 10^{-21} M, K_D Cu [II] = 1.0 x 10^{-21} M, K_D Zn [II] = 8 x 10^{-18} M) (179, 199) activates the same percentage of eggs as ionomycin (within a standard deviation). To test whether OP causes activation through copper chelation, we treated the eggs with 10 mM ammonium tetrathiomolybdate (TTM), which has a high selectivity and specificity for copper (K_D Cu [I] = 2.32×10^{-20} M). (97) TTM did not activate the eggs, suggesting that fertilization is linked to zinc depletion.

Treatment of eggs with 3 mM of N,N,N',N'-tetrakis-(2-pyridylmethyl)-ethylenediamine (TPEN), a heavy metal chelator (K_D Cu [II] = 10^{-20}, K_D Zn [II] = 10^{-16}) (180), did not lead to activation. Due to its low aqueous solubility and modest DMSO solubility (25 mM) we were not able to test significantly higher concentrations of TPEN. EtOH at a concentration as low as 2% can parthenogenically activate eggs, so it could not be used as a solvent.

Inductively Coupled Plasma Mass Spectrometry (ICP-MS): Dejellied *Xenopus* eggs were prepared as described above. The eggs were then rinsed in 0.1X MMR. To prepare samples for ICP-MS, 20 eggs were placed in a metal-free conical tube (#89049-170, VWR, Radnor, PA) with a transfer pipet and rinsed 3X with 15 ml MilliQ H_2O. 20 eggs per tube were analyzed in order to be within the standard curve and improve the signal-to-noise for copper and manganese, which are the elements with the lowest measured concentrations.

Embryos were obtained through mincing ¼ testis in a small amount of 0.1X MMR. The solution was mixed with eggs in a Petri dish and allowed to sit for 10 minutes. The dish was then

flooded with 0.1X MMR. After 30 minutes, the jelly was removed from the embryos and samples were prepared as above.

Following sample collection, the eggs/embryos were dried in a heat block at 70 C for at least 5 hours. They were then dissolved in 450 µl 67-70% trace-metal free nitric acid (#NX0407, Supelco, Burlington, MA) overnight at 70 C. The solution was then diluted to 15 ml using MilliQ H_2O. ICP elemental standards were obtained from Inorganic Ventures (Christiansburg, Virginia). The elemental concentrations were measured using a Thermo iCAP Q ICP-MS and a Thermo iCAP 7600 ICP-OES with Qtegra software (Quantitative Bio-element Imaging Center, Northwestern University). Eggs and embryos from 4 frogs were analyzed, and for each frog 3-5 tubes of eggs/embryos were measured. In order to calculate the molarity of the eggs/embryos, their average volume was assumed to be 1 µl. (174) Two-tailed, heteroscedastic T-tests were run between eggs and embryos in order to determine if there was a significant difference in metal content. No adjustments were made for multiple comparisons.

In order to determine the metal content of the frog tank water, HNO_3 was added to the water in metal-free tubes to obtain a final concentration of 2%. In order to determine the concentrations of highly concentrated elements, dilutions of the samples were made with MilliQ H_2O/HNO_3. Elemental concentrations were measured using a Thermo iCAP Q ICP-MS and a Thermo Element2 High Resolution Magnetic Sector Field ICP-MS (Quantitative Bio-element Imaging Center, Northwestern University).

EPR/ENDOR/ESEEM Spectroscopy: Frog eggs and embryos were loaded into a quartz EPR sample tube, flash-frozen in liquid nitrogen, and stored at 77 K until analysis.

EPR Spectroscopy: 35 GHz continuous-wave (CW) EPR spectra were recorded using a lab-built 35 GHz EPR spectrometer with LabVIEW 2016. (114) Absorption-display EPR spectra were collected from eggs/embryos and Mn-metabolites by using CW "rapid passage" methods at 34.9 GHz and 2 K as previously described. (101, 104) The spectra of Mn^{2+} are characteristic of an S = 5/2 ion with small zero-field splitting (ZFS), with the principal ZFS parameter, D, much less than the microwave quantum (hν). Such spectra show a central ^{55}Mn (I = 5/2) sextet arising from hyperfine interactions, A ~ 90 G, that is associated with transitions between the m_s = +1/2 and −1/2 electron-spin substrates. These features "ride on" and are flanked by significantly broader signals from the four "satellite" transitions involving the other electron-spin substates (m_s ±5/2 ⇔ ±3/2; ±3/2 ⇔ ±1/2). The net absorption spectrum is the sum of the five envelopes of these five transitions among substrates.

The Mn^{2+} EPR spectra of both frozen eggs and embryos show a resolved six-line ^{55}Mn hyperfine pattern centered at g-2 (~12 kG) riding on "wings" extending to both high and low magnetic field with a total field span of 4 kG, features which are suppressed in the derivative-mode CW EPR spectra. The wings are relatively narrow in the high-symmetry Mn complexes discussed here (Figure 2.5); broad wings are seen in low-symmetry complexes with chelating ligands and proteins. The sextet is accentuated in the derivative spectra similar to those in the commonly used "derivative-mode" EPR spectra (Figure 2.5A inset); however, the full absorption-display spectra show this central feature.

EPR experiments were performed on three batches of egg and embryo samples. The shapes of the EPR spectra of eggs and embryos are the same (Figure 2.6) so the amplitude of their EPR spectra is an appropriate indicator of total Mn^{2+}. The embryos contain on average about one-third the amount of Mn^{2+} of the eggs (~30 ± 10% remaining) across the three batches of samples. As

noted in the main text, the decrease in the Mn^{2+} EPR amplitude upon fertilization agrees with the loss of Mn^{2+} measured by ICP-MS (Figure 2.4) within the mutual uncertainties of the two measurements.

ENDOR/ESEEM Spectroscopies: Pulsed ENDOR/ESEEM spectra were recorded using a lab-built 35 GHz pulsed EPR spectrometer with Femi Instruments SpecMan4EPR. (115) All spectra were recorded at 2 K using an immersion helium cryostat. ^{31}P, ^{1}H Davies ENDOR spectra were recorded using the pulse sequence $\pi - T - \pi/2 - \tau - \pi - \tau -$ echo, where T is the time interval for the radio-frequency (RF) pulse, which is randomly hopped. (200)

The frozen-solution spectrum of an I =1⁄2 nucleus, such as ^{31}P and ^{1}H, coupled to Mn^{2+} comprises a set of doublet features centered at the nuclear larmor frequency and split by multiples of the electron-nuclear hyperfine coupling (A). The primary doublet is associated with the $m_s = \pm 1/2$ electron spin sublevels of Mn^{2+} and is split by A; weaker satellite doublets associated with the $m_s = \pm 3/2$ and $\pm 5/2$ sublevels are split by 3A and 5A. All spectra in this study display ^{1}H signals that can be assigned to the protons of bound water. In addition, all the spectra, except for the aqueous solution, show a sharp $m_s = \pm 1/2$ ^{31}P doublet from a phosphate moiety bound to Mn^{2+} center. The intensities of ^{31}P and ^{1}H signals differ significantly among the spectra, and analysis of these intensities provide a means of assessing cellular Mn^{2+} speciation. (102) ENDOR experiments were performed using the following conditions: MW frequency 34.8 GHz, temperature 2K, magnetic field ~ 12.5 kG, $t_{\pi/2}$ = 60 ns, τ = 400 ns, T_{rf} = 160 μs, repetition time 10 ms.

3-Pulse ESEEM spectra were recorded using the pulse sequence, $\pi/2 - \tau - \pi/2 - T - \pi/2 - \tau$ – echo where T is the time varied between second and third microwave pulses, with four-step phase cycling to suppress unwanted Hahn and refocused echoes. (201) A ^{14}N nucleus (I = 1)

directly coordinated with Mn^{2+} creates modulation in the electron spin echo decay, which is dominated by ^{14}N hyperfine interaction. To quantitate ^{14}N ESEEM responses from cellular Mn^{2+}, we chose as a standard the ^{14}N response from the Mn-imidazole complex, which binds one imidazole and (presumably) five waters. ESEEM experiments were performed using the following conditions: MW frequency 34.9 GHz, temperature 2K, magnetic field ~ 12.5 kG, $t_{\pi/2}$ = 50 ns, τ = 400 ns, repetition time 10 ms.

Speciation Calculations: Experiments were performed on three sets of samples and the average ^{31}P%, ^{1}H% were used to calculate the fractional Mn^{2+} speciation. The ^{31}P%, ^{1}H% ENDOR values vary somewhat among the triplicate samples and to make sure that this variation is not attributed to spectrometric variability, ENDOR spectra of Mn-Pi were recorded along with frog eggs/embryos in every case (Figure 2.5B) in every sample measurement, confirming that small yet significant variation in ^{31}P%, ^{1}H% ENDOR response for frog eggs/embryos across the triplicate experiments is independent of the experimental conditions and purely a physiological issue. The fractional populations of Mn-L, L = H_2O, Pi, polyP, and ENDOR-silent complexes reported as percentages were obtained using a heuristic binding model as described. (102)

Frozen Eggs/Lysate Controls to Test for Possible Freeze-Lysis Artifacts: By conducting EPR/ENDOR studies on frozen intact eggs, we are able to circumvent a hurdle in understanding Mn^{2+} speciation inside cells. When cells are lysed, any substitutionally-labile Mn^{2+} complexes are at risk of undergoing rapid ligand exchange reactions. In such cases the spectra of Mn^{2+} species in the lysate may not reflect the chemical state of the manganese complexes present in intracellular compartments. The same problem can arise upon rapid freezing of large cells such as frog eggs: ice crystal formation can inadvertently rupture and mix the contents of the intracellular compartments. We have directly examined this premise by “scrambling” the eggs,

gently rupturing them by ~30 seconds agitation with a Vortex™ mixer, which disrupted egg membranes and created a liquid suspension. It was anticipated that even such a mild treatment would expose Mn^{2+} sequestered in the vicinity of the plasma membrane to millimolar concentrations of small molecule ligands in the cytosol such as cysteine, histidine, NADP, NTPs, etc. As shown in Figure 2.6, this expectation is realized. In comparison to intact eggs, ENDOR spectra of crushed eggs show three-time higher ^{31}P% and two-time higher ^{1}H% response. This corresponds to an increase of the Mn-P population to ~20% and reduction of the ENDOR-silent population to ~70%, with the remainder present as aquo-Mn^{2+}. To test whether these Mn-P species arise from complex ion formation with buffer constituents, ^{31}P% ENDOR spectra were acquired on a frozen solution of 0.1X MMR spiked with 200 μM $MnSO_4 \cdot H_2O$. No Mn-P species were observed, leading us to conclude that the lysis-induced emergence of a significant population of Mn-P complexes likely arise from components of the egg cytoplasm, organelles etc. These controls suggest that freezing the eggs did not disturb the vesicular compartmentalization of Mn^{2+} and provide support the conclusion that the most abundant manganese species in the cortical granules are Mn^{2+}-carboxylate complexes.

Sulfide Fixation of Eggs and Embryos: To chemically fix the eggs/embryos, the supernatant was removed from a tube containing jelly-stripped eggs/embryos and 10 ml of fixation solution (2.5% glutaraldehyde, 2% paraformaldehyde, 20 mM NaSH, in 0.1 M PIPES buffer, pH 7.4) were added. Eggs/embryos were fixed for 2 hours at RT. We used 16% paraformaldehyde (#15710), 25% glutaraldehyde (#16220) and 0.3 M PIPES stock solutions (#11610) from EMS, Hatfield, PA. NaSH (#161527-5G, Sigma-Aldrich, St. Louis, MO) from a 1 M stock solution was added before the pH was adjusted. After fixation, the eggs were rinsed 10 minutes in 0.1 M PIPES and 3 x 5

minutes in ddH_2O, followed by dehydration in 30%, 50%, 70%, and 90% ethanol for 15 minutes each, and finally in pure ethanol for 2 x 10 minutes.

After dehydration, eggs were infiltrated with a Durcupan resin: ethanol dilution of 1:1 overnight and in pure resin for 4 hours before transfer into fresh resin in silicon molds, and polymerization at 65° C for 24 hours. Sections of 400 and 2 μm thickness were obtained with a Ultracut-S ultramicrotome (Leica, Buffalo Grove, IL) using a diamond knife (Diatome/EMS Hatfield, PA).

X-ray Fluorescence Microscopy: Egg and embryo sections were mounted on 200 nm-thick silicon nitride windows (#NX5150D, Norcada, Edmonton, AB, Canada) and were glued to aluminum sample holders using clear nail polish. The sections were analyzed using scanning X-ray fluorescence microcopy at Beamline 2-ID-D at the Advanced Photon Source at Argonne National Laboratory. The source was a 3.3-cm-period undulator, and X-rays were monochromatized by a double multilayers monochromator to provide 20-25 times higher intensity than conventional crystal monochromators. An X-ray energy of 10.3 keV was selected to excite the Kα emission lines of elements from Si to Zn. A Fresnel zone plate focused the X-ray beam onto the sample with a spot size of ~ 0.3 μm. The specimen was placed in a helium environment and mounted on an X-Y translation stage at 75º to the incident beam. An energy-dispersive silicon drift detector (Vortex-EM, Hitachi High-Technologies Science America, Northridge, CA) was used to collect X-ray fluorescence spectra while the sample was being scanned across the focus spot. Because of their large diameters, a fly scan of each egg/embryo was first taken with a 20 μm step size and a 40 ms/pixel dwell time. An area near the cortex would be selected, and then a moderate-resolution scan with a 2 μm step size and a 40 ms/pixel dwell time would be taken. The

sample would be checked for damage and then a final, high resolution scan of the cortex would be imaged with a 300 nm step size and a 500 ms/pixel dwell time. Using the program MAPS written in IDL, XRF spectrum at each pixel were individually fitted to remove background and overlaps between adjacent emission lines. Conversion of fluorescence intensities to areal densities in $\mu g/cm^2$ was performed by comparing X-ray fluorescence intensities with those from thin film standards NBS-1832 and NBS-1833 (NIST, Gaithersburg, MD).

Metal Compartment Concentrations: 400 nm-thick slices from 3 frogs were used to determine the approximate metal concentrations of the small metal-dense compartments in the egg animal pole. 8-bit grayscale images of each element were taken from the program MAPS and analyzed with ImageJ. (202) A grayscale value of 55/255 was determined to best capture the distribution of zinc-containing compartments and was then used for all the other elements in order to maintain consistency. The images were thresholded and ROIs of at least 2 pixels in size (300 x 600 nm) were selected. The grayscale values of each ROI were converted back into $\mu g/cm^2$ as well as mM by extrapolating for the volume of each voxel (300 x 300 x 400 nm). The same procedure was used to determine the metal concentrations of the compartments in the embryo animal pole. The voxel molar concentrations should be considered to be minimal values for two reasons. First, because XRF analyzes slices of *Xenopus* eggs, it is possible that a slice contains part of a compartment and part of the cytoplasm. Second, the smaller class of compartment was only several pixels in area, meaning that the compartment areas selected may contain some of the cytoplasm near their circumferences.

In order to determine the elemental content of yolk platelets, 400 nm-thick slices from 3 frogs were used for the egg animal pole. The cluster analysis function of MAPS was used to select for areas of high phosphorous. ROIs were then drawn for each platelet – however the

corresponding area of the grayscale image was checked for each to make sure that it was not an agglomeration of multiple vesicles. Clusters of four or more pixels (≥ 0.36 μm^2) were selected. Elemental concentrations were then acquired for each ROI and then averaged for each frog.

Pearson Coefficients: Grayscale images of each element were taken from MAPS. To avoid bias, coefficients were determined for the entire scanned slice areas, rather than focusing on areas rich in metal-containing clusters. Using ImageJ, a mask of the egg/embryo area was drawn for each element using the sulfur image as a base. This allowed analysis of only the egg/embryo area and not the blank space outside the plasma membrane, as well as excluding any microscopic holes in the slice. The white value at each X/Y coordinate was then saved. For each pair of elements, linear regressions were run in order to obtain Pearson coefficients. Means and standard deviations were calculated from the Pearson coefficients averaged for slices from 3-4 frogs.

Cortical Electron-Dense Vesicle Distribution: TEM images of the entire cortex of ~150 nm-thick slices of *Xenopus* eggs and embryos were obtained using ThermoFisher Talos F20 and the prototype ANL PicoProbe Analytical Electron Microscopes. In order to determine the distribution of small electron-rich vesicles, four images at a time were stitched together using the MosaicJ plugin for ImageJ. (203) Brightness and contrast were adjusted, and the images were then imported into Adobe Illustrator. The plasma membrane was approximately traced, and boxes were drawn with marks at 2, 5, and 10 μm from the membrane (Figure 2.16B). The number of small electron-rich vesicles was counted in each box. It should be noted that these are probably under-estimations, as some vesicles fall out of the fixed slice during sectioning. In order to determine the vesicle density per 100 μm^2, the number of vesicles was divided by the cortical area analyzed.

***Xenopus* Fertilization Experiments:** Approximately 50-100 *Xenopus* eggs were placed in small Petri dishes. The control dish was filled with 0.1X Marc's Modified Ringers without EDTA (MMR: 10 mM NaCl, 200 μM KCl, 100 μM $MgSO_4$, 200 μM $CaCl_2$, 500 μM HEPES, pH 7.4) while experimental dishes were filled with 0.1X MMR containing the following metal concentrations: 50 μM $ZnSO_4$, 100 μM $ZnSO_4$, 250 μM $ZnSO_4$, or 500 μM $ZnSO_4$; 0.5 mM $MnCl_2$, 1 mM $MnCl_2$, 3 mM $MnCl_2$, or 5 mM $MnCl_2$. The eggs were soaked in the solutions for 15 minutes. The solutions were removed, and the eggs were fertilized using a sperm solution created by grinding a portion of a testis in 0.1X MMR. The sperm solutions for the metal-containing dishes were spiked with metal at their corresponding concentrations. 15 minutes after fertilization, the dishes were flooded with their corresponding buffers. After cleavage became apparent (90-120 minutes), the contents of the dishes were scored according to three categories: unfertilized, properly cleaved, and failed cleavage. There were no signs of toxicity to the eggs. Because egg quality can vary, the percent proper cleavage in each experimental dish was normalized to that of its corresponding control dish. The metal content of the buffer in the control dishes was measured via ICP-MS. IC_{50} values were calculated using Graphpad.

Calculations:

Estimated Manganese Release Concentration: Via ICP-MS, *Xenopus* eggs contain on average 8.8 x 10^{13} atoms of Mn while embryos contain 4.1 x 10^{13} atoms. The amount of Mn released following fertilization is:

$$\frac{(8.8\ x\ 10^{13}\ atoms - 4.1\ x\ 10^{13}\ atoms)}{6.022\ x\ 10^{23}\ \frac{atoms}{mol}} = 7.8\ x\ 10^{-11}\ mol$$

The average radius of a *Xenopus* egg is 625 µm. If we model Mn release into a 50 µm "shell" around the embryo following fertilization, the volume of the "shell" is:

$$\frac{4\pi}{3} x\ ((6.75\ x\ 10^{-4}\ m)^3 - \ (6.25\ x\ 10^{-4}\ m)^3) = 2.7\ x\ 10^{-10}\ m^3 = 2.7\ x\ 10^{-7}\ L$$

The concentration of Mn released into the 50 µm "shell" would therefore be:

$$\frac{7.8\ x\ 10^{-11}\ mol}{2.7\ x\ 10^{-7}\ L} = 290\ \mu M$$

Supplemental Figures:

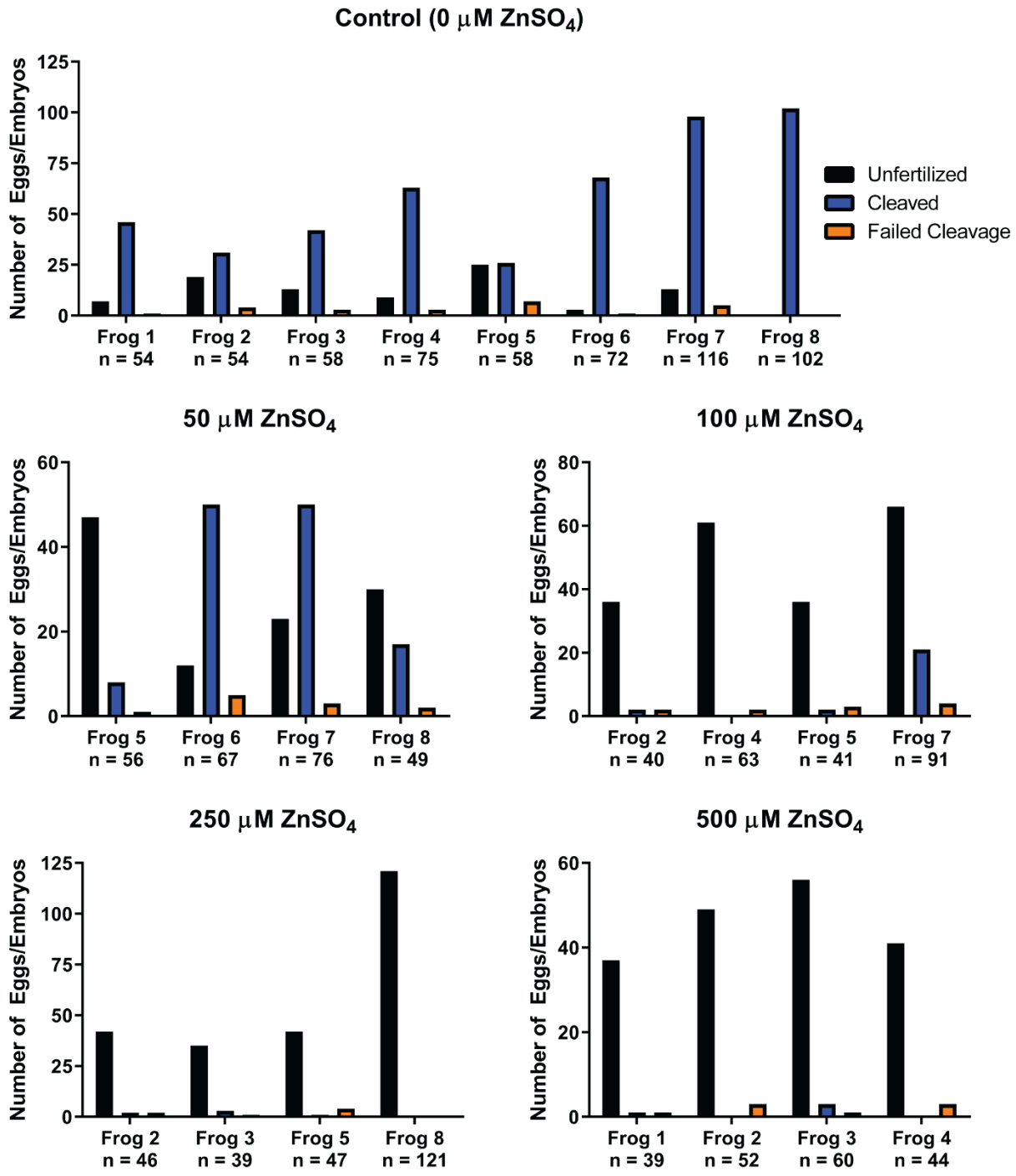

Figure A.1: Raw counts of the number of unfertilized eggs, properly dividing embryos, and failed cleavage for eggs fertilized in the presence of extracellular $ZnSO_4$. n = number of eggs used per frog for each data point.

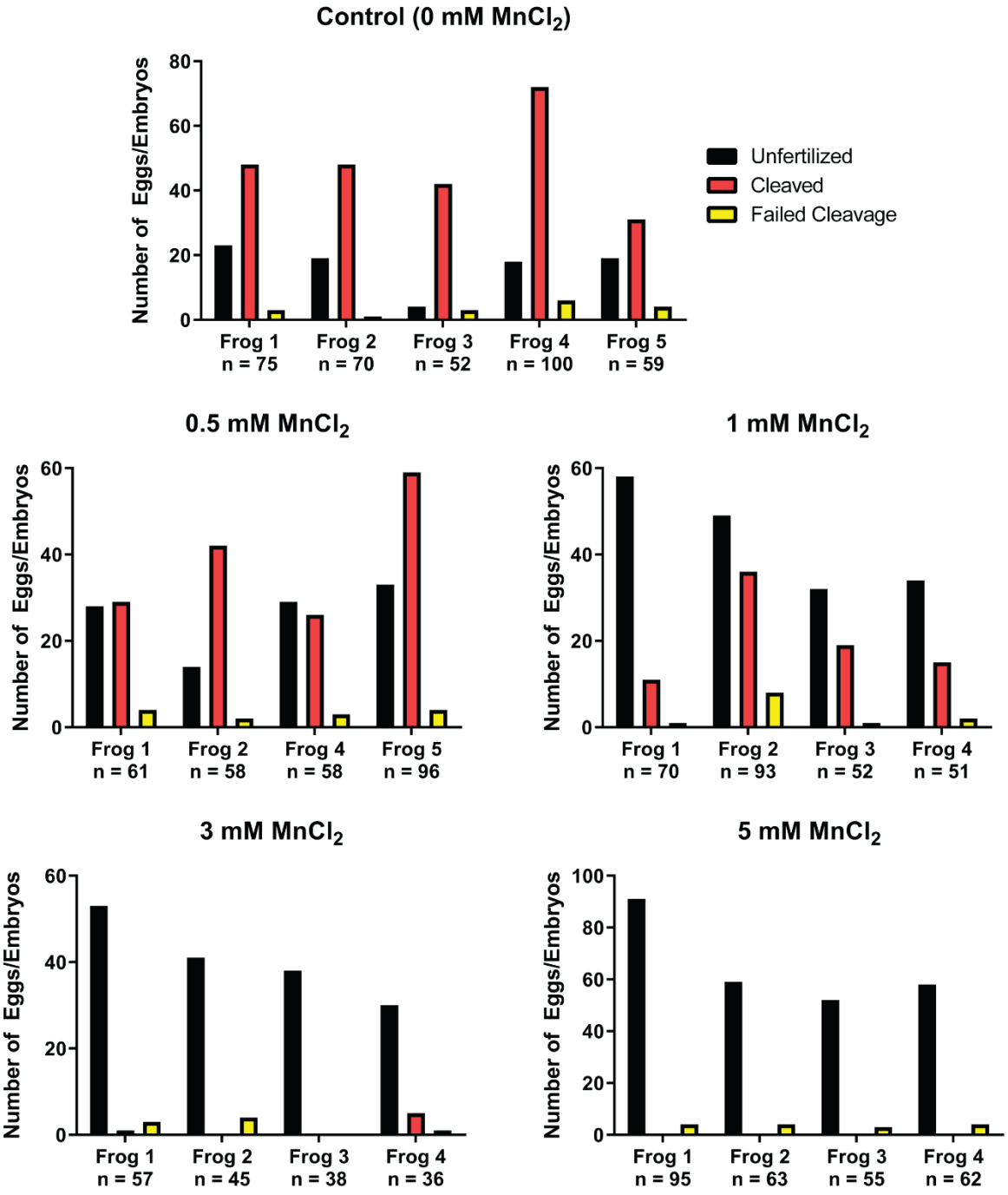

Figure A.2: Raw counts of the number of unfertilized eggs, properly dividing embryos, and failed cleavage for eggs fertilized in the presence of extracellular $MnCl_2$. n = number of eggs used per frog for each data point.

Supplemental Video Captions:

Video A.1: Zinc spark following fertilization of a *Xenopus* egg (time as mm:ss). Brightness and contrast were adjusted.

Video A.2: Zinc spark following parthenogenic activation of a *Xenopus* egg by ionomycin (time as mm:ss). Brightness and contrast were adjusted.

Video A.3: Control eggs in 0.1X MMR buffer with 1% DMSO (time as mm:ss).

Video A.4: Eggs treated with 20 μM ionomycin (time as mm:ss).

Video A.5: Eggs treated with 10 mM 1,10-phenanthroline (time as mm:ss).

Video A.6: Eggs treated with 10 mM ammonium tetrathiomolybdate (time as mm:ss).

APPENDIX B: SUPPLEMENTARY FIGURES AND TABLES FOR THE EFFECTS OF CHEMICAL FIXATION ON THE METAL CONTENT OF EGGS AND TISSUE

Supplemental Calculations:

Eggs were in 0.1X Marc's Modified Ringers Buffer (10 mM NaCl, 100 μM $MgSO_4$, 200 μM KCl, 200 μM $CaCl_2$, 10 μM EDTA, 500 μM HEPES, pH 7.4) before washes. The buffer was aspirated using a metal-free pipette tip so that ~0.5 – 1 ml remained in the tube. The eggs were washed 3X in MilliQ H_2O. The tube was filled to 15 ml with MilliQ H_2O and then the water was aspirated as described above. The following calculations estimate the amount of salt remaining from the buffer following the three washes:

Sodium:

- If there was 0.5 ml liquid remaining in the tube between steps:
  0.01 M Na x $(5 \times 10^{-4}$ L$) = 5 \times 10^{-6}$ mol Na originially in buffer
- Rinsed 3X with 15 ml ddH_2O: $\frac{5 \times 10^{-6} \text{ mol}}{30^3} =$
  1.9×10^{-10} mol Na remaining after washing
- If there was 1 ml liquid remaining in the tube between steps:
  0.01 M Na x $(1 \times 10^{-3}$ L$) = 10^{-5}$ mol Na originially in buffer
- Rinsed 3X with 15 ml ddH_2O: $\frac{10^{-5} \text{ mol}}{15^3} = 3.0 \times 10^{-9}$ mol Na remaining after washing
- Each egg is ~1 μl in volume
- 10 eggs in each tube
- By ICP, 52 mM Na in the eggs
- 10 eggs x $\frac{10^{-6} \text{ L}}{\text{egg}}$ x $\frac{0.052 \text{ mol Na}}{\text{L}} = 5.2 \times 10^{-7}$ mol Na in the eggs in the tube
- Therefore, Na remaining from the buffer should account for approximately $\frac{1.9 \times 10^{-10} \text{ mol}}{5.2 \times 10^{-7} \text{ mol}} \times 100\% = 0.037\%$ and $\frac{3.0 \times 10^{-9} \text{ mol}}{5.2 \times 10^{-7} \text{ mol}} \times 100\% = 0.58\%$ of the Na measured by ICP

Magnesium:

- If there was 0.5 ml liquid remaining in the tube between steps:
  10^{-4} M Mg x $(5 \times 10^{-4}$ L$) = 5 \times 10^{-8}$ mol Mg originially in buffer
- Rinsed 3X with 15 ml ddH_2O: $\frac{5 \times 10^{-8} \text{ mol}}{30^3} =$
  1.9×10^{-12} mol Mg remaining after washing

- If there was 1 ml liquid remaining in the tube between steps:
  10^{-4} M Mg x (1×10^{-3} L) = 10^{-7} mol Mg originially in buffer
- Rinsed 3X with 15 ml ddH_2O: $\frac{10^{-7}\ \text{mol}}{15^3} = 3.0 \times 10^{-11}$ mol Mg remaining after washing
- Each egg is ~1 µl in volume
- 10 eggs in each tube
- By ICP, 21 mM Mg in the eggs
- 10 eggs x $\frac{10^{-6}\ \text{L}}{\text{egg}}$ x $\frac{0.021\ \text{mol Mg}}{\text{L}} = 2.1 \times 10^{-7}$ mol Mg in the eggs in the tube
- Therefore, Mg remaining from the buffer should account for approximately $\frac{1.9 \times 10^{-12}\ \text{mol}}{2.1 \times 10^{-7}\ \text{mol}} \times 100\% = 0.00090\%$ and $\frac{3.0 \times 10^{-11}\ \text{mol}}{2.1 \times 10^{-7}\ \text{mol}} \times 100\% = 0.014\%$ of the Mg measured by ICP

Potassium:

- If there was 0.5 ml liquid remaining in the tube between steps:
  2×10^{-4} M K x (5×10^{-4} L) = 1×10^{-7} mol K originially in buffer
- Rinsed 3X with 15 ml ddH_2O: $\frac{1 \times 10^{-7}\ \text{mol}}{30^3} =$
  3.7×10^{-12} mol K remaining after washing
- If there was 1 ml liquid remaining in the tube between steps:
  2×10^{-4} M K x (1×10^{-3} L) = 2×10^{-7} mol K originially in buffer
- Rinsed 3X with 15 ml ddH_2O: $\frac{2 \times 10^{-7}\ \text{mol}}{15^3} =$
  5.9×10^{-11} mol K remaining after washing
- Each egg is ~1 µl in volume
- 10 eggs in each tube
- By ICP, 81 mM K in the eggs
- 10 eggs x $\frac{10^{-6}\ \text{L}}{\text{egg}}$ x $\frac{0.081\ \text{mol Mg}}{\text{L}} = 8.1 \times 10^{-7}$ mol K in the eggs in the tube
- Therefore, K remaining from the buffer should account for approximately $\frac{3.7 \times 10^{-12}\ \text{mol}}{8.1 \times 10^{-7}\ \text{mol}} \times 100\% = 0.00046\%$ and $\frac{5.9 \times 10^{-11}\ \text{mol}}{8.1 \times 10^{-7}\ \text{mol}} \times 100\% = 0.0073\%$ of the K measured by ICP

Calcium:

- If there was 0.5 ml liquid remaining in the tube between steps:
  $2 \text{ x } 10^{-4}$ M Ca x $(5 \text{ x } 10^{-4} \text{ L}) = 1 \text{ x } 10^{-7}$ mol Ca originially in buffer
- Rinsed 3X with 15 ml ddH_2O: $\frac{1 \text{ x } 10^{-7} \text{ mol}}{30^3} =$
  $3.7 \text{ x } 10^{-12}$ mol Ca remaining after washing
- If there was 1 ml liquid remaining in the tube between steps:
  $2 \text{ x } 10^{-4}$ M Ca x $(1 \text{ x } 10^{-3} \text{ L}) = 2 \text{ x } 10^{-7}$ mol Ca originially in buffer
- Rinsed 3X with 15 ml ddH_2O: $\frac{2 \text{ x } 10^{-7} \text{ mol}}{15^3} =$
  $5.9 \text{ x } 10^{-11}$ mol Ca remaining after washing
- Each egg is ~1 µl in volume
- 10 eggs in each tube
- By ICP, 1.1 mM Ca in the eggs
- 10 eggs x $\frac{10^{-6} \text{ L}}{\text{egg}}$ x $\frac{0.0011 \text{ mol Ca}}{\text{L}} = 1.1 \text{ x } 10^{-8}$ mol Ca in the eggs in the tube
- Therefore, Ca remaining from the buffer should account for approximately $\frac{3.7 \text{ x } 10^{-12} \text{ mol}}{1.1 \text{ x } 10^{-8} \text{ mol}}$ x $100\% = 0.034\%$ and $\frac{5.9 \text{ x } 10^{-11} \text{ mol}}{1.1 \text{ x } 10^{-8} \text{ mol}}$ x $100\% = 0.54\%$ of the Ca measured by ICP

In sum, assuming that the tube contents were mixed with each wash, at most ~0.6% of the measured elemental content could be attributed to salts remaining from the buffer.

Supplemental Tables:

Copper Contamination from DI Water

Element	Eggs	Fixed	Dehydrated	Resin-Infused	p Eggs → FND	p Fixed → Dehyd	p Dehyd → Resin	p Eggs → Resin
Cu	50 ± 1.4	74 ± 1.2	55 ± 6.6	46 ± 0.89	1.8×10^{-5}	0.065	0.27	0.054
Cu (fixed with NaSH)	50 ± 1.4	75 ± 5.3	49 ± 2.4	48 ± 0.70	0.015	9.3×10^{-3}	0.83	0.23

Table B.1: Copper content of unfixed eggs washed with MilliQ H_2O and fixed eggs washed with diH_2O. Values in μM. Values as mean ± SEM, N = 4 frogs. p values compare the change in elemental content between the different stages of the sample preparation process.

Xenopus Eggs Fixed Without NaSH

Element	Eggs	Fixed	Dehydrated	Resin-Infused	p Eggs → Fixed	p Fixed → Dehyd.	p Dehyd. → Resin	p Eggs → Resin
Na	52 ± 3.1	59 ± 3.3	48 ± 3.6	34 ± 3.4	0.16	0.067	0.028	8.2×10^{-3}
Mg	21 ± 1.1	19 ± 1.2	19 ± 0.97	17 ± 1.3	0.39	0.78	0.33	0.075
P	290 ± 12	270 ± 13	230 ± 13	200 ± 13	0.31	0.069	0.15	2.2×10^{-3}
S	130 ± 5.0	130 ± 5.8	124 ± 5.4	120 ± 7.7	0.90	0.80	0.58	0.39
K	81 ± 2.9	4.1 ± 0.54	6.5 ± 1.1	6.8 ± 1.2	7.9×10^{-5}	0.11	0.86	1.8×10^{-5}
Ca	1.1 ± 0.10	1.1 ± 0.12	1.1 ± 0.12	1.3 ± 0.16	0.77	0.87	0.39	0.22
Mn	0.12 ± 0.015	0.10 ± 0.013	0.10 ± 0.010	0.12 ± 0.019	0.51	0.91	0.36	0.82
Fe	0.89 ± 0.19	1.4 ± 0.12	1.4 ± 0.13	1.6 ± 0.16	0.072	0.94	0.24	0.022
Cu	0.058 ± 0.0058	0.062 ± 0.0060	0.063 ± 0.0049	0.070 ± 0.0066	0.61	0.94	0.43	0.22
Zn	1.9 ± 0.16	2.0 ± 0.13	1.9 ± 0.10	2.2 ± 0.17	0.95	0.83	0.18	0.27

Table B.2: ICP values of the elemental content of eggs fixed without NaSH. Values in mM. Values as mean ± SEM, N = 4 frogs. p values compare the change in elemental content between the different stages of the sample preparation process.

Xenopus Eggs Fixed with NaSH

Element	Eggs	Fixed	Dehydrated	Resin-Infused	p Eggs → Fixed	p Fixed → Dehyd.	p Dehyd. → Resin	p Eggs → Resin
Na	52 ± 3.1	64 ± 2.2	52 ± 2.3	38 ± 2.5	0.020	0.011	4.6×10^{-3}	0.012
Mg	21 ± 1.1	19 ± 0.94	18 ± 0.66	17 ± 0.62	0.33	0.50	0.14	0.031
P	290 ± 12	270 ± 8.1	230 ± 8.6	200 ± 4.5	0.29	9.1×10^{-3}	0.036	2.1×10^{-3}
S	130 ± 5.0	200 ± 7.1	190 ± 6.0	190 ± 5.9	3.1×10^{-4}	0.32	0.80	3.4×10^{-4}
K	81 ± 2.9	4.1 ± 0.50	5.5 ± 0.90	5.9 ± 1.4	8.4×10^{-5}	0.23	0.82	1.1×10^{-5}
Ca	1.1 ± 0.10	1.0 ± 0.15	1.1 ± 0.078	1.4 ± 0.28	0.85	0.80	0.32	0.32
Mn	0.12 ± 0.015	0.093 ± 0.014	0.095 ± 0.16	0.12 ± 0.014	0.27	0.94	0.30	0.96
Fe	0.89 ± 0.19	1.3 ± 0.15	1.3 ± 0.16	1.7 ± 0.17	0.19	0.85	0.13	0.018
Cu	0.058 ± 0.0058	0.56 ± 0.0057	0.056 ± 0.0073	0.070 ± 0.0073	0.78	0.94	0.23	0.25
Zn	1.9 ± 0.16	1.8 ± 0.13	1.8 ± 0.18	2.3 ± 0.20	0.40	0.90	0.11	0.22

Table B.3: ICP values of the elemental content of eggs fixed with NaSH. Values in mM. Values as mean ± SEM, N = 4 frogs. p values compare the change in elemental content between the different stages of the sample preparation process.

Mouse Ovary Fixation

Element	Unfixed	MD	FA	GA/FA/NaSH	GA/FA	p Unfixed → MD	p Unfixed → FA	p Unfixed → GA/FA/NaSH	p Unfixed → GA/FA
Na	1200 ± 28	5.6 ± 1.3	1900 ± 68	2000 ± 51	1800 ± 24	7.3×10^{-9}	1.1×10^{-5}	1.4×10^{-8}	2.0×10^{-8}
Mg	220 ± 6.8	9.9 ± 1.9	40 ± 2.2	74 ± 3.2	75 ± 1.2	1.4×10^{-9}	2.7×10^{-9}	2.6×10^{-9}	6.2×10^{-8}
P	3500 ± 110	2400 ± 120	2300 ± 92	2000 ± 51	2100 ± 76	1.5×10^{-5}	9.8×10^{-7}	3.0×10^{-7}	1.6×10^{-7}
S	2200 ± 67	1500 ± 79	1200 ± 16	3000 ± 77	1600 ± 35	8.0×10^{-6}	9.6×10^{-7}	1.0×10^{-6}	1.2×10^{-5}
K	3900 ± 120	4.3 ± 1.1	120 ± 5.2	26 ± 2.7	22 ± 1.5	8.3×10^{-9}	9.7×10^{-9}	8.5×10^{-9}	8.5×10^{-9}
Ca	52 ± 2.2	4.6 ± 1.2	16 ± 0.59	14 ± 0.64	15 ± 0.62	2.0×10^{-9}	3.2×10^{-7}	1.6×10^{-7}	2.2×10^{-7}
Mn	0.41 ± 0.018	0.15 ± 0.017	0.29 ± 0.0080	0.28 ± 0.015	0.29 ± 0.011	5.8×10^{-8}	1.4×10^{-4}	6.8×10^{-5}	1.1×10^{-4}
Fe	97 ± 2.9	92 ± 6.4	99 ± 4.6	88 ± 3.5	86 ± 2.7	0.50	0.76	0.064	0.016
Cu	1.2 ± 0.059	1.1 ± 0.060	1.0 ± 0.054	1.0 ± 0.034	0.95 ± 0.035	0.26	0.057	0.016	3.6×10^{-3}
Zn	20 ± 0.70	5.4 ± 0.67	25 ± 1.5	16 ± 0.36	17 ± 0.41	6.3×10^{-10}	8.1×10^{-3}	7.3×10^{-4}	0.011

Table B.4: ICP values of the elemental content of ovaries fixed with the following: MD: Modified Davidson's Fixative (14% denatured ethanol, 37.5% formalin, 6.25% glacial acetic acid in dH_2O), FA: 4% formaldehyde, GA/FA/NaSH: 2.5% glutaraldehyde, 2% formaldehyde in 0.1 M PIPES buffer with 20 mM NaSH, GA/FA: 2.5% glutaraldehyde, 2% formaldehyde in 0.1 M PIPES buffer. Values in μg/g tissue (wet weight). Values as mean ± SEM, N = 7-8 ovaries per condition. p values compare the change in elemental content between unfixed ovaries and the different fixation conditions.

VITA

John F. Seeler

781-697-0862 - johnseeler2015@u.northwestern.edu

EDUCATION

Northwestern University, Evanston IL Expected June 2021
Ph.D. Candidate
- Interdisciplinary Biological Sciences Graduate Program

Wheaton College, Wheaton IL 2013
B.S. Biochemistry and B.A. German, summa cum laude
- Received the American Institute of Chemists Foundation Award
- Studied for one semester at the Ludwig-Maximilians-Universität, Munich, Germany

RESEARCH EXPERIENCE

Northwestern University 2015-Present
Graduate research assistant in Dr. Thomas V. O'Halloran's laboratory
- Discovered that a zinc efflux following fertilization, as well as a novel manganese release, occurs the frog *Xenopus laevis*
- Utilized confocal microscopy, inductively coupled plasma mass spectrometry, and *in vitro* techniques to characterize metal release and its effects
- Collaborated with scientists at Argonne National Laboratory to image and characterize a system of metal storage vesicles in frog eggs

Boston Children's Hospital 2013-2015
Research assistant
- Supported research in signal transduction in cancers

Wheaton College 2012-2013
Student researcher
- Synthesized frameworks for chromium light-harvesting complexes

UMass Memorial Medical Center, Worcester MA 2011
Summer research assistant
- Ran PCRs to determine murine genotypes for antibody class switching research

TEACHING EXPERIENCE

Northwestern University 2017-Present
- Supervise undergraduate biology and chemistry students working on the purification and characterization of a meiotic protein
- Led two laboratory sections of 20 students each as a teaching assistant for Biological Sciences – Investigative Laboratory, focusing on molecular biology techniques
- Assisted students in their studies and managed test taking for Fundamentals of Biochemistry lecture

GRANTS

Cellular and Molecular Basis of Disease NIH T32 Training Grant 2017-2019

CONFERENCE PRESENTATIONS

John F. Seeler, Reiner Bleher, Nestor Zaluzec, Ajay Sharma, Barry Lai, Olga Antipova, Brian M. Hoffman, Teresa K. Woodruff, Carole LaBonne, Thomas V. O'Halloran. Metal Release from *Xenopus laevis* Zygotes Following Fertilization. International Conference on Biological Inorganic Chemistry, August 2019. Poster Presentation.

John F. Seeler, Stephen Allen, Teresa K. Woodruff, & Thomas V. O'Halloran. The Function of the Meiotic Protein EMI2. EMBO Meiosis Conference, August 2017. Poster Presentation.

PUBLICATIONS

John F. Seeler, Ajay Sharma, Nestor J. Zaluzec, Reiner Bleher, Barry Lai, Emma G. Schultz, Brian M. Hoffman, Carole LaBonne, Teresa K. Woodruff, Thomas V. O'Halloran. Metal Ion Fluxes Controlling Amphibian Fertilization. *Nature Chemistry*. In Press. 2021.

John F. Seeler, Yu-Ying Chen, Carole LaBonne, Teresa K. Woodruff, Reiner Bleher, Thomas V. O'Halloran. The Elemental Effects of Sulfide Fixation. In preparation.

Nestor J. Zaluzec, **John Seeler**, Reiner Bleher, Thomas O'Halloran. Challenges in Biological X-ray Microanalysis in the AEM. *Microscopy and Microanalysis*. 2019;25(S2):1076-7.

SKILLS AND TECHNIQUES

Laboratory
Inductively coupled plasma mass spectrometry, confocal microscopy, X-ray fluorescence microscopy, bacterial protein expression and purification, mammalian cell culture, western blotting

Computer
Microsoft Office, Graphpad, Adobe Illustrator

Languages
German (Advanced), French (Intermediate), Spanish (Beginner)